Optical modeling of thin film silicon solar cells with random and periodic light management textures

vorgelegt von
Diplom–Physiker
Daniel Lockau
aus Regensburg

Von der Fakultät IV - Elektrotechnik und Informatik
der Technischen Universität Berlin
zur Erlangung des akademischen Grades
Doktor der Naturwissenschaften
Dr. rer. nat.

genehmigte Dissertation

Promotionsausschuss:

Vorsitzende: Prof. Dr.-Ing. Sibylle Dieckerhoff
Berichter: Prof. Dr. Bernd Rech
Berichter: Prof. Dr.-Ing. Rolf Schuhmann
Berichter: Prof. Dr. Frank Schmidt
Berichter: Prof. Dr. Marko Topič

Tag der wissenschaftlichen Aussprache: 19.10.2012

Berlin 2013

D 83

Abstract

Better light trapping concepts are a prerequisite for the success of thin film silicon photovoltaics. This thesis presents optical simulations on statistical and periodic absorption enhancing textures for thin film silicon solar cells.

For simulation of statistically textured solar cells a rough surface synthesization method is characterized and found applicable for synthesization of commercial FTO (fluorine doped tin oxide) surfaces. Possible model errors are induced in rigorous simulation of extended scatterers by insufficient computational domain size and the lateral boundary conditions. An analysis of these errors yields that a sampling of relatively small domain widths is sufficient for modeling extended rough surfaces in thin film silicon devices. Cell efficiencies resulting from the simulation of 2D rough surfaces and 1D cuts are compared. Finally, a commonly employed statistical ray tracing algorithm is compared to rigorous simulation for a test case.

Growth conditions need to be strongly considered for light trapping texture design of polycrystalline thin film devices. Simulations are done in close connection to the experimental development of polycrystalline thin film silicon layers on a periodic light trapping texture. A precise geometrical model is reconstructed from cross–sectional images of the experimental structure. A comparison of optical absorptance measurements with the simulated absorptance of the model yields very good quantitative agreement. In simulations, the model is further analyzed by scaling and back reflector variation. Maximum light path improvement factors are found for specific texture periods, which coincide with the findings of other groups. The results from the scaling analysis highlight the importance of achieving a few micrometers layer thickness of the deposited silicon for attaining high absorptance values. A further enhancement of absorptance is reached by employing a detached flat back reflector. The resulting simulated cells have a single–pass comparable absorptance of more than 37 μm of silicon.

Planar photonic crystal structures are a different field of research for which the periodic patterning and polycrystalline silicon growth methods, developed for solar cells, might be applicable. In a first test, the general quality of a patterned and silicon coated substrate is assessed by a comparison of specular reflectivity measurements to simulated band structures. Good agreement is found between experiment and simulation.

Acknowledgement

For the project of my thesis I was given the chance to work on the interface between the institute of silicon photovoltaics at *Helmholtz–Zentrum Berlin* (HZB) and the *Zuse–Institute Berlin* (ZIB), which is a mathematical research institute. I very much enjoyed gaining insight into both, the research field of thin film silicon photovoltaics and the numerical analysis of optical problems. This rare work environment made it possible for me to tackle a very challenging problem of current photovoltaic research.

I would like to express my deepest gratitude to my mentors at both institutes, Prof. Dr. Bernd Rech at HZB and PD Dr. Frank Schmidt at ZIB, for their continuous support and for giving me a lot freedom in the choice of my research direction.

I am very indebted to Dr. Lin Zschiedrich and Dr. Sven Burger from the computational nano–optics group at ZIB for sharing their experience in optical simulation with me and for giving important advice for the progress of my work. I am also thankful to the ZIB spin off company *JCMwave* for providing the finite element solver that was used for the simulations in this thesis.

Further, I am profoundly indebted to Dr. Christiane Becker and Dr. Tobias Sontheimer from HZB for many discussions on light trapping, for giving me insight into material growth and experimental methods as well as for providing experimental input to my simulations. I am also very thankful to Dr. Florian Ruske for discussions on multilayer optics and his opinion on material parameters.

I would like to express my sincere gratitude to Assoc. Prof. Dr. Janez Krč from University of Ljubljana for helping me understand the principles of approximate optical solvers for solar cells with rough interfaces, for providing the simulation software *SunShine* as well as for the pleasant environment he created during my stay at Ljubljana.

I am thankful to Dr. Volker Hagemann and Dr. Eveline Rudigier from *SCHOTT* for providing data on commercial tin oxide surfaces and for providing the textured solgel surfaces which

were studied in this thesis. I also thank Dr. Volker Hagemann for interesting discussions on light trapping systems.

I thank Dr. Jürgen Hüpkes from Forschungszentrum Jülich for providing data on etched zinc oxide surfaces.

I am very thankful to my colleague Martin Hammerschmidt for carefully proof reading the entire manuscript and suggesting many corrections. I also thank Christoph Schwanke, Benjamin Kettner, Dr. Christiane Becker and Dr. Jan Pomplun for their corrections on selected chapters of this thesis.

Many thanks also to Dr. Mark Blome for helpful discussions and input on *Open CASCADE* modeling, especially for making the *Netgen* surface triangulator work in the *pythonocc* interface.

I would also like to thank all group members at ZIB who have not yet been mentioned, Therese Pollok, Maria Rozova, Dr. Kiran Hiremath and Sascha Briest, for creating a very enjoyable work environment.

Last, I am very thankful to my family for their for their unreserved support during the last years.

Contents

1. Introduction

Electricity is an outstanding versatile form of useable energy with the capability of directly powering a wide range of devices. It is almost emission free in application and is therefore an important factor in the global development of health and working conditions [Hai+07; MK09; Ieab]. However, providing access to electrical energy to the world population will get increasingly difficult in future years. Additionally to the traditional use of fossil thermal energy sources, renewable energy sources will need to be employed to ensure a sustainable development of the global climate and the world energy supply [Lew07].

A technology of high prospect on the road to a clean and sustainable world energy supply is the photovoltaic energy conversion. Already today photovoltaic systems are an alternative for home electrification in rural areas of developping and emerging countries. Most of these areas are rich in renewable energy sources and emerging projects on home electrification with micro–hydropower grids and home photovoltaic systems have proven successful [MK09; Ren; LRS11]. However, due to its extreme scalability and low dependence on local conditions the success of photovoltaic technology is not limited to such small scale applications. Megawatt sized power plants can be assembled in many regions. Even Germany has an estimated roof top only photovoltaic potential of more than 160 GWp [Löd+10]. Photovoltaic technology is therefore integrated as one of the renewable energy sources in current roadmaps for a clean and sustainable world energy supply. The IEA technology roadmap [BMD11] predicts an annual market of 105 GW for photovoltaic systems in 2030 and a total installed capacity of 900 GW that contributes 5% to the total electricity generation. These production capabilities have to be built from a currently very small basis and require stable annual growth at double digit rates [Ieaa].

To maintain the current annual growth rate in photovoltaics of over 20% [Ieaa] inexpensive cell technologies with a potential for high throughput production need to be established. In view of a sustainable energy supply these technologies should also not be limited by the abundance of the required materials. Silicon thin film technology has the potential to meet all these requirements if cell efficiencies can be brought into the range of silicon wafer solar cells. The primary prerequisite for this is a comparable device absorption. This thesis presents studies

on absorption enhancement technologies for thin film silicon solar cells.

Absorption enhancement in thin film silicon solar cells

The bandgap of crystalline silicon is very well suited for photovoltaic energy conversion of the solar emission spectrum. Wavelengths in the wide spectral range from near–UV to near–IR light contribute to photocurrent generation and solar cells with efficiencies of 20%–25% have already been built from multi– or monocrystalline wafers [Gre+12]. Yet silicon is an indirect semiconductor in the wavelength range of photovoltaic application and its absorption coefficent decreases continuously and substantially towards the band edge. The large absorber thickness in wafer devices of more than one hundred micrometers cannot be reached in thin film technology due to the lower electric quality of the deposited material. A light induced degradation, known as the Staebler–Wronski effect, limits the film thickness of the highly absorptive amorphous silicon even to below a few hundred nanometers [Kol04]. This degradation can be overcome in a nanocrystalline material which includes small crystallites in the amorphous matrix. Nanocrystalline silicon can be directly grown using suitable deposition methods like LPCVD [Mei+94; Rec+03]. In a different approach amorphous silicon is crystallized to polycrystalline silicon after deposition using an annealing step [Gre+04; Son+09]. Still solar cells from nano– and polycrystalline material are limited by their material quality to a thickness of a few micrometers only. Current efficiency records of single junction thin film silicon solar cells are 10.1% for amorphous as well as nanocrystalline devices and 10.5% for polycrystalline devices [Gre+12]. For the common combination to amorphous / nanocrystalline tandem cells 12.3% cell efficiency was reported.

The large efficiency gap between thin film and wafer devices results to a high degree from insufficient absorption of incident light in thin film devices. Only a small amount of light is absorbed in a single pass through the solar cell's absorber layer in most of the wavelength range. To improve the device absorption, scattering optical elements have to be added to the planar device structure.

In today's industrial applications, absorption enhancement is reached mostly by a random texturing of the interface of the cell's deposition substrate. From geometrical considerations an absorption enhancement limit of almost 50 was predicted by Yablonovitch for a directionally completely randomized electromagnetic field with respect to a single perpendicular pass through the silicon absorber layer [Yab82]. It is unlikely that a complete randomization of the field can be reached for thin film cells and only moderate absorption enhancement has been shown experimentally [Ber+06]. A texture optimization for specific thin film structures is necessary to obtain best results. Computer simulations have already been used for that purpose for

more than a decade now. The most widespread simulation method is based on statistical ray tracing [LPS94; KST02; Krč+03; Krč+04; SPV04; Spr+05; Lan+11; Jäg+11]. In recent years rigorous optical simulation tools have also been increasinglyused for analysis and optimization of solar cell designs with random interface textures [Roc+07; Bit+08; Agr+10; Roc+10; Jan+10; Loc+11; Lac+11].

An even higher enhancement than the geometrical limit predicted by Yablonovitch was recently derived by Yu in the wave optical picture [YF11]. He computed a possible light path enhancement of almost 160 in uniform layers. Yu also demonstrated that this limit could be reached in optimized grating textures, which have already been studied by optical simulation for several years. Many design concepts with the possibility for a high absorption enhancement were proposed [Zen+08; CK+09; AP09; Wei+10; She+11b]. However, due to constraints in device production few of the designs were brought to application. Especially for polycrystalline thin film silicon solar cells it was recently demonstrated by Sontheimer that crystal growth conditions need to be strongly considered for the device texture design [Son11].

This thesis makes contributions to optical simulation of thin film silicon solar cells incorporating both random and periodic light management textures. To the field of simulation of randomly textured solar cells a model error analysis is contributed. Further the rigorous simulation is compared to an implementation of a partially coherent statistical ray tracer. To the field of periodically textured solar cells a study of a realistic device structure, suitable for implementation in polycrystalline thin film silicon solar cells, is contributed. This work was done accompanying the development of polycrystalline thin film silicon layers on periodic substrates by Sontheimer [Son11]. Best absorption enhancement was found in simulation of textures with spaced flat silver back reflectors. A different field of application for the same periodic texturing and silicon deposition methods are planar photonic crystals. In a first study the band structures obtained from simulation and from experimental measurement were compared.

Thesis outline

Chapter 2 introduces the fundamental conepts and the methods used throughout this thesis. A brief overview on silicon thin film photovoltaics is given in section 2.1. The optical and geometrical modeling techniques which were applied in the simulations are presented in the sections 2.2.1 and 2.4.2. The Monte Carlo sampling technique applied for rough surface simulation is introduced in section 2.3.

Chapter 3 contains the results of simulations on solar cells with rough interface textures. A

characterization of a rough surface synthesization method with respect to experimental surfaces is presented in section 3.2. The chapter continues with an analyzation of possible model errors in space discretized rigorous modeling of rough surfaces in 2D and 3D in the sections 3.4 and 3.5. Cell efficiencies resulting from the simulation of 1D and 2D rough surfaces are compared in section 3.5.2. Finally a commonly employed statistical ray tracing algorithm is compared to rigorous simulation for a pessimistic test case in section 3.6.

Chapter 4 contains an analysis of a realistic periodic light trapping texture. An experimental comparison is presented in section 4.2.5. Possible improvements on light trapping by texture period variation and application of different back reflector designs are presented in sections 4.2.7 and 4.2.8.

Chapter 5 contains the results from a comparison of experimentally measured and simulated band structures for a periodically patterned silicon thin film. The applied measurement method is discussed with respect to comparable simulations in section 5.2. The resulting bandstructures are discussed in section 5.3.

2. Fundamentals and methods

This chapter elaborates the fundamentals of thin film silicon solar cell optics and introduces the numerical concepts used for optical simulation. It further explains the Monte Carlo sampling and the techniques applied for geometrical modeling of the solar cell devices.

2.1. Thin film silicon solar cells

This section starts with a short review of the working principle of single–junction silicon solar cells and the spectral properties of the sun. Then it introduces the device structure of the polycrystalline thin film silicon devices fabricated at Helmholtz–Zentrum Berlin, which were in the focus of the optical modeling throughout this thesis. A suitably simplified device structure was used for the optical simulations and is depicted in Fig. 2.3.

2.1.1. Photovoltaic energy conversion

The working principle of semiconductor solar cells is very well covered by corresponding text books as “Physics of Solar Cells” by Peter Würfel [Wür05]. This section therefore only gives a brief introduction of the single–junction device principle for which optical designs were simulated.

Two conditions are required to build a working solar cell. First the field energy of the incident electromagnetic field has to be converted into electro–chemical energy. This mechanism is provided in a semiconductor by excitation of an electron from the valence band into the conduction band by absorption of a photon of sufficiently high energy, as depicted schematically in red in Fig. 2.1(a). Secondly a charge separation towards the contacts of the photovoltaic device has to be achieved to make the chemical energy useable as electrical energy. This is achieved by insertion of electron and hole filters to both sides of the solar cell’s absorber layer. An idealized depth profile of a single–junction solar cell is depicted in Fig. 2.1, (a). The introduced filter layers are n– and p–doped with respect to the absorber layer for electron and hole extraction, respectively. In the idealized layout the dopings realize a one–directional increase

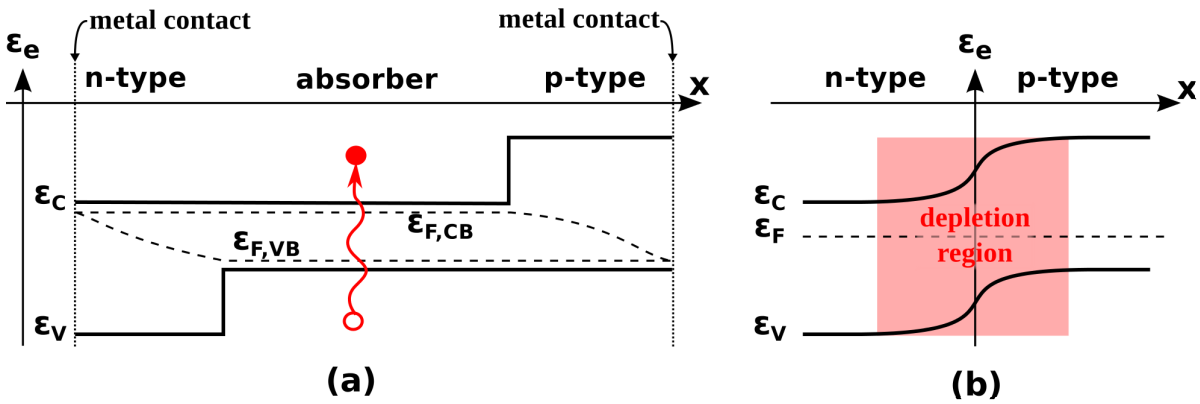

Figure 2.1.: *Depth profiles of the electrical energy. Diagrams as in [Wür05, chap. 6]. **(a)** Ideal working principle of a semiconductor solar cell. The potential structure is visualized under equilibrium conditions. Illumination leads to a splitting of the Fermi levels of conduction and valence bands. The red inset symbolizes an absorption process. **(b)** Realistic bandstructure at a pn–junction under equilibrium conditions. The red region marks the contact region in which the depletion of semiconductor majority carrier concentrations by diffusion processes leads to a band bending.*

of the band gap, thus resulting in a reduction of hole or electron density in the layers. The band shifts of valence and conduction band act like barriers for the charge carriers in the absorber layer. Under these conditions illumination leads to a Fermi level splitting, as visualized in the diagram, and to charge separation towards the contacts of the cell. An electric circuit can now be powered by the solar cell, which can yield a maximum voltage equivalent to the splitting of the Fermi levels at the contacts.

In the idealized layout the enlarged band gaps in the filter layers reduce absorption with respect to the absorber layer. This is generally not ideally realized by realistic pn–junctions between differently doped semiconductor material. A typical depth profile of the electrical energy at a pn–junction, between two differently doped semiconductors of the same kind, is shown in Fig. 2.1, (b). Charge carrier diffusion and recombination in the contact zone leads to a depletion of majority carriers in each doping region. The same process builds up an electric field, which acts opposed to the diffusion current. Under steady state conditions with a constant Fermi level, both valence and conduction bands bend accross the pn–junction. An energy barrier is realized but the band gap remains similar to the band gap of the absorber material.

2.1.2. Quantum efficiency

Linear processes dominate in optical absorption in conventional solar cells. Thermalization of excited charge carriers further happens on a shorter time scale than extraction. Therefore a maximum of one charge carrier pair can be created by absorption of a photon, independent of the photon's excess energy beyond the band gap energy difference.

The figure of merit for solar cell optimization is the external quantum efficiency, often denoted as EQE. This quantity measures the probability of a an incident photon of a certain energy to be converted into a charge carrier pair separated at the contacts. In contrast the internal quantum efficiency (IQE) measures the probability of an absorbed photon to be converted into a charge carrier pair separated at the contacts.

From optical simulation the cell absorptance can be computed. In the solar cell model described above the absorptance fraction of the absorber layer equals the EQE of a cell under the assumption of perfect carrier extraction, i.e. neglecting all electrical loss mechanisms.

2.1.3. Spectral properties of the sun

The solar spectrum above the atmosphere is to a good approximation the spectrum generated by a black body at a temperature of $T_{\text{eff, sun}} \approx 5777\text{K}$[1]. In earth's atmosphere the sunlight is subject to absorption and scattering. For the purpose of experimental comparison a standard spectrum has been defined in the norm IEC 60904-3, named "AM1.5g". This spectrum is depicted in Fig. 2.2 along with the spectrum above the atmosphere in spectral irradiance units and additionally in photon numbers. It means to represent standard conditions in mid latitudes, with an "air mass" (AM) factor of 1.5 which corresponds to a zenith incidence at 48.2°. The suffix "g", for "global", indicates that both direct as well as indirect sunlight have been taken into account. Narrow bands visible in the spectrum are due to molecular absorption. Scattering in air mostly happens on molecules and has a wavelength dependent cross section of $Q_R \propto 1/\lambda^4$ (Rayleigh scattering [Bat84]). Due to this effect, the maximum of the solar spectrum is blue shifted in regions where the diffuse part of radiation is more important than the direct part, as for example in northern Europe. The AM1.5g spectrum is mostly useful for comparison of solar systems within one technology. The amount of diffused light due to cloud coverage and the large range in local solar irradiance, see table 2.1, makes it necessary to adapt the photovoltaic technology to local conditions.

Photovoltaic energy conversion in a single absorber material is, due to the rapid thermalization of "hot" carriers to the band edge mentioned in the previous section, rather dependent on

[1] NASA sun factsheet: `http://nssdc.gsfc.nasa.gov/planetary/factsheet/sunfact.html`

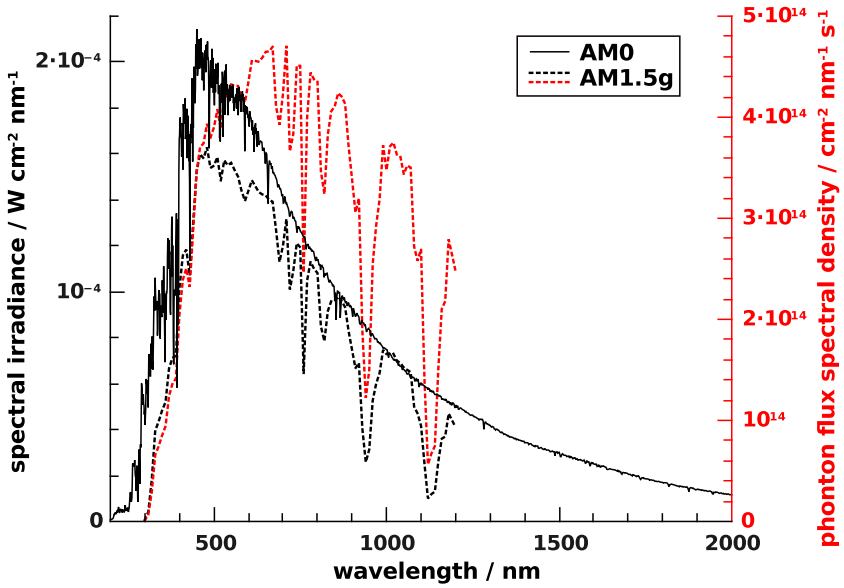

Figure 2.2.: *Spectral irradiance of the sun above the atmosphere (AM0, full black line) and at AM1.5g standard terrestrial conditions (dashed black line). The solar photon flux spectral density at AM1.5g conditions is included as a dashed red line.*

the spectral photon flux than on the energy flux. The photon flux in the spectral region relevant to silicon photovoltaics is depicted as a dotted line in Fig. 2.2. Its maximum is around 600 nm wavelength and it does not decrease as steeply as the spectral irradiance. Therefore, a high contribution to the photocurrent can come from near IR light.

2.1.4. Polycrystalline thin film silicon devices

In contrast to monocrystalline or multicrystalline wafer cells, thin film silicon devices are created by material deposition on a substrate. As a result the grown layers only feature small crystallites which can be annealed up to the micrometer or even millimeter range, depending on the crystallization method. The SPC method employed for creating the experimental reference textures in chapter 4 typically creates crystals in the micrometer range. Depending on the amorphous fraction the silicon is referred to as “amorphous silicon” (a–Si), “microcrystalline

country	annual irradiation range / kWh m^{-2} Year^{-1}
Germany	1000–1500
USA (mainland)	1350–2500
Spain	1300–2000

Table 2.1.: *Annual irradiance ranges in different regions (source: irradiance maps by the NREL GIS group, http://www.nrel.gov/gis/mapsearch.html).*

silicon" (μc–Si) or "polycrystalline silicon" (poly–Si). In polycrystalline silicon only a very low fraction of amorphous material is present.

The amorphous and crystalline phases of silicon have distinctly different optical and electrical properties. The absorption of amorphous silicon is strongly determinded by the location of its mobility edge. It absorbs better than crystalline silicon in most of the spectral region below 800 nm wavelength. For higher wavelengths amorphous silicon is almost transparent. Solar cells based on amorphous silicon material suffer from a light–induced degradation of their initial efficiency, the Staebler–Wronski effect [Kol04]. This effect is less pronounced for thin layers and limits the cell thickness of amorphous silicon solar cells to a few hundred nanometers. The Staebler–Wronski effect can also be stabilized in a mixed phase material of crystalline grains in an amorphous tissue. The so–called microcrystalline or nanocrystalline silicon has crystallite sizes in the nanometer range and can be deposited at considerably higher layer thickness than amorphous silicon [Mei+94; Rec+03]. Nanocrystalline silicon absorbs up to the band gap of crystalline silicon at 1100 nm wavelength. Due to their only partially overlapping absorption spectra, a–Si and μc–Si cells are often combined to tandem cells in a stack layout, to obtain a higher cell efficiency [SCB07].

Polycrystalline material is not yet employed much in industrial solar cell production. Its optical properties match closely with the properties of monocrystalline silicon. The band gap is about 1.12 eV which corresponds to a wavelength of light of approximately 1100 nm. Electrical properties allow deposition of several micrometers of polycrystalline material without considerable losses. However, deposition quality is highly dependent on the used deposition substrate [Son11].

Current cell efficiency records reported by Green [Gre+12] are 10.1% for a–Si, 10.1% for μc–Si, 12.3% for a–Si/μc–Si tandem and 10.5% for poly–Si cell layouts.

Device structure and optical properties of the modeled devices

The solar cell layout employed in the experimental fabrication of the polycrystalline silicon solar cells modeled in this thesis is depicted in Fig. 2.3 and further described in the references [Gal+09; Son11]. It consists of a highly doped n+ emitter layer, a weakly positively doped p− base layer and a back surface field p+ with strong positive doping. All silicon layers are deposited by electron beam evaporation and subsequently thermally annealed by SPC to obtain polycrystalline material. The fabricated cells are in the "superstrate" layout, i.e. the cells are illuminated through their deposition substrate and the back reflector is deposited as the last layer. Front contacting of the cells is made by a highly transparent conductive oxide (TCO), aluminum doped zinc oxide (ZnO:Al, AZO). The back contact is made by a very thin

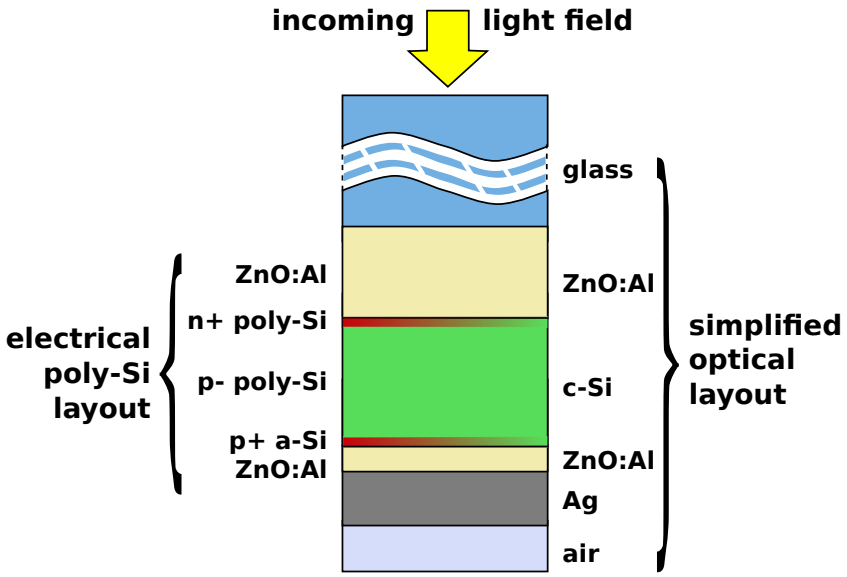

Figure 2.3.: *Vertical device structure of a polycrystalline thin film silicon solar cell in superstrate configuration.*

ZnO:Al layer and the silver reflector. The thin back TCO layer improves the reflectivity of the back reflector.

To reduce the computational effort, especially in 3D simulations, p+– and n+–doped layers are omitted in the optical layout, as depicted schematically in Fig. 2.3. Omitting the highly doped front layer might be a crude approximation for the high–frequency part of the solar spectrum in a case where an absolute estimation of cell efficiency is sought, due to parasitic absorption which does not contribute to photocurrent generation. But as the layer's material properties are very similar to the silicon absorber material they do not represent an additional optical element and can be safely omitted for characterization purposes and relative comparison of different light trapping textures.

For a brief discussion of the optical properties of the simulated devices the absorptance path length of 90% absorption is depicted in Fig. 2.4, left, and a comparison of the absorption coefficients of crystalline silicon and the ZnO:Al material data used for simulation is depicted in the same Figure, right. The requirement for a high efficiency of the solar cells is a good absorption throughout the whole wavelength range up to the indirect band gap of silicon. This is difficult to achieve in silicon as silicon is an indirect semiconductor in the operating wavelength range of the photovoltaic device. Its absorption coefficient decreases over about six decadic orders of magnitude from the direct band edge in the UV to the indirect band edge in the near infrared. The path length of 90% absorption diagram shows that for high efficiency an absorption path length of at least a few hundred micrometers has to be reached close to the

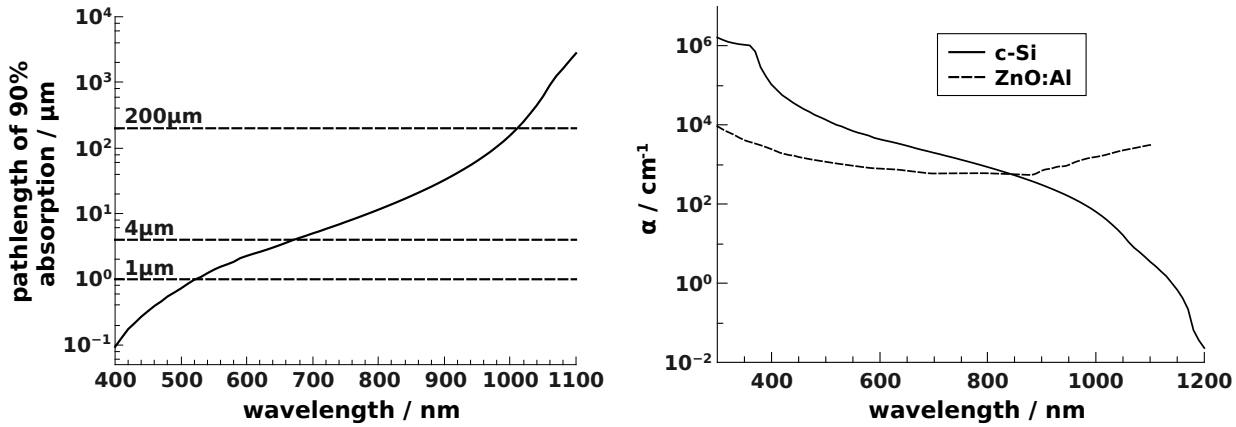

Figure 2.4.: ***Left:*** *Pathlength of 90% absorption in crystalline silicon.* ***Right:*** *Comparison of the absorption coefficients of silicon and ZnO:Al.*

band edge. This path length can be attained either by material thickness or by light trapping effects. In thin film silicon solar cell technology light trapping is of an extreme importance for device efficiency. Good light trapping schemes, as the one presented in chapter 4 of this thesis, allow to reach effective path lengths of hundreds of micrometers at an absorber layer thickness of only a few micrometer.

The AZO material employed as TCO in the simulations of this thesis has a high free carrier absorption in the near infrared. Consequently its absorption is larger in that wavelength range than for silicon. The used data set does have high absorption coefficient throughout the whole wavelength range compared to other data sets available to the author. It was not exchanged during the simulations of this thesis for reasons of consistency.

The complete set of material data used for the simulations in this thesis is included in appendix A.

2.2. Optical modeling

Thin film silicon solar cells are complex material systems with dimensions in the wavelength range of visible and near infrared light. This wavelength range is also their operating regime as an opto–electronic device. Sharp interfaces between the materials with different refractive index and periodic texturing can bring the optical response to a near resonance condition for certain wavelengths. Interference effects are also visible in the spectral response of thin film devices with statistical interface textures. Statistical ray tracing solvers need to include interference effects for a good approximation of the thin film optical systems [KST02; Spr+05]. Pure geometrical optics based ray tracing does not approximate these systems well in most of the spectral range [Sch09].

The studies presented in this thesis target a predictive ab initio modeling of the optics of PV devices. Given that the dimensions of the physical systems are on the order of the wavelength of light this objective can only be reached by rigorous simulation of Maxwell's equations. For optical modeling of 2D and 3D material distributions the author used the finite element software *JCMsuite*. The software was used with a custom Python package for 3D grid generation, described in section 2.4.2, and a Matlab based toolbox for pre– and post–processing of numerical results. A transfer matrix based algorithm implemented in Matlab was used for 1D simulations and the incoherent superstrate coupling described in section 2.2.3.

This section provides information about the finite element and transfer matrix implementations. It further discusses the sun as a light source on earth and justifies its representation by a polarized plane wave in rigorous simulation. The incoherent superstrate coupling used in the simulations within this thesis to obtain experimental comparability is discussed in section 2.2.3. Finally section 2.2.4 discusses the measurement of numerical errors in optical simulations used throughout this thesis.

2.2.1. Rigorous optical modeling

Maxwell's equations

Maxwell's equations describe the optical response of a system's interaction with a high number of photons based on linear macroscopic material laws. This is the correct model for the simulation of conventional solar cells where non–linear optical effects are negligible. All rigorous simulation methods used in this thesis are based on a solution of the time harmonic Maxwell's equations, i.e. the steady state response of the physical system at a single wavelength.

Maxwell's equations in their differential form can be written as [Jac99]

$$\nabla \cdot \mathbf{D}(\mathbf{r}, t) = \varrho(\mathbf{r}) \tag{2.1}$$
$$\nabla \times \mathbf{E}(\mathbf{r}, t) = -\partial_t \mathbf{B}(\mathbf{r}, t) \tag{2.2}$$
$$\nabla \cdot \mathbf{B}(\mathbf{r}, t) = 0 \tag{2.3}$$
$$\nabla \times \mathbf{H}(\mathbf{r}, t) = \mathbf{j}(\mathbf{r}, t) + \partial_t \mathbf{D}(\mathbf{r}, t) \tag{2.4}$$

with the constituting material laws

$$\mathbf{D}(\mathbf{r}, t) = \varepsilon(\mathbf{r})\mathbf{E}(\mathbf{r}, t) \tag{2.5}$$
$$\mathbf{B}(\mathbf{r}, t) = \mu(\mathbf{r})\mathbf{H}(\mathbf{r}, t) \tag{2.6}$$
$$\mathbf{j}(\mathbf{r}, t) = \sigma(\mathbf{r})\mathbf{E}(\mathbf{r}, t) + \mathbf{j}_{\text{impressed}}\,. \tag{2.7}$$

which describe the linear relations of the electric and magnetic field and the macroscopic material properties. Here **E** is the electric field and **D** the displacement, **H** the magnetic field and **B** the magnetic flux density. **j** labels the local electric current which is divided into a response to the local electric field dependent on the local conductivity σ and an externally impressed current $\mathbf{j}_{\text{impressed}}$. The permittivity ε and the permeability μ (with $\varepsilon, \mu \in \mathbb{R}$) describe the local electric and magnetic response on the field. ϱ is the local net density of charges.

The time harmonic Maxwell's equations are obtained from these equations by using the time harmonic ansatz

$$\begin{aligned} \mathbf{E}(\mathbf{r}, t) &= \Re\left\{\hat{\mathbf{E}}(\mathbf{r}, \omega)e^{-i\omega t}\right\} \\ \mathbf{H}(\mathbf{r}, t) &= \Re\left\{\hat{\mathbf{H}}(\mathbf{r}, \omega)e^{-i\omega t}\right\} \end{aligned} \tag{2.8}$$

which separates the spatial variation of the fields and a harmonic oscillation in time with frequency $\omega/2\pi$. A complex field representation will be used in the following. The physical solution is obtained as the real part of the introduced complex fields.

If further the complex permittivity is defined as

$$\hat{\varepsilon}(\mathbf{r}, \omega) = \varepsilon_0 \varepsilon_r(\mathbf{r}, \omega) = \varepsilon + i\frac{\sigma}{\omega} \tag{2.9}$$

and the law of conservation of charges is reformulated in terms of time harmonic quantities

$$\begin{aligned} \nabla \cdot \mathbf{j}_{\text{impressed}}(\mathbf{r}, t) + \partial_t \varrho(\mathbf{r}, t) &= 0\,, \\ \nabla \cdot \hat{\mathbf{j}}_{\text{impressed}}(\mathbf{r}, \omega) - i\omega\hat{\varrho}(\mathbf{r}, \omega) &= 0 \end{aligned} \tag{2.10}$$

Maxwell's equations can be rewritten as

$$\nabla \cdot \hat{\varepsilon}(\mathbf{r},\omega)\hat{\mathbf{E}}(\mathbf{r},\omega) = -\frac{i}{\omega}\nabla \cdot \hat{\mathbf{j}}_{\text{impressed}}(\mathbf{r},\omega) \tag{2.11}$$

$$\nabla \times \hat{\mathbf{E}}(\mathbf{r},\omega) = i\omega\hat{\mu}(\mathbf{r},\omega)\hat{\mathbf{H}}(\mathbf{r},\omega) \tag{2.12}$$

$$\nabla \cdot \hat{\mu}(\mathbf{r},\omega)\hat{\mathbf{H}}(\mathbf{r},\omega) = 0 \tag{2.13}$$

$$\nabla \times \hat{\mathbf{H}}(\mathbf{r},\omega) = -i\omega\hat{\varepsilon}(\mathbf{r},\omega)\hat{\mathbf{E}}(\mathbf{r},\omega) + \hat{\mathbf{j}}_{\text{impressed}}(\mathbf{r},\omega) \tag{2.14}$$

In this formulation the system of equations for the fields **E** and **H** can be fully decoupled and solved separately: The time harmonic Maxwell's equations for the electric field are obtained by substituting eq. 2.12 into eq. 2.14. In all following equations the hats denoting the quantities of the time harmonic formulation will be omitted. The time harmonic Maxwell's equations for the electric field are

$$\nabla \times \mu^{-1}\nabla \times \mathbf{E}(\mathbf{r}) - \omega^2\varepsilon\mathbf{E}(\mathbf{r}) = i\omega\mathbf{j}_{\text{impressed}}(\mathbf{r})\,. \tag{2.15}$$

From the solution of the electric field the magnetic field can be derived as

$$\mathbf{H}(\mathbf{r}) = \frac{1}{i\omega\mu(\mathbf{r})}\nabla \times \mathbf{E}(\mathbf{r})\,. \tag{2.16}$$

The transfer matrix method

For some simulations presented in chapters 3, 4 and 5 a transfer matrix implementation was used to obtain solutions of Maxwell's equations for the electric field in 1D material stacks. A stack of material layers with plane normals parallel to the *z*–axis is assumed in the following. As the material distribution is homogeneous in the *xy*–plane no field discontinuities are present in these directions and the electric field can be represented by its Fourier integral,

$$\mathbf{E}(\mathbf{r},\omega) = \frac{1}{(2\pi)^2}\int_{\mathbb{R}^2}\mathbf{u}(k_x,k_y)e^{i(k_x x + k_y y + k_z(k_x,k_y)z)}dk_x dk_y \tag{2.17}$$

which is an expansion into plane waves with coefficients **u**. k_z is defined by the refractive index n, the vacuum wavelength of light λ_0 and the propagation direction of the Fourier component along $\pm z$ by

$$k_z^{\pm}(k_x,k_y) = \pm\sqrt{(k_0 n)^2 - k_x^2 - k_y^2}\,, \tag{2.18}$$

where $k_0 = \frac{2\pi}{\lambda_0}$ is the absolute value of the wave vector in vacuum.

The individual Fourier components in eq. 2.17 are not coupled by the stack of material

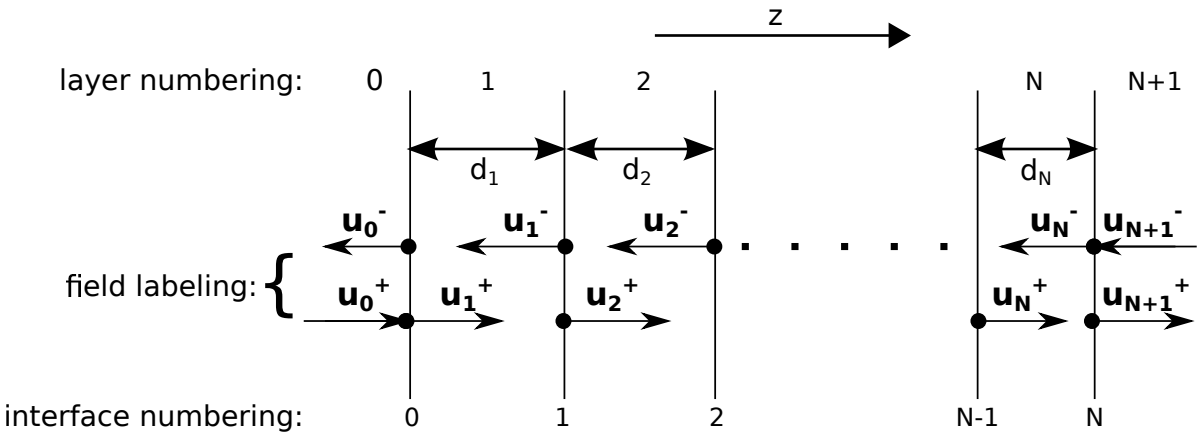

Figure 2.5.: *Field, layer and interface labeling of the transfer matrix method implementation described in the text*

layers. Therefore the solution can be obtained by solving a coupled system of boundary value problems for each Fourier component separately.

The stack numbering and field description depicted in Fig. 2.5 will be used in the following. The field inside every layer is decomposed into two counter–propagating components as

$$\begin{aligned}\mathbf{u}_m(\mathbf{r}) &= \mathbf{u}_m^+(\mathbf{r}) + \mathbf{u}_m^-(\mathbf{r}) \\ &= \tilde{\mathbf{u}}_m^+ e^{i(k_x x + k_y y + k_z^+(k_x,k_y)(z - z_{0,m}^+))} + \tilde{\mathbf{u}}_m^- e^{i(k_x x + k_y y + k_z^-(k_x,k_y)(z - z_{0,m}^-))}\,.\end{aligned} \tag{2.19}$$

The zero phase point of $\mathbf{u}_m^\pm$ in the stack normal direction is $x = 0$, $y = 0$, $z = z_{0,m}^\pm$. The positions $z_{0,m}^\pm$ are marked with dots in Fig. 2.5 and chosen such that fields are always decreasing in absorbing internal layers at propagation to the opposite layer interface. In every layer 6 degrees of freedom have to be fixed which in the numbering of Fig. 2.5 sums up to $6(N+2) = 6N+12$. From Maxwell's first equation, eq. 2.11 and the assumption of no impressed currents, we obtain the condition that inside every layer

$$\begin{aligned}\nabla \cdot \mathbf{u}_m(\mathbf{r}) &= \nabla \cdot \mathbf{u}_m^+(\mathbf{r}) + \nabla \cdot \mathbf{u}_m^-(\mathbf{r}) \\ &= \mathbf{k}^+ \cdot \mathbf{u}_m^+(\mathbf{r}) + \mathbf{k}^- \cdot \mathbf{u}_m^-(\mathbf{r}) = 0\end{aligned} \tag{2.20}$$

where $\mathbf{k}^\pm = [k_x, k_y, k_z^\pm]^T$. The condition has to hold for every position $\mathbf{r}$ and hence

$$\mathbf{k}^\pm \cdot \mathbf{u}_m^\pm(\mathbf{r}) = 0\,. \tag{2.21}$$

These conditions are applied to all fields of the finite layers and the outgoing fields in the infinite layers. The incoming fields in the infinite layers are set as incoming fields on the right

hand side.

From eq. 2.21 ($2N + 2$) conditions are set for the fields inside the layers. Including the incoming fields ($2N + 8$) conditions are set and ($4N + 4$) conditions remain open. These can be fixed by relating the fields by 4 conditions at each of the ($N + 1$) layer interfaces. The full set of boundary conditions which has to hold at the plane interface between the two adjacent layers m, $m + 1$ is [Jac99]

$$(\varepsilon_m \mathbf{u}_m - \varepsilon_{m+1}\mathbf{u}_{m+1}) \cdot \mathbf{n} = 0 \tag{2.22}$$

$$(\nabla \times \mathbf{u}_m - \nabla \times \mathbf{u}_{m+1}) \cdot \mathbf{n} = 0 \tag{2.23}$$

$$(\mathbf{u}_m - \mathbf{u}_{m+1}) \times \mathbf{n} = 0 \tag{2.24}$$

$$(\mu_m^{-1}\nabla \times \mathbf{u}_m - \mu_{m+1}^{-1}\nabla \times \mathbf{u}_{m+1}) \times \mathbf{n} = 0 \tag{2.25}$$

where $\mathbf{n}$ is the stack normal vector. In the considered case of non–magnetic materials we have $\mu_m = \mu$, $m = 0, \ldots N + 1$, where μ is the vacuum permeability. From eq. 2.24 and eq. 2.25 we obtain 4 conditions per interface that relate the fields at both sides of the interface These conditions complete the set of equations required to solve the scattering problem of a plane wave from the layer stack.

Properties of the finite element method and description the used software package

Finite element theory in general and for Maxwell's equations is covered in corresponding textbooks [Bra92; Mon03] and will not be derived here. In a brief summary, the finite element method allows to discretize and solve differential equations. First, the differential equation is integrated after multiplication with a test function. The application of the differential operator can subsequently be shifted to the test function by partial integration. Derivatives defined in such an integral sense can be shown to be unique if they exist, under the proper conditions for the test function space. A choice of test functions on compact carriers, which overlap in a neighbourhood, leads to a the transformation of the global problem, which is to compute the solution of a partial differential equation inside a computational domain under certain boundary conditions, into a system of coupled local problems. Usually the computational domain is discretized into geometric elements like triangles or tetrahedra. Local polynomials of a chosen degree, which are non-zero only within certain neighbouring elements, can then be used to build the test function space. In case of Maxwell's equations, a local integration of the partial differential equation leads to a linear system of coupling conditions between the localized test functions and to the boundary conditions at the computational domain boundary. This linear system can be solved by standard numerical methods and yields an approximation

to the solution of the partial differential equation, which converges to the analytic solution with refinement of the discretization and optionally the increase of the polynomial degree of the ansatz functions.

When the geometric discretization error of a material distribution is ignored, the most important quantity for error analysis is related to the polynomial degree p of the ansatz functions of the test space and a measure (length) of the finesse of the spacial discretization, h. The theory is covered e.g. by Braess [Bra92]. Convergence behaviour is dependent on many factors, as for example the chosen error norm. In an energy norm and for Maxwell's equations, the typically observed convergence behaviour, given by the interpolation of the solution by a piecewise polynomial, is

$$\text{error} \leq c \cdot h^{p+1}\,, \tag{2.26}$$

with a positive constant c. This means that, given a fixed discretization and polynomial degree which already capture properties the physical problem, exponential convergence of the solution is expected with increasing finite element polynomial degree. The above property is used for error measurement and quality assurance of the simulations in this thesis.

The finite element implementation used in all simulations within this thesis with complex 2D and 3D material distributions is developed as part of the finite element suite *JCMsuite* at the Zuse Institute Berlin. This finite element package focusses on simulation of linear optics in the high–frequency regime by solving the time–harmonic Maxwell's equations, eq. 2.15. Additional solvers are implemented in the package for linear elasticity and heat equations. The software is commercially distributed by the spin–off company *JCMwave*[2]. Main programmers of the implementation are Lin Zschiedrich and Jan Pomplun. The finite element implementation for solving Maxwell's equations in 3D is based on Nédélecs elements [Néd80] which prevent the existence of unphysical solutions in the interior domain. Details about the implementation can be found in reference [Pom+07] and in the PhD thesis of Lin Zschiedrich [Zsc09] and Jan Pomplun [Pom10]. The linear solver used internally for solving the finite element system is the direct sparse solver PARDISO [SG04].

In *JCMsuite*, transparent boundaries are implemented by an optionally adaptive PML method which ensures exponential damping of scattered fields in the exterior domain. The implementation is based on the work of Lin Zschiedrich [Zsc09] and allows the use of multiply structured exterior domains. Other available boundary conditions are periodic boundaries and Dirichlet boundary conditions for the electric and magnetic components of the field which can be used as mirror boundary conditions in cases of special symmetry of the geometry and incoming field.

[2] www.jcmwave.com

The specific features of the finite element solver used for this thesis were:

- Solution of scattering problems for Maxwell's equations on 2D and 3D computational domains with transparent and periodic boundaries.
- Solution of the eigenvalue problem for ω^2, E of Maxwell's equations in 3D on twofold periodic domains with transparent boundaries in the third dimension.
- Weighted superposition of previously computed fields.
- Post–processing capabilities. Typical functionals like the computation of volume integrals of the field energy or the surface integrals of the surface normal component of the Poynting vector were used. Further the built–in Fourier transform was used to obtain the Fourier spectra of reflected and transmitted fields in scattering simulations.

Calculation of the absorption inside a sub-volume of the computational domain

For the evaluation of absorptance, optical quantum efficiency and current generation of a solar cell it is necessary to calculate the absorption inside of sub–volumes of the computational domain. Physically this means that the work done by the electric field on the material distribution per unit time needs to be calculated. For a single charge q the electric force acting on the charge is the Lorentz force $\mathbf{F} = q(\mathbf{E} + \frac{\mathbf{v}}{c} \times \mathbf{B})$ and the work rate on a charge at velocity v is $P = q\mathbf{v} \cdot \mathbf{F} = q\mathbf{v} \cdot \mathbf{E}$. The work rate by an electric field $\mathbf{E}$ on a static impressed current distribution $\mathbf{j}$ can therefore be defined by [Jac99]

$$\int_V \mathbf{j} \cdot \mathbf{E} \, \mathrm{d}V \tag{2.27}$$

In the time harmonic context where a complex field notation is used for convenience the real part of the complex quantities needs to be taken before multiplication. A product of quantities $\mathbf{A}(\mathbf{r}, t) = \tilde{\mathbf{A}}(\mathbf{r})e^{-i\omega t}$, $\mathbf{B}(\mathbf{r}, t) = \tilde{\mathbf{B}}(\mathbf{r})e^{-i\omega t}$ therefore needs to be expanded as

$$\begin{aligned} \mathbf{A} \cdot \mathbf{B} &\equiv \frac{1}{4}[\tilde{\mathbf{A}}(x)e^{-i\omega t} + \tilde{\mathbf{A}}^*(x)e^{i\omega t}] \cdot [\tilde{\mathbf{B}}(x)e^{-i\omega t} + \tilde{\mathbf{B}}^*(x)e^{i\omega t}] \\ &= \frac{1}{2}\Re(\tilde{\mathbf{A}}^*(x) \cdot \tilde{\mathbf{B}}(x) + \tilde{\mathbf{A}}(x) \cdot \tilde{\mathbf{B}}(x)e^{-2i\omega t}) \end{aligned} \tag{2.28}$$

to obtain the physically correct quantity. In the case of a high frequency field the typical quantity of interest is the time average over one characteristic period. This reduces equation (2.28) to $\mathbf{A} \cdot \mathbf{B} = \frac{1}{2}\Re(\mathbf{A}^*(x) \cdot \mathbf{B}(x))$.

Using Ampère's law for time harmonic fields, cf. eq. 2.14, to substitute the current distribution and the vector identity $\nabla \cdot (\mathbf{A} \times \mathbf{B}) = \mathbf{B} \cdot (\nabla \times \mathbf{A}) - \mathbf{A} \cdot (\nabla \times \mathbf{B})$ to transform the work integral 2.27, we obtain

$$\begin{aligned} \underbrace{\frac{1}{2}\int_V \mathbf{J}^* \cdot \mathbf{E}\,\mathrm{d}V}_{I} &= \frac{1}{2}\int_V \mathbf{E} \cdot [\nabla \times \mathbf{H}^* - i\omega \mathbf{D}^*]\,\mathrm{d}V \\ &= \underbrace{\frac{1}{2}\int_V [-\nabla \cdot (\mathbf{E} \times \mathbf{H}^*)]\,\mathrm{d}V}_{III} + \underbrace{\frac{1}{2}\int_V [-i\omega(\mathbf{E} \cdot \mathbf{D}^* - \mathbf{B} \cdot \mathbf{H}^*)]\,\mathrm{d}V}_{II} \ . \end{aligned} \tag{2.29}$$

The above equation is the integral representation of Poynting's theorem of conservation of energy for time harmonic fields.

With definition of the complex Poynting vector and electric as well as magnetic field energy densities

$$\mathbf{S} = \frac{1}{2}(\mathbf{E} \times \mathbf{H}^*),\ w_e = \frac{1}{4}(\mathbf{E} \cdot \mathbf{D}^*),\ w_m = \frac{1}{4}(\mathbf{B} \cdot \mathbf{H}^*)$$

equation 2.29 can be rewritten as [Jac99]

$$\underbrace{\frac{1}{2}\int_V \mathbf{J}^* \cdot \mathbf{E}\,dV}_{\mathrm{I}} + \underbrace{2i\omega \int_V (w_e - w_m)\,dV}_{\mathrm{II}} + \underbrace{\int_{S(V)} \mathbf{S} \cdot \mathbf{n}\,da}_{\mathrm{III}} = 0 \ . \tag{2.30}$$

Here, Gauss's divergence theorem was applied to transform term III into a surface integral. $S(V)$ is the surface enclosing V and $\mathbf{n}$ the surface normal on the infinitesimal surface element da.

In the case of zero impressed currents term I of equation (2.30) vanishes. The real part of the two remaining terms represent the conservation of energy in lossy media (i.e. with $\Im(\varepsilon) \neq 0$ or $\Im(\mu) \neq 0$). Losses inside V which are represented by term II must equal the negative of the change of the net energy flux through $S(V)$ (term III). The absorption inside a volume V can thus be calculated from 2.30.II as

$$(\text{Absorption})_V = 2\omega \int_V (\Im(w_e) - \Im(w_m))\,dV \ . \tag{2.31}$$

In the problems considered within this thesis, no material is magnetically dissipative, i.e.

$\Im(w_m) = 0$. Alternatively to 2.31 we can calculate the absorption from term 2.30.III,

$$(\text{Absorption})_V = \int_{S(V)} \mathbf{S} \cdot \mathbf{n}\, da \tag{2.32}$$

$$= \int_V \nabla \cdot \mathbf{S}\, dV\,. \tag{2.33}$$

Using the surface integral 2.32 should always result in lower resource consumption during computation. However, if in case of the surface integral the quality of the input data, i.e. the calculated field values, has to be higher for a comparable error in the computed absorption, using the volume integral may become the better choice. It should be noted here that whereas in 2D volume integration and factorization of the FEM matrix have about the same computational costs, the quadrature is less computational intensive than the matrix factorization in the 3D case. It can be seen that we have to expect a loss in precision when calculating the integrand of the surface integral, rendering this method impractical in 3D cases. Having a closer look on how the integrands are calculated from the electric field, we see that, in case of isotropic permittivities, the electric field energy density is simply proportional to the local permittivity and intensity of the field[Nol90],

$$w_e(\mathbf{r}) = \frac{1}{4}\mathbf{E}(\mathbf{r})^* \cdot \mathbf{D}(\mathbf{r}) \tag{2.34}$$

$$= \frac{1}{4}\mathbf{E}(\mathbf{r})^* \cdot (\varepsilon_r(\mathbf{r})\varepsilon_0\mathbf{E}(\mathbf{r})) \tag{2.35}$$

$$= \frac{1}{4}\varepsilon_r(\mathbf{r})\varepsilon_0 I(\mathbf{r})\,. \tag{2.36}$$

The time averaged Poynting vector required to calculate the surface integral is defined as[Nol90]

$$\mathbf{S}(\mathbf{r}) = \frac{1}{2\mu_r\mu_0}\Re\left\{\mathbf{E}(\mathbf{r}) \times \mathbf{B}(\mathbf{r})\right\}\,. \tag{2.37}$$

As Maxwell's equations are typically only solved for the electric field, the magnetic field for computation of eq. 2.37 has to be derived from eq. 2.16. The derivative that has to be taken in this step leads to a loss of one order in the polynomial representation of the **H** field. No precision is lost, when computing the absorption from the field energy in eq. 2.36. Another factor that makes the use of the surface integral, eq. 2.32, unattractive is that regions with high local errors are often found at material interfaces. In cases where absorption is more a volume effect than a localized effect close to interface boundaries we can expect the volume integral to converge much quicker to a satisfying error level than the surface integral representation.

The difference in the convergence of the two absorption integral representations can be

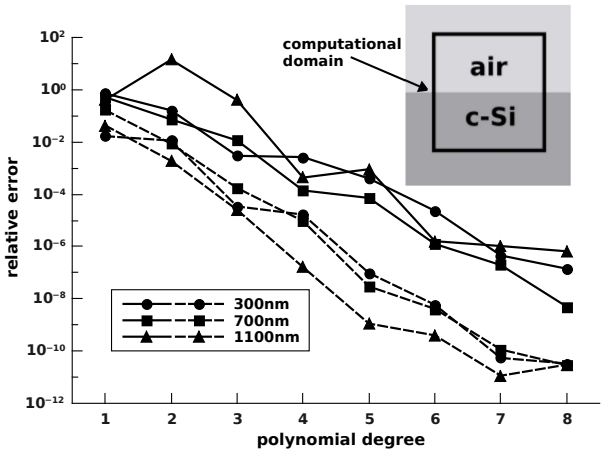

Figure 2.6.: *Convergence of the two post processing variants to obtain the absorbed field energy. The computational domain is depicted in the inset. Errors are computed against the analytic solution for a fixed triangular discretization and increasing polynomial degree of the finite element ansatz functions (see p. 26 for expectations on finite element convergence behaviour). Dashed lines represent the convergence of the volume integral (eq. 2.31) and full lines the convergence of the surface integral (eq. 2.32) formulation of absorption.*

made clear by a very simple example. The inset in Fig. 2.6 shows the computational domain which is centered at the interface between a half space of air and a half space of crystalline silicon. For a few exemplary wavelengths between 300 nm and 1100 nm the electric field was computed using an edge length ≤ 0.5 wavelengths and polynomial degrees from 1 up to 8. The absorption inside the silicon volume enclosed by the computational domain was calculated using eqs. 2.31 and 2.32 for all field solutions. Errors of the individual results with respect to analytic values are shown in Fig. 2.6. It is evident that the volume integral converges faster and moreover already has a smaller error at low finite element degrees. For geometries with field singularities at the interfaces between materials the difference between the two processing methods gets more pronounced than in this well-behaved case. Eq. 2.31 was chosen to obtain absorption values in all simulations in this thesis.

2.2.2. Justification of a plane wave model light source

The sun is an extended, spatially–incoherent thermal light source. In rigorous simulation of solar cells it is usually modeled by an incoming plane wave which which is completely coherent and has a well–defined polarization. The following subsections motivate why the plane wave model is justified for modeling of thin film solar cell optics.

The first subsection shows how to obtain polarization incoherence in rigorous simulation.

The following subsections discuss the spatial coherence properties of spectrally filtered sunlight on earth. This is done along with an introduction into the optical coherence theory of wave fields mainly developed by Emil Wolf and Leonard Mandel.

Scattering of an unpolarized plane wave

Scattering of a totally unpolarized plane wave, i.e. an incoherent average of plane waves of all possible states of polarization, can easily be achieved in rigorous simulation of Maxwell's equations. We start by decomposing the incoming plane wave into two perpendicular fields,

$$\begin{aligned} \mathbf{E^{inc}}(\mathbf{r}) &= \mathbf{E}_1^{\mathbf{inc}}(\mathbf{r}) + \mathbf{E}_2^{\mathbf{inc}}(\mathbf{r}) \\ \mathbf{E}_1^{\mathbf{inc}}(\mathbf{r}) \cdot \mathbf{E}_2^{\mathbf{inc}}(\mathbf{r}) &= 0 \ . \end{aligned} \tag{2.38}$$

The scattered field can then be written in a similar form,

$$\mathbf{E^{sc}}(\mathbf{r}) = \mathbf{E}_1^{\mathbf{sc}}(\mathbf{r}) + \mathbf{E}_2^{\mathbf{sc}}(\mathbf{r}) \ , \tag{2.39}$$

only that the fields $\mathbf{E}_1^{\mathbf{sc}}(\mathbf{r})$, $\mathbf{E}_2^{\mathbf{sc}}(\mathbf{r})$ can not be assumed generally perpendicular any more. Hence, the intensity of the scattered field is

$$\begin{aligned} I^{sc}(\mathbf{r}) = |\mathbf{E}^{sc}(\mathbf{r})|^2 &= |\mathbf{E}_1^{sc}(\mathbf{r})|^2 + |\mathbf{E}_2^{sc}(\mathbf{r})|^2 \\ &+ \underbrace{2\left[\Re(\mathbf{E}_1^{sc}(\mathbf{r}))\Re(\mathbf{E}_2^{sc}(\mathbf{r})) + \Im(\mathbf{E}_1^{sc}(\mathbf{r}))\Im(\mathbf{E}_2^{sc}(\mathbf{r}))\right]}_{\neq 0 \text{ in general}} \end{aligned} \tag{2.40}$$

where $\Re$ and $\Im$ denote real and imaginary part, respectively.

To obtain an incoherent average over all possible states of polarization, we assume the fields $\mathbf{E}_1^{\mathbf{inc}}(\mathbf{r})$, $\mathbf{E}_2^{\mathbf{inc}}(\mathbf{r})$ to be normalized and define the incoming field

$$\mathbf{E^{inc}}(\mathbf{r};\varphi) = a(\sin\varphi \mathbf{E}_1^{\mathbf{inc}}(\mathbf{r}) + \cos\varphi \mathbf{E}_2^{\mathbf{inc}}(\mathbf{r})) \ , \tag{2.41}$$

with a complex amplitude a, and average the intensity 2.40 of the scattered field over φ,

$$\langle I^{sc}(\mathbf{r})\rangle_\varphi = \frac{1}{2\pi}|a|^2 \int_0^{2\pi} \Big\{ \sin^2\varphi |\mathbf{E}_1^{sc}(\mathbf{r})|^2 + \cos^2\varphi |\mathbf{E}_2^{sc}(\mathbf{r})|^2 \tag{2.42}$$

$$+2\sin\varphi\cos\varphi\left[\Re(\mathbf{E}_1^{sc}(\mathbf{r}))\Re(\mathbf{E}_2^{sc}(\mathbf{r})) + \Im(\mathbf{E}_1^{sc}(\mathbf{r}))\Im(\mathbf{E}_2^{sc}(\mathbf{r}))\right]\Big\} \ d\varphi \tag{2.43}$$

$$= \frac{1}{2}|a|^2(|\mathbf{E}_1^{sc}(\mathbf{r})|^2 + |\mathbf{E}_2^{sc}(\mathbf{r})|^2) \ . \tag{2.44}$$

So the incoherent average over all possible states of polarization may be obtained simply by

computing the incoherent average for any two perpendicular polarizations of the incoming plane wave, for any geometry. This can also be shown by the addition property of coherency matrices [Won05, p. 101].

In certain cases the incoherent averaging over perpendicularly polarized incoming sources is not necessary:

- If the geometry is isotropic like a rough surface and the electromagnetic field is normally incident, a change of polarization direction does not change the result.
- If the geometry is periodic with a four–fold mirror symmetric unit cell and the electromagnetic field is normally incident, then the solution is symmetric with respect to a 90° rotation of the polarization of the incoming light.

These are the two cases which were encountered throughout the simulations done for the work of this thesis.

Quantification of optical coherence and propagation laws

For further discussion of coherence properties in experimental settings it is useful to introduce a mathematical quantification of coherence by means of a correlation of signals. This theory was developed mainly by Emil Wolf and Leonard Mandel. It is briefly introduced in this section as the results will be used for discussion in the following subsections. The derivation included hereunder is described in more detail in [BW59, p. 500; MW65, p. 237].

A two point correlation which quantifies the coherence of two complex signals can be derived from the double slit experiment, depicted schematically in Fig. 2.7. We assume the field $V(\mathbf{r}, t)$ to be a physical solution of the Helmholtz equation at a point $\mathbf{r}$ at time t. The field is created by two disturbances at the points $\mathbf{r}_1$, $\mathbf{r}_2$. Due to the superposition principle the instantaneous field at $\mathbf{r}_d$ can be written as

$$V(\mathbf{r}_d, t) = K_1 V(\mathbf{r}_1, t - t_1) + K_2 V(\mathbf{r}_2, t - t_2)$$

where V denotes the primary field and $K_i,\ i = 1, 2$, are factors combining the deterministic disturbance at $\mathbf{r}_1$, $\mathbf{r}_2$ and the translation of the field to the point $\mathbf{r}_d$. The two time constants t_1, t_2 are the communication times of the signals to the detector point $\mathbf{r}_d$. A homogenous non–dispersive medium with a speed of light c will be assumed in the following. The propagation times are then dependent only on spatial distance and not position. V is further assumed to

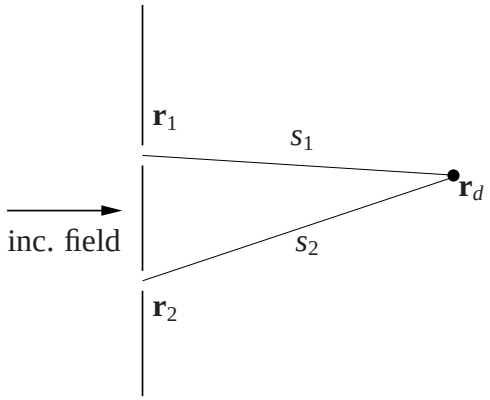

Figure 2.7.: *The double slit interference experiment.*

be the complex analytic description of the real field field[3]. The intensity at point $\mathbf{r}_d$ is hence given by

$$\begin{aligned} I(\mathbf{r}_d,t) =& V^*(\mathbf{r}_d,t)V(\mathbf{r}_d,t) \\ =& |K_1|^2 I(\mathbf{r}_1,t-t_1) + |K_2|^2 I(\mathbf{r}_2,t-t_2) \\ &+ 2\Re\{K_1^* K_2 V^*(\mathbf{r}_1,t-t_1)V(\mathbf{r}_2,t-t_2)\}, \end{aligned} \tag{2.45}$$

with $\Re$ denoting the real part. If we now take an ensemble average of different realizations of the field, denoted by $\langle\cdot\rangle_e$, we obtain

$$\begin{aligned} \langle I(\mathbf{r}_d,t)\rangle_e =& |K_1|^2\langle I(\mathbf{r}_1,t-t_1)\rangle_e + |K_2|^2\langle I(\mathbf{r}_2,t-t_2)\rangle_e \\ &+ 2\Re\{K_1^* K_2 \Gamma(\mathbf{r}_1,\mathbf{r}_2,t-t_1,t-t_2)\} \end{aligned} \tag{2.46}$$

where

$$\Gamma(\mathbf{r}_1,\mathbf{r}_2,t-t_1,t-t_2) = \langle V^*(\mathbf{r}_1,t-t_1)V(\mathbf{r}_2,t-t_2)\rangle_e \tag{2.47}$$

represents the correlation between the field at $(\mathbf{r}_1,t-t_1)$ and $(\mathbf{r}_2,t-t_2)$. We further note that $\langle I(\mathbf{r}_1,t-t_1)\rangle_e = \Gamma(\mathbf{r}_1,\mathbf{r}_1,t-t_1,t-t_1)$.

Under assumption of statistical stationarity, i.e. independence of the time origin, and ergodicity $\Gamma(\mathbf{r}_1,\mathbf{r}_2,t_1,t_2)$ is only dependent on the time difference $\tau = t_1 - t_2 = (s_1 - s_2)/c$,

$$\Gamma(\mathbf{r}_1,\mathbf{r}_2,\tau) = \lim_{T\to\infty}\frac{1}{2T}\int_{-T}^{T} V^*(\mathbf{r}_1,t)V(\mathbf{r}_2,t+\tau)dt \tag{2.48}$$

[3] The complex analytic field V(**r**, t) is defined from the Fourier transform of the real signal $V^{(r)}(\mathbf{r},t) = \int_{-\infty}^{\infty} v(\mathbf{r},\omega)e^{-i\omega t}d\omega$, where $v(\mathbf{r},\omega) = v^*(\mathbf{r},-\omega)$, by omitting the negative frequencies which do not hold any additional information: $V(\mathbf{r},t) = \int_0^{\infty} v(\mathbf{r},\omega)e^{-i\omega t}d\omega$

and the ensemble average is equal to the time average, $\langle\cdot\rangle_e = \langle\cdot\rangle_t$ which will further only be denoted by $\langle\cdot\rangle$. Eq. 2.46 can thus be rewritten as

$$\begin{aligned}\langle I(\mathbf{r}_d,t)\rangle =& |K_1|^2\langle I(\mathbf{r}_1,t)\rangle + |K_2|^2\langle I(\mathbf{r}_2,t)\rangle \\ &+ 2\Re\{K_1^* K_2 \Gamma(\mathbf{r}_1,\mathbf{r}_2,\tau)\}\,.\end{aligned} \tag{2.49}$$

For the sun and in typical measurements on solar cells the simultaneous realization of the ensemble required for ergodicity and the time independence of measurement required by stationarity are provided. Integration times are much longer than the typical time interval of field fluctuations and are done on stationary states. The function $\Gamma(\mathbf{r}_1,\mathbf{r}_2,\tau)$ was introduced by Wolf and is commonly known as *mutual coherence function*. It describes the correlation of signals from two sources at $\mathbf{r}_1$, $\mathbf{r}_2$ as a function of the time difference τ of wave propagation to a point $\mathbf{r}_d$.

By Fourier transform (see also footnote 3 and [MW65, p. 240])

$$\Gamma(\mathbf{r}_1,\mathbf{r}_2,\tau) = \int_0^\infty W(\mathbf{r}_1,\mathbf{r}_2,\omega)e^{-i\omega\tau}d\omega \tag{2.50}$$

a similar quantity W called *mutual spectral density* can be defined in frequency space.

The normalized quantity

$$\gamma(\mathbf{r}_1,\mathbf{r}_2,\tau) = \frac{\Gamma(\mathbf{r}_1,\mathbf{r}_2,\tau)}{\sqrt{\Gamma(\mathbf{r}_1,\mathbf{r}_1,0)}\sqrt{\Gamma(\mathbf{r}_2,\mathbf{r}_2,0)}} \tag{2.51}$$

known as the *complex degree of coherence* measures the coherence as a correlation on the scale between zero and one.

As V has been assumed a solution to a Helmholtz equation, Γ and W are solutions to a set of two Helmholtz equations. These take the most simple form for the *mutual spectral density* W [MW95, p. 183]. The propagation of the *mutual spectral density* from a plane into a half space can be solved as a Dirichlet boundary value problem to the Helmholtz equation using the Green's function. The calculation is given in [MW95, p. 185] and yields the propagation integral

$$\begin{aligned}W(\mathbf{r}_1,\mathbf{r}_2,\omega) = &\left(\frac{k}{2\pi}\right)^2 \int_{z=0}\int_{z=0} W(\mathbf{r}_1',\mathbf{r}_2',\omega)\left[1+\frac{i}{k}\left(\frac{1}{R_2}-\frac{1}{R_1}\right)+\frac{1}{k^2}\frac{1}{R_1R_2}\right] \\ &\times \frac{e^{ik(R_2-R_1)}}{R_1R_2}\cos\theta_1\cos\theta_2\; d^2\mathbf{r}_1' d^2\mathbf{r}_2'\;, \\ &R_i = |\mathbf{r}_i - \mathbf{r}_i'|,\;\; i=1,2,\end{aligned} \tag{2.52}$$

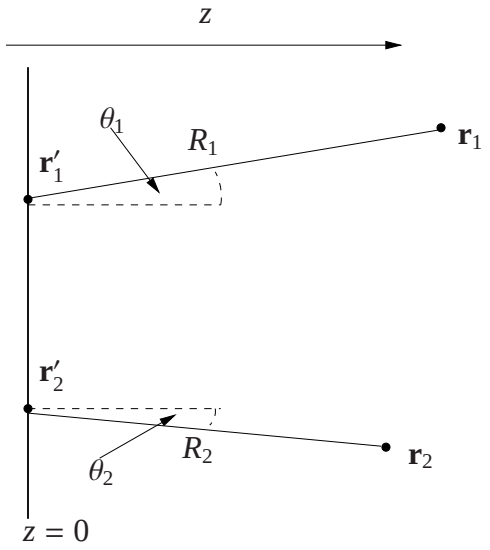

Figure 2.8.: *Propagation of mutual coherence from plane $z = 0$ to two points $\mathbf{r}'_{1,2}$ in an adjacent half space.*

for the case depicted in Fig. 2.8.

When the coherence information is transferred to a plane far from $z = 0$, i.e. the separation of the two planes is large compared to the wavelength $\lambda = \frac{c}{\omega}$ and hence $R_i \gg \lambda,\ i = 1, 2$ or $\frac{1}{R_i} \ll k,\ i = 1, 2$. Equation 2.52 can then be approximated by

$$W(\mathbf{r}_1, \mathbf{r}_2, \omega) \approx \left(\frac{k}{2\pi}\right)^2 \int_{z=0} \int_{z=0} W(\mathbf{r}'_1, \mathbf{r}'_2, \omega) \frac{e^{ik(R_2 - R_1)}}{R_1 R_2} \cos\theta_1 \cos\theta_2 \, d^2\mathbf{r}'_1 d^2\mathbf{r}'_2 \, . \tag{2.53}$$

The propagation integral for the *mutual coherence function* can be derived from equation 2.52 by applying the definition 2.50. The terms within the rectangular braces in 2.52 can be transformed into time derivatives. After interchanging the order of the frequency integral and the time derivatives and a second application of 2.50, we obtain (cf. again [MW95, p. 185])

$$\Gamma(\mathbf{r}_1, \mathbf{r}_2, \tau) = \left(\frac{1}{2\pi}\right)^2 \int_{z=0} \int_{z=0} \frac{\cos\theta_1 \cos\theta_2}{(R_1 R_2)^2} \mathfrak{D}\Gamma\left(\mathbf{r}'_1, \mathbf{r}'_2, \tau - \frac{R_2 - R_1}{c}\right) d^2\mathbf{r}'_1 d^2\mathbf{r}'_2 \, , \tag{2.54}$$

with the differential operator $\mathfrak{D} = (1 + \frac{R_2 - R_1}{c} \frac{\partial}{\partial \tau} - \frac{R_2 R_1}{c^2} \frac{\partial^2}{\partial \tau^2})$. In case of the approximation for large distances, only the second time derivative is taken into account.

Further simplifications can be applied for light with a narrow bandwith as provided by a bandfilter, like a monochromator. The integral eq. 2.50 can be rewritten in the form

$$\Gamma(\mathbf{r}_1, \mathbf{r}_2, \tau) = \int_{-\omega_0}^{\infty} \tilde{W}(\mathbf{r}_1, \mathbf{r}_2, \mu) e^{-i\mu\tau} d\mu \tag{2.55}$$

with $\mu = \omega - \omega_0$. In the case of a limited bandwidth $\Delta\omega$ around ω_0, $\tilde{W}(\mathbf{r}_1, \mathbf{r}_2, \mu)$ will only take significant values around $\mu = 0$, i.e. for low frequencies $\mu < \Delta\omega$. If $\Delta\omega/\omega \ll 1$, $\Gamma(\mathbf{r}_1, \mathbf{r}_2, \tau) = \tilde{\Gamma}(\mathbf{r}_1, \mathbf{r}_2, \tau)e^{-i\omega_0\tau}$ is the product of a slowly varying part and a rapidly oscillating part at frequency ω_0. An electromagnetic field which satisfies $\Delta\omega/\omega \ll 1$ is called *quasi–monochromatic*.

In the following we assume the source to be quasi–monochromatic with a central frequency ω_0. We further assume two different sourcepoints to be totally uncorrelated. Under these assumptions the *mutual coherence function* of the primary source may be written as [MW65, p. 255f]

$$\Gamma(\mathbf{r}_1, \mathbf{r}_2, \tau) \sim I(\mathbf{r}_1)\delta(\mathbf{r}_1 - \mathbf{r}_2)e^{-i\omega_0\tau} \tag{2.56}$$

where $I(\mathbf{r})$ is the average radiant intensity of the source point $\mathbf{r}$. The large distance condition for the simplified version of the propagation of the *mutual spectral density* 2.53 is assumed to be fulfilled. We further assume a homogenous circular light source and

$$\frac{\rho}{R} \ll 1\,,$$

where ρ and R are radius of and distance to the light source, respectively. The cosine in eq. 2.54 can then be approximated as $\cos\theta_i = \frac{R^2}{R^2+\rho^2} = \frac{1}{1+(\rho/R)^2} \approx 1,\ i = 1, 2,$. We further consider only time arguments much smaller than the coherence time $|\tau - (R_2 - R_1)/c| \ll 2\pi/\Delta\omega$. Under these assumptions eq. 2.54 can be approximated by

$$\Gamma(\mathbf{r}_1, \mathbf{r}_2, \tau) \sim \left(\frac{k_0}{2\pi}\right)^2 e^{-i\omega_0\tau} \int_\sigma \frac{I(\mathbf{r}')}{(R_1R_2)^2} e^{-ik_0(R_2-R_1)}\, d^2\mathbf{r}' \tag{2.57}$$

where $R_i = |\mathbf{r}_i - \mathbf{r}'|,\ i = 1, 2$, and the radiating area in the source plane is σ. Eq. 2.57 is known as the *van Cittert-Zernike theorem*. A further simplification can be applied to eq. 2.57 in the case of normal incidence, which is most interesting in case of the simulations for photovoltaic applications. If the points $\mathbf{r}_1,\ \mathbf{r}_2$ are located in a plane parallel to σ at distance R from the primary source plane and small differences $|\mathbf{r}_1 - \mathbf{r}_|/R \ll 1$ and a uniform and circular source of radius ρ are assumed, the *complex degree of coherence* is given by the Bessel function of the first kind and the first order,

$$\gamma(\mathbf{r}_1, \mathbf{r}_2, \tau) = [2J_1(v)/v]e^{i(\Psi-\omega_0\tau)},\ |\tau| \ll 2\pi/\Delta\omega\,, \tag{2.58}$$

with $\Psi = k_0[(x_2^2 + y_2^2) - (x_1^2 + y_1^2)]/2R$ and $v = (k_0\rho/R)\sqrt{(x_2 - x_1)^2 + (y_2 - y_1)^2}$.

In instrumental optics $|\gamma| > 0.88$ is regarded as fully coherent which equals the condition

$v < 1$ or

$$|\mathbf{r}_1 - \mathbf{r}_2| < 0.16\lambda_0 \frac{R}{\rho}\,. \tag{2.59}$$

This result and eq. 2.57 will be used for further discussion.

Thermal light sources

Thermal light sources are usually assumed to have a Gaussian probability distribution of the field amplitude (not meaning the spectral distribution, but the amplitude distribution for a single wavelength). As the field amplitude at any point in space is composed from contributions of many independent random radiators, a Gaussian joint probability distribution is suggested by application of the central limit theorem, cf. eq. 2.92. For black body radiation the Gaussian distribution can also be derived from quantum mechanical considerations[MW65, p. 249]. Gaussian probability distributions have specific properties. All odd-order moments are zero. The highest cumulant is of second order and all even order moments are functions of the mean value and the second order moment only. So the coherence phenomena of thermal light are effectively fully described by the two point correlation function Γ derived above.

The sun as a light source on earth

The above result for the lateral coherence of spectrally filtered light, which is not completely coherent also for arbitrarily small spectral width due to the spatial incoherence of the source, can be straightforward applied to the sun.

The sun lies at a distance of $R = 1.496 \cdot 10^{11}$m from the earth. Its radius is $\rho = 0.5 \cdot (1.392 \cdot 10^6$m). The lateral length scale at which light can interact in the photovoltaic applications considered here is mainly limited by the absorption of silicon which should be almost complete to the order of 10^{-2} m (cf. Fig. 2.4). This is also the distance at which multiple reflections within a millimeter thick superstrate would relate surface areas of the solar cell. The vertical deviation of the wave front of light of a point source at the distance to the sun

$$\Delta_z(\Delta_{xy}) = R - \sqrt{R^2 - \Delta_{xy}^2} \approx \frac{1}{2}\frac{x^2}{R} \tag{2.60}$$

at this typical distance is

$$\Delta_z(10^{-2}\,\mathrm{m}) < 10^{-6}\,\mathrm{nm}\,. \tag{2.61}$$

This result is very small compared to the wavelength of light. A plane wave front can therefore be assumed to be a good approximation.

Considering the lateral coherence the requirements for application of the van Cittert–Zernike theorem, eq. 2.57, can be seen as provided as

$$\rho/R \approx \frac{1.392 \cdot 10^6 \mathrm{m}/2}{1.496 \cdot 10^{11} \mathrm{m}} \approx 4.7 \cdot 10^{-6} \ll 1\,.$$

From relation 2.59 and at a wavelength of $\lambda_0 = 800\,\mathrm{nm}$ we can assume points in a lateral distance up to

$$\delta_{\text{lateral, limit}} = 2.7\,\mathrm{cm} \tag{2.62}$$

as strongly correlated.

Considering the longitudinal coherence it is obvious from the time argument in the integrand of eq. 2.54 that the longitudinal coherence interval should be larger than the lateral interval. To approximate the longitudinal coherence interval we again assume a circular and uniform source to make eq. 2.57 applicable. We now consider two points along the normal direction through the center of the source with

$$R_1 = \sqrt{\rho^2 + d^2} \tag{2.63}$$

$$R_2 = \sqrt{\rho^2 + (d + \Delta d)^2} \tag{2.64}$$

where ρ is the radial coordinate from the source center and d, $(d + \Delta d)$ the normal distances of the two source points to the source. We define $\rho' = \sqrt{1 + \frac{\rho^2}{d^2}} \geq 1$ and rewrite the above as

$$R_1 = d\rho' \tag{2.65}$$

$$R_2 = d\sqrt{\rho'^2 + \frac{2\Delta d}{d} + \left(\frac{\Delta d}{d}\right)^2}. \tag{2.66}$$

Under the assumption that $\frac{\Delta d}{d} \ll 1$ we obtain

$$R_2 \approx d\rho' + \frac{\Delta d}{\rho'} + O\left(\frac{\Delta d}{d}\right) \tag{2.67}$$

and are able to evaluate

$$R_2 - R_1 \approx \frac{\Delta d}{\rho'}, \tag{2.68}$$

$$\frac{d^2}{R_1 R_2} \approx \frac{1}{\rho'^2 + \frac{\Delta d}{d}} \tag{2.69}$$

where we again neglect the term of $\frac{\Delta d}{d}$ in the denominator. In the following we want to relate two secondary sources at their respective positions, i.e. given the situation $\tau = \frac{\Delta d}{c}$. With the assumption of a circular homogenous source and the relations $\rho(\rho') = d\sqrt{\rho'^2 - 1}$ and $\frac{\partial \rho}{\partial \rho'} = \frac{\rho' d}{\sqrt{\rho'^2 - 1}}$ we can approximate the integrand in eq. 2.57 as

$$\Gamma(\mathbf{r}_1, \mathbf{r}_2, \tau) \propto \int_0^{\rho_{\text{sun}}} \rho \frac{1}{R_1 R_2} e^{-ik_0(R_2 - R_1)}\, d\rho \tag{2.70}$$

$$= \int_1^{\sqrt{1+(\rho_{\text{sun}}/d)^2}} \frac{1}{\rho'} e^{-i\omega_0 \tau \frac{1}{\rho'}}\, d\rho' \,. \tag{2.71}$$

The above formulation was evaluated numerically using Gauss–Kronrod quadrature rule. The resulting curve $|\gamma|$ is of a similar shape as eq. 2.58. Applying the coherence interval condition $|\gamma| = 0.88$ from instrumental optics the longitudinal coherence interval evaluates to

$$\delta_{\text{longitudinal, limit}} \approx 20\,\text{km} \tag{2.72}$$

for light at a wavelength of $\lambda = 800\,\text{nm}$. This interval is far longer than the vertical or lateral dimension of the solar cell.

Conclusion: No special limit on spectral width was taken into account to compute the results on lateral and longitudinal coherence. The results are dependent only on the spatial incoherence of the source and geometric parameters. From the above considerations a plane wave is a suitable source model for rigorous simulation which is close to the conditions generated by spectrally filtered sunlight. Spatial coherence properties of the primary source do not need to be considered any further. When required by the simulated geometry, incoherence of the polarization can easily be modeled by incoherent averaging of two perpendicular states of polarization.

2.2.3. Incoherent superstrate coupling

The polycrystalline solar cells which where of interest during the work on this thesis are suitable for deposition in the superstrate layout, cf. section 2.1.4. In this case the illumination takes place through the millimeter thick glass layer on which the thin film solar cells were deposited. Total internal reflection of light at the glass / air interface leads to a superstrate light trapping effect which may result in additional absorption and hence a higher current generation in the solar cell. The superstrate is by far too thick to be included in the finite element domain. It is further only 1D structured and can therefore be represented by a transfer matrix solver,

as described in section 2.2.1. This 1D problem was coupled to the finite element problem of the textured solar cell in an iterative way. As described in section 2.2.2 the rigorous solution of the solar cell system for incoming sunlight with a very narrow bandwidth filter also needs to include all interference effects caused by the resonances within the glass superstrate. The typical measurement setup employs a larger bandwidth and is discussed hereunder.

The superstrate coupling implemented for the simulations in this thesis does not represent a completely incoherent coupling of the superstrate. This choice had to be made for reasons of computational effort. The implemented coupling algorithm will be dicussed in more detail in the following subsections. However, also a completely incoherent coupling will not describe the experimental case correctly. The only way of computing the experimental result is by using a fine wavelength sampling and incoherent averaging over the experimental bandwidth.

A thick planar resonator in view of a typical monochromator bandwidth

If the bandwidth of thermal light employed for measurement is not very narrow the rigorous solution at a single wavelength is still valid but an incoherent averaging needs to be carried out over a characteristic ensemble of states to obtain results which are comparable to the experiment. This can be achieved by computing an incoherent average over the wavelength range of the measurement device. Typical measurement setups use monochromators with a finite bandwidth of at least a few nanometers in the visible and near–infrared range. The employed light sources are usually high pressure gas lamps which emit a broad thermal light spectrum and hence need to be treated as incoherent light sources.

We first consider a planar resonator as the superstrate model. The interferometric free spectral range of a planar resonator is defined as

$$\Delta\lambda(\lambda,\theta) \approx \frac{\lambda^2}{2nl\cos(\theta)} \tag{2.73}$$

where θ is the propagation angle, n the refractive index and l the thickness of the superstrate layer. The free spectral range is larger for higher wavelength and propagation angle. Assuming a glass superstrate thickness of $l = 1\,\text{mm}$, $\lambda = 1100\,\text{nm}$, $\theta = 85°$ and n=1.52 the free spectral range is still $\Delta\lambda < 5\,\text{nm}$. For propagation angles $\theta < 60°$ we have $\Delta\lambda < 0.8\,\text{nm}$. Modes propagating under large angles are only highly occupied in rare cases. If we assume a wavelength independent typical bandwidth of $\Delta\lambda_{\text{monochromator}} = 5\,\text{nm}$ of the light passing the monochromator also light propagating under very high propagation angles is averaged over more than one period of the interference pattern. In the following the coherent coupling will

first be explained. Then the incoherent coupling conditions, which result from wavelength averaging, will be derived and discussed.

Coherent coupling of two sub–domains

Coherent coupling of two sub–domains can be achieved iteratively using an additive Schwarz iteration [Bjø88; Sch+07]. In the two domain case the iteration is started from the decoupled case and keeps adding scattered fields of the subdomains to the incoming field of the respective other subdomain until a desired level of convergence is reached. In the following the two subdomains will be denoted by subscripts 1, 2, iterations will be denoted by superscripts in braces. The two linear operators calculating the scattered field of a subdomain towards the other subdomain will be denoted by $A_{1,2}$. The initially incoming fields are denoted by $i_{1,2}$ and the scattered fields in iteration n by $u_{1,2}^{(n)}$. The iteration is initialized by

$$u_1^{(0)} = A_1 i_1 \tag{2.74}$$

$$u_2^{(0)} = A_2 i_2 \tag{2.75}$$

and then carried out as

$$u_1^{(n+1)} = A_1(i_1 + u_2^{(n)}) \tag{2.76}$$

$$u_2^{(n+1)} = A_2(i_2 + u_1^{(n)}) \tag{2.77}$$

until the convergence level is reached. In the case where $i_2 = 0$ the n-th iteration reflected field from domain 1 can be written as

$$u_1^{(n)} = \left(1 + \sum_{j=1}^{n-1} (A_1 A_2)^j\right) u_1^{(1)} . \tag{2.78}$$

Using this form the integrated intensity $I_1^{(n)}$ of the field $u_1^{(n)}$ is

$$I_1^{(n)} = u_1^{(n)*} u_1^{(n)} \tag{2.79}$$

$$= u_1^{(1)*} \left(1 + \sum_{j=1}^{n-1} (A_2^* A_1^*)^j\right)\left(1 + \sum_{j=1}^{n-1} (A_1 A_2)^j\right) u_1^{(1)} \tag{2.80}$$

$$= u_1^{(1)*} \Bigg(1 \tag{2.81}$$

$$+ \sum_{j=1}^{n-1} (A_2^* A_1^*)^j + \sum_{k=1}^{n-1} (A_1 A_2)^k \tag{2.82}$$

$$+ \sum_{l=1}^{n-1} \sum_{\substack{m=1 \\ l \neq m}}^{n-1} (A_2^* A_1^*)^l (A_1 A_2)^m \tag{2.83}$$

$$+ \sum_{l=1}^{n-1} (A_2^* A_1^*)^l (A_1 A_2)^l \Bigg) u_1^{(1)} \tag{2.84}$$

where $\cdot^*$ denotes the complex conjugate transpose.

Incoherent averaging under the condition of a separation of scales

In case of the solar cell we assume a very narrow free spectral range for the superstrate, as already discussed above. For incoherent decoupling the textured solar cell is assumed to have a wavelength independent response in a sufficiently large wavelength interval around the central wavelength. We denote the operator of this wavelength independent domain by subscript $\cdot_1$ and the wavelength dependent operator representing the superstrate by $\cdot_2$. Wavelength integrating eq. 2.79 over the interval $\Delta\lambda_{\text{source}}$ around λ_{source} we get

$$\begin{aligned} \frac{1}{\Delta\lambda_{\text{source}}} \int_{\lambda_{\text{source}}-\Delta\lambda_{\text{source}}/2}^{\lambda_{\text{source}}+\Delta\lambda_{\text{source}}/2} I_1^{(n)}(\lambda) d\lambda &= \underbrace{\left|u_1^{(1)}\right|^2}_{\text{I}} \\ + \underbrace{\frac{1}{\Delta\lambda_{\text{source}}} \int_{\lambda_{\text{source}}-\Delta\lambda_{\text{source}}/2}^{\lambda_{\text{source}}+\Delta\lambda_{\text{source}}/2} \left[\sum_{k=1}^{n-1} \left|(A_1 A_2(\lambda))^k u_1^{(1)}\right|^2\right] d\lambda}_{\text{II}} & \end{aligned} \tag{2.85}$$

for a suitable $\Delta\lambda_{\text{source}}$ which is a typical common period of the oscillating parts of eq. 2.79. The terms 2.82 and 2.83 which consist of sums of complex conjugate addends have zero average contribution to 2.85. In case of a solar cell the term (I) in eq. 2.85 holds the contribution from the first pass through the cell and term (II) holds the contribution from superstrate light

trapping. The latter term is now considered for two separate cases.

In the specific geometry considered here the operator $A_2(\lambda)$ is supposed to represent a transfer matrix system. The operators A_1, A_2 hold the scattering information in terms of Fourier modes. A discrete spectrum as in case of a periodic geometry is assumed. The field quantity $u_1^{(1)}$ holds the Fourier coefficients of the field. In this basis $A_2(\lambda)$ is diagonal as it doesn't correlate different Fourier modes. The operator can be written in the form of a product,

$$A_2(\lambda) = B\Phi(\lambda)\,, \tag{2.86}$$

where B represents the absolute backscattered amplitudes and $\Phi(\lambda)$ the matrix of phase factors. We assume B constant within the integration interval. If further A_1 does not correlate different Fourier modes this operator is also diagonal and exchanges with B and Φ. This is the case if A_1 also represents a 1D structured domain with planes parallel to the superstrate interface. In that case we can write $A_1 = C\Psi$, where C is the matrix of absolute amplitudes and Ψ the matrix of phase factors, and get

$$\frac{1}{\Delta\lambda_{\text{source}}} \int_{\lambda_{\text{source}}-\Delta\lambda_{\text{source}}/2}^{\lambda_{\text{source}}+\Delta\lambda_{\text{source}}/2} I_1^{(n)}(\lambda)d\lambda = \left|u_1^{(1)}\right|^2 + \sum_{k=1}^{n-1} \left|(CB)^k u_1^{(1)}\right|^2 \tag{2.87}$$

which adds up intensities from subsequent iterations and is commonly used for incoherent coupling in 1D systems.

If A_1 is not diagonal, i.e. the operator correlates the different Fourier modes as in case of a 2D or 3D textured scatterer, a wavelength dependent interference pattern will also be created from the superstrate light trapping term in eq. 2.85. Generally all addends in the integrand can be written in the form of a wavelength independent contribution and an interference term. The difference in the matrix elements of the operators is only in phase factors. The incoherent average over a common charactistic wavelength interval of all phase factors decouples the different Fourier modes and allows to incoherently add up the intensities of all Fourier modes within each iteration.

Discussion of the incoherent averaging with respect to the solar cell layout

In case of a solar cell the operators A_1, A_2 are both lossy due to absorption or reflection out of the system. Higher order terms in eq. 2.79 therefore contribute decreasing amounts of energy to the solution. The lowest order coupling terms in eq. 2.79 have phase factors as discussed on eq. 2.73 and should vanish when integrating over the monochromator bandwidth. The second

order term

$$\sum_{k=1}^{n-1} \left|(A_1 A_2(\lambda))^k u_1^{(1)}\right|^2 = \sum_{k=1}^{n-1} \left|(A_1 B \Phi(\lambda))^k u_1^{(1)}\right|^2 \tag{2.88}$$

does have contributions which oscillate at the difference frequency of phase factors. Crucially low difference frequencies can occur between Fourier modes which propagate at low angles to the stack normal. However the loss by transmission through the superstrate / air interface is very high for these modes so that their contribution are not expected to be very important.

Generally the validity of the incoherent coupling described above is dependent on the condition that A_1 and B are independent of the wavelength over the integration range. This assumption can be violated at steep flanks of resonances. In most cases of the light trapping concepts discussed within this thesis resonances are not of a very high quality and do not show steep flanks. In some cases isolated narrow resonances occur, but their contribution to the wavelength integrated cell absorptance, which is the most interesting quantity for photovoltaic application, is low. In case of the back reflection operator B, large changes in narrow wavelength intervals occur in conditions when a Fourier mode is close to the angle of total internal reflection.

For a rigorous simulation of the domain coupling also in critical wavelength ranges the incoherent averaging needs to be carried out explicitly. The computational effort of this is very high as the finite element solution needs to be computed at a large number of wavelength evaluation points.

Details and discussion of the implemented algorithm

The domain coupling is implemented in an iterative way. In each iteration incoherent target quantities like absorption and reflected intensity are calculated and summed up with results from previous iterations. The finite element method is especially suitable for this type of coupling as the LU decomposition of the finite element matrix needs to be calculated only once and can then be used to solve many different source configurations.

It was found that, employing the incoherent coupling as described in eq. 2.85 with completely incoherent Fourier modes, a major bottleneck in simulation consisted in evaluating the post–processing functionals for absorptance calculation. Considering a 3D computational domain of $2\,\mu$m domain width, for example, 45 volume integrals over the computational domain need to be calculated at $\lambda = 800\,$nm to obtain the absorptance matrices required for incoherent coupling. It was therefore decided not to implement the completely incoherent transfer. Instead we decouple incoherently between iterations and not between the Fourier modes within one iteration. This means that, in the form of the incoherent response given in eq. 2.85, the

wavelength integration was not carried out,

$$I_{\text{simulated}}(\lambda) = \left|u_1^{(1)}(\lambda)\right|^2 + \sum_{k=1}^{n-1} \left|(A_1(\lambda)B(\lambda)\Phi(\lambda))^k u_1^{(1)}\right|^2 . \tag{2.89}$$

Due to reflection and absorption losses this form required only a few iteration steps in all cases, usually 3 to 5, for a convergence to an energy error of less than 1%. The required computational costs of this implementation are considerably lower compared to the complete decoupling of the Fourier modes. This kind of superstrate coupling was therefore found suitable for 3D simulation as well. The required post–processing was parallelized in Matlab using the package MatlabMPI[4].

The implemented superstrate coupling is clearly an approximation to the incoherent superstrate response but the simulations presented in this thesis demonstrate that superstrate light trapping effects need to be integrated in solar cell simulation. For computational reasons this could only be done in the presented way. It should further be noted that the wavelength integration of this solution for a fine wavelength sampling should again yield the rigorous result if the separation of scales, which was discussed above, is applicable.

2.2.4. A note on error measurement in the optical simulations

Integral values of absorptance, transmittance and reflectance are the quantities of interest in solar cell simulation. These quantities measure the proportion of the incoming power absorbed, transmitted or reflected on a scale between zero and one. In the convergence studies in this thesis the computational error is measured as the absorptance error within the individual absorbing layers of the solar cell. Usually, relative error measures with respect to an analytic or high quality numerical solution $A_{\text{reference}}$

$$\text{relative absorptance error} := \frac{||A - A_{\text{reference}}||}{||A_{\text{reference}}||} \tag{2.90}$$

are used in numerical analysis. However, the use of a relative error measure can be misleading in the interpretation of absorptance errors. In cases of a low absorption coefficient or very small material volume the relative error can be very high for some material's sub–volume of the computational domain, as an effect of a very small $A_{\text{reference}}$. The global error may instead be very small already.

[4] http://www.ll.mit.edu/mission/isr/matlabmpi/matlabmpi.html

Layer resolved error analysis was used for convergence analysis in this thesis to ensure the validity of the conclusions on different sub–volumina drawn from the simulations. The applied error measure for most simulations is the absolute absorptance scale, i.e. errors are measured as

$$\text{absorptance error} := \|A - A_{\text{reference}}\| \,. \tag{2.91}$$

In many cases the relative error is also presented for reference.

For solar cell efficiency calculation, integral values of the absorptance over the working spectral range of the device are the most important output quantity. Their accurate computation does not require high precision at wavelengths where absorptance is low. Also for experimental comparison a very high spectrally resolved precision is not necessary. Absolute errors of 0.01 on the absorptance scale were used as desired error threshold in most cases.

2.3. Monte Carlo simulation

In Monte Carlo type simulations with random samples the convergence of integral averages is given by the central limit theorem. We consider a random sample of k identically distributed random variates X_i, $i = 1, \ldots, k$ with a common expectation value μ and variance σ^2, which can be assumed in case of a Monte Carlo experiment. The central limit theorem states [Wei11; Gey92] that the variate

$$S_k = \frac{1}{k} \sum_{i=1}^{k} X_i \tag{2.92}$$

approximates the gaussian normal distribution with mean value μ and

$$\sigma_{S_k} = \frac{\sigma}{\sqrt{k}} \,. \tag{2.93}$$

A convergence behaviour of $\frac{1}{\sqrt{k}}$ is therefore expected for the tolerance interval of sample averages in the Monte Carlo experiment. Given a required error tolerance for the result of the experiment an appropriate sample size k can be determined from σ. In this thesis the standard error interval σ_{S_k} of the sample average is estimated by using a finite random set of representations to estimate σ for the whole population.

2.4. Modeling of the device geometry

2.4.1. Characterization and synthesization of random surfaces

The statistical measure predominantly used for rough surface characterization in photovoltaics is the root mean square roughness δ_{rms}, i.e. the standard deviation of the height. Correlations of haze and δ_{rms} as well as between haze and light trapping properties have been shown experimentally within several TCO (transparent conductive oxide) technologies [LGH04; Dau+06]. Daudrix [Dau+06] also investigated whether the correlation between δ_{rms} and haze was given across different TCO technologies and found that this was not the case. The root mean square roughness provides no information about lateral correlation properties of the height data. Other characterization quantities for rough surfaces used in photovoltaic research are the distribution of local angles [Sch09; Agr+10] and the height autocorrelation function (ACF) or power spectral density (PSD) [Dom+10]. In view of random rough surface synthesization the height ACF is particularly easy to handle and therefore was used as the main surface characterization quantity within this thesis.

Surface height distribution and autocorrelation

The height distribution of the rough surfaces considered in this thesis are unimodal distributions around their mean values. In dependence on the manufacturing process, the distributions can be symmetric or have a skewness, as depicted in Fig. 2.9. The skewness can also be seen in the height autocorrelation [Whi97].

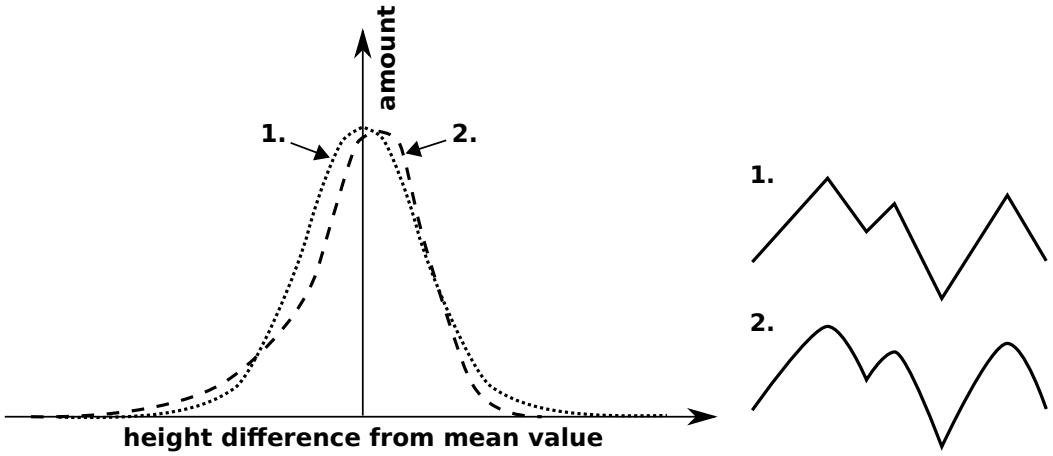

Figure 2.9.: *Schematic of height distributions (left). Skewness of the distribution may be a result of a characteristic manufacturing process (right).*

Height autocorrelation functions provide information about the height correlation of two points as a function of their distance. The 2D spatial autocorrelation function of a real valued signal $f(\mathbf{r})$, $\mathbf{r} \in \mathbb{R}^2$, is defined as

$$\mathrm{ACF}(f;\mathbf{d}) = \int_{\mathbb{R}^2} f(\mathbf{r})\, f(\mathbf{r}+\mathbf{d})\, d^2\mathbf{r} \,\Big/ \sigma^2 \tag{2.94}$$

whith $d \in \mathbb{R}^2$ and the variance σ^2 of f. This definition can be rewritten in Fourier space, provided f has a Fourier representation,

$$\begin{aligned} \mathrm{ACF}(f;\mathbf{d}) &= \int_{\mathbb{R}^2} \hat{f}^*(\mathbf{k})\, \hat{f}(\mathbf{k}) e^{i\mathbf{k}\cdot\mathbf{d}}\, d^2\mathbf{k} \,\Big/ \sigma^2 \\ &= \int_{\mathbb{R}^2} \left(\left|\hat{f}(k)\right|^2 \Big/ \sigma^2 \right) e^{i\mathbf{k}\cdot\mathbf{d}}\, d^2\mathbf{k} \\ &= \int_{\mathbb{R}^2} \mathrm{PSD}(\mathbf{k}) e^{i\mathbf{k}\cdot\mathbf{d}}\, d^2\mathbf{k}\,. \end{aligned} \tag{2.95}$$

where a hat denotes the Fourier transform and an asterisk the complex conjugate. The autocorrelation of a signal is the Fourier transform of the signals power spectral density.

If the signal is periodic or periodified the term *circular ACF* is often used instead of *ACF*. Within this thesis all ACF data is generated as periodic data using the fast Fourier transform and the term circular will not be used as no distinction is necessary. Surface height data is usually provided in the form of AFM scans on a cartesian grid, with extents of $6\,\mu\mathrm{m} \times 6\,\mu\mathrm{m}$ to $18\,\mu\mathrm{m} \times 18\,\mu\mathrm{m}$. From such a data set the circular autocorrelation function can be rapidly calculated using FFT. The determination of the non-periodic autocorrelation function [Wu00] would require more surface data and a longer time for computation.

If the surface texturing does not have a preferential direction the 2D ACF is isotropic and can be represented by a radial ACF. A schematic of a radial ACF with typical characteristics for the surfaces discussed in the chapter about rough surface light trapping is depicted in Fig. 2.10. A few characteristic points have been marked within the drawing:

A The shape of the autocorrelation function in the vicinity of zero determines the sharpness of events [Whi97].

B In the context of spatial autocorrelation data the term *autocorrelation length* often appears as characteristic measure of the width of the distribution. It has, however, no natural definition. Exponential autocorrelation functions are often defined as

$$\mathrm{ACF}(d) = \exp\left[-3\left(\frac{d}{l_{\mathrm{AC}}}\right)^{\nu}\right] \tag{2.96}$$

so that ACF(l_{AC}) = 0.05 [Abr97]. For the simulations within this thesis a gaussian distribution in the common form

$$\mathrm{ACF}(d) = \exp\left[-\frac{1}{2}\left(\frac{d}{\sigma_{AC}}\right)^2\right] \tag{2.97}$$

was chosen. The autocorrelation length was computed from the definition above as

$$l_{AC} = \sqrt{6}\sigma_{AC}\,. \tag{2.98}$$

C Negative values and oscillations of the autocorrelation function can be related to processing or growth characteristics [Whi97].

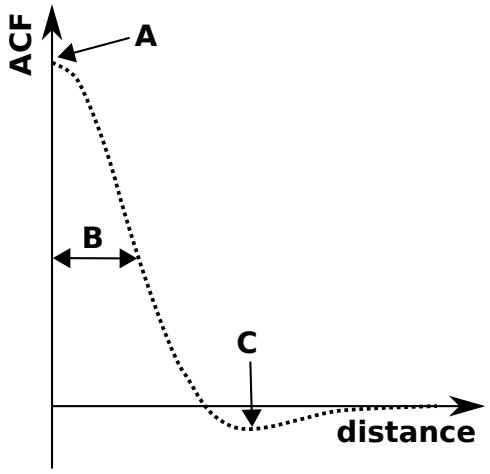

Figure 2.10.: *Schematic of the typical form of a 2D isotropic height autocorrelation function. Characteristic points marked with letters are explained within the text.*

ACF based random surface synthesization

An ACF based random surface synthesization method was implemented relying only on Fourier transform and random phase generation. Using the definition for the PSD given in equation 2.95 a single periodic rough surface representation is computed by applying the inverse Fourier transform on the product of the surface standard deviation σ_{rms}, the square root of the PSD and a sample of random phase factors [Wu00]:

$$Z_{rand}(x,y) = \mathrm{IFFT}\left(\sigma_{rms}\sqrt{\mathrm{PSD}(k_x,k_y)}\;\underbrace{e^{i\phi_{rand}(k_x,k_y)}}_{\text{random phase sample}}\right) \tag{2.99}$$

The only constraint on the choice of phase factors is that the obtained signal needs to be real. For this reason phase factors can not be chosen completely at random but have to be symmetric when taking the complex conjugate and point inverting at the origin.

The synthesization procedure from height ACF data described by equation 2.99 effectively assumes that phases in Fourier space are completely uncorrelated. If the characteristic fingerprints of the manufacturing process of an experimental surface are strong it is unlikely that phases are completely uncorrelated and a random choice of phases might not produce the desired result.

Surface angle distribution

Due to the loss of phase correlation the height ACF does not provide knowledge about the local angle distribution on the original surface with respect to a reference direction. Agrawal recently suggested to use both the height distribution and the local angle distribution as describing distributions for rough surfaces in photovoltaics [Agr+10]. Within this thesis the local angle distribution is used as additional quantity to characterize synthesized surfaces.

The local local angle with respect to a reference direction can be calculated from the local normal vector as follows. For a scalar field $F(x, y, z)$ in three space dimensions, the gradient points in the direction of the greatest increase of the field. Given a height distribution in the form

$$z = f(x, y) \tag{2.100}$$

the implicit function

$$F_{\pm}(x, y, z) = \pm(z - f(x, y)) \tag{2.101}$$

can be defined which is zero on every point on the surface and nonzero in its vicinity. The local normal vector of the surface can thus be computed as

$$n(x, y) = \frac{\nabla F_{\pm}(x, y, z)}{||\nabla F_{\pm}(x, y, z)||} \,. \tag{2.102}$$

The surface angle to the reference direction z is then given by

$$\theta(x, y) = \arccos\left(\frac{\mathbf{z} \cdot \nabla F_{\pm}(x, y, z)}{||\nabla F_{\pm}(x, y, z)||}\right) . \tag{2.103}$$

Within this thesis the sign of $F_{\pm}(x, y, z)$ is chosen such that $\mathbf{z} \cdot \mathbf{n}(x, y)$ is one if the surface is locally parallel to the xy–plane.

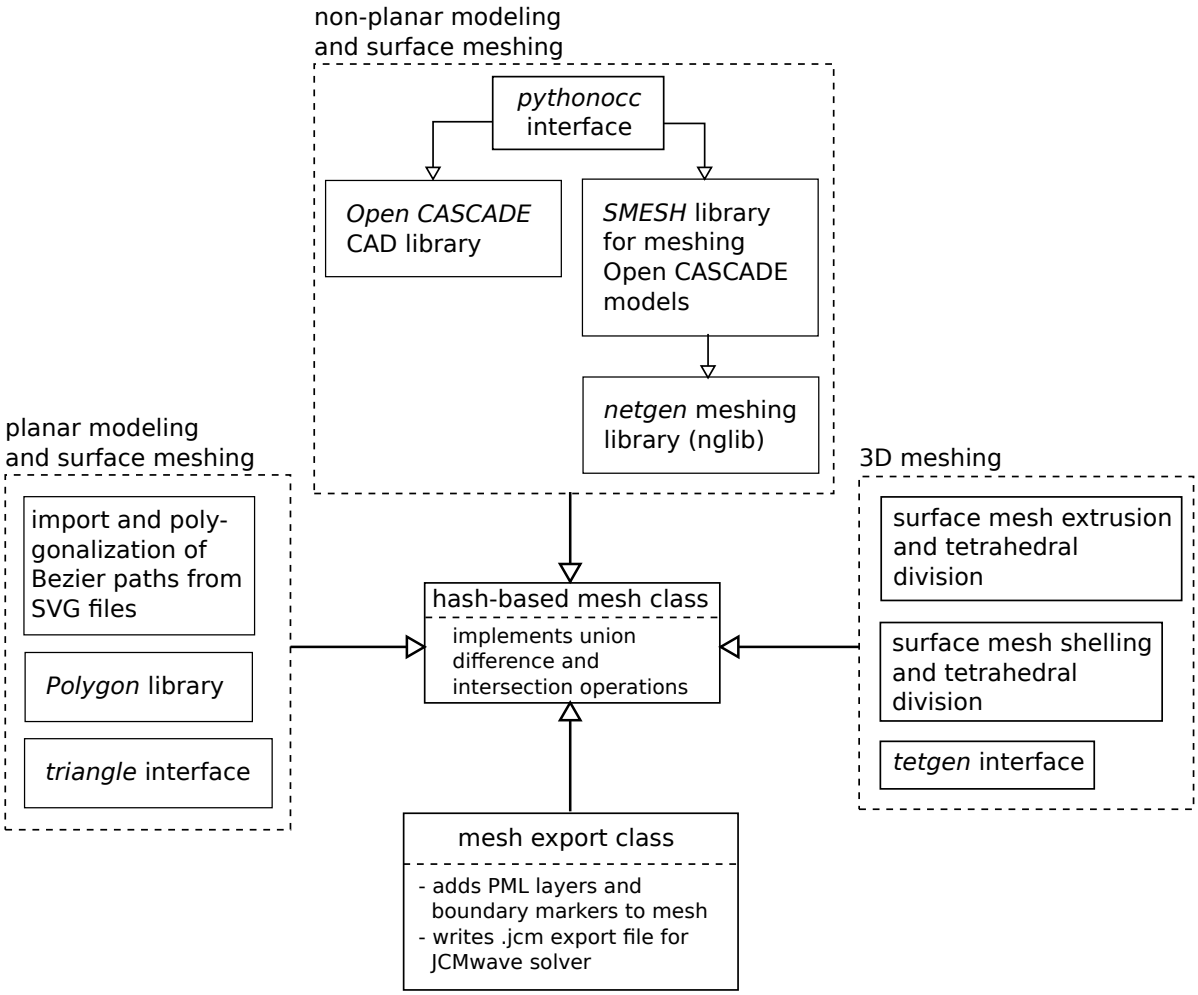

Figure 2.11.: *Main elements of the python based geometric modeling and grid generation toolbox. Public domain sofware included in the toolbox is marked by italic letters.*

2.4.2. 3D CAD modeling and unstructured grid creation

In contrast to 2D where a geometrical description for a space resolved simulation can usually be easily found on the basis of a polygonalization of objects the representation of 3D objects and an efficient grid generation based on this description is far more complicated. This section describes the grid generation toolbox used for the 3D simulations of solar cells with rough surfaces in section 3.5 and the simulations of periodic textures in chapters 4 and 5.

The grid generator implementation was especially targeted towards periodic mesh generation for layered media stacks with arbitrary interface texture. A divide–and–conquer strategy was employed to build a robust mesher. A stack of layers is defined in a first step. Each layer is then meshed separately with an appropriate algorithm. Shared interfaces are propagated from

meshed layers to adjacent unmeshed layers. In rare cases of matching errors at the shared boundaries due to point insertion during volume meshing the errors are fixed and the layers are remeshed if necessary. Specific implementations were done for layers with inclusions and very thin layers which commonly lead to very poor grids when a 3D grid generator like *tetgen* or *netgen* is naively used. The periodic boundaries required by the finite element solver are enforced by boundary mesh projection from a primary boundary face to its opponent secondary face.

The scripting language "python" was used for implementation. The package makes extensive use of other public domain packages for geometric modeling and meshing. Its main components are depicted schematically in Fig. 2.11:

- A hash–based grid implementation serves as an interface between the different grid generators. It stores geometrical elements according to a hash value computed from their point coordinates. The hash value is obtained from a string representation of the coordinates with a user–defined precision of the representation. Hashing errors can possibly occur due to known problems of floating point representation when using this hashing algorithm. No errors were detected during use so far. The grid representation implements union, difference and intersection operations. Each mesh element can be assigned with arbitrary data attributes, e.g. material data.

- The pythonOCC [Pyt] interface to the *Open CASCADE* [OCS01] package and the Netgen [Sch97] package was used for geometrical representation and meshing of curved 3D surfaces.

- For creation of complex 2D models with curved interfaces and tracing of curves in images a SVG parser was implemented. The parser reads control points of Bézier paths from the SVG which are transformed into an internal Bézier representation which uses an implementation of de Casteljau's algorithm. The bezier representation is polygonalized using a segment length constraint for further use. This implementation was used for reconstruction of the unit cell of a periodic texture from TEM data in section 4.2.2.

- The *Polygon* python interface to the polygon clipping library *gpc*[5] was used for set operations on polygons in 2D.

- The 2D grid generator Triangle [She96] was used for meshing of all planar surfaces.

[5] `http://www.cs.man.ac.uk/~toby/alan/software/`

- Tetgen [Si09] was used for tetrahedral volume meshing of all volumes except for thin layers.
- Thin layers were volume–meshed using a custom implementation which employs a simple extrusion algorithm and subsequent tetrahedralization. Two different cases of extrusion were implemented:
  - Vertical extrusion in $\pm z$–direction.
  - Shelling of a surface in the direction of the surface normal to ensure a constant normal thickness of a curved layer. Boundary points of the domain are vertically shifted in this algorithm. Depending on the parent grid this algorithm can fail as surface triangles may collapse or generated tetrahedrons may intersect with each other.
- A mesh export interface into the *JCMwave* mesh format adds PML boundary layers and periodic or domain boundary markers before exporting the mesh.

3. Random surfaces for light management in thin film silicon solar cells

This chapter presents optical simulations of crystalline thin film silicon solar cells with rough interface textures. The key contribution of this thesis on simulation of solar cells with statistically rough interfaces lies in the characterization of the simulation itself. In contrast to many of the commonly used simulation approaches a rigorous solution of Maxwell's equations on space discretized simulation domains is employed. Rigorous modeling of layered systems with rough interfaces has become increasingly popular only during the last few years. Despite of the use of a discretized geometry and rigorous simulation a few model error sources need to be considered. To establish a clear identification of model error sources we generated and applied synthesized rough surface data.

The analyzed model error are introduced in section 3.3.2. A detailed error analysis on simulation of 1D rough surface slices can be found in sections 3.4.1 and 3.4.2. A characterization of the same errors for simulation of 2D rough surfaces can be found in section 3.5.1. In section 3.5.2 the results of the simulation of solar cells with 2D rough surfaces and of identical cells with 1D rough surface slices are compared. Further a comparative study was done between rigorous simulation and the implementation of an approximate solver based on statistical scattering and 1D simulation. The results of this study are presented in section 3.6.

3.1. Introduction

3.1.1. Prior work

The Yablonovitch limit

Rough surfaces have been playing a major role in the light management of light absorbing and emitting semiconductor devices for a few decades already. Attention was drawn to them

through the predicition of theoretical limits, initiated by the work of Yablonovitch on statistical ray optics [Yab82]. In his initial paper he used the argument that for a material volume bounded by randomizing surfaces in one direction a perfect directional randomization of the radiation inside the volume could be achieved, provided the escape probability was low enough. Yablonovitch stated that if that condition holds a few total internal reflections would be sufficient to completely randomize the field. A small escape cone can be realized by high refractive index materials like silicon. Using the assumption of complete randomization Yablonovitch predicted an absorption enhancement of $4n^2$ for bulk absorption, where n is the real part of the refractive index. The limit is valid only under conditions of weak absorption as e.g. close to the indirect band edge of silicon. Yablonovitch achieved a good comparability between his predictions and the measured reflection from a $250\,\mu$m thick crystalline silicon wafer with rough surfaces. Deckman provided further experimental results for $0.85\,\mu$m thick amorphous silicon layers [DRY83], i.e. in the thin film regime. He measured an absorption enhancement of only $2n^2$ which he claimed being due to the lack of a rear reflector. On the basis of Yablonovitch's theory Tiedje [Tie+84] derived more detailed limit predictions for the limiting efficiency of silicon based solar cells, taking into account radiative recombination, Auger recombination and free carrier absorption as loss mechanisms. He estimated a limit efficiency of almost 30% for a $100\,\mu$m thick crystalline silicon cell with light trapping at Yablonovitch's limit and under AM1.5g illumination. Tiedje indicated that limit is close to the ideal radiative recombination limit 32.9% of a solar cell with unit absorption at energies above the indirect band edge.

Yablonovitch's theory is a good approximation if the scattering angle upon entry into the solar cell and subsequent reflection angles are not strongly correlated. Due to ratios of texture feature size and layer thickness of $\simeq 1$ this is hard to achieve in thin film solar cells. In many fabrication processes the scattering texture is furthermore replicated from the substrate to all other interfaces during the deposition process. Thus a fairly small distribution of reflection angles can be available for an initially scattered beam. It can be doubted that the limit derived by Yablonovitch [Yab82] under specific assumptions on scattering statistics and in a pure ray tracing picture holds under these circumstances. Furthermore the estimates obtained in [Yab82; Tie+84] treat a single finite material layer and assume the incoming and outgoing flux probabilities through its interfaces to be known. In more complicated setups composed of a few finite layers, as found in every solar cell, these quantities are usually not straightforward to obtain. Also the layered system can in general not be decoupled any more between the different layers which renders analytic approaches difficult.

Computer simulation

To provide reliable estimations of the absorptance of complete cell designs at low computational effort, approximate solvers for multilayer geometries with scattering rough interfaces have been developed in the past decade and were successfully applied to solar cell simulation [LPS94; KST02; KST03; Krč+03; Krč+04; SPV04; Lan+11]. They combine coherent transfer matrix algorithms for flat multilayer stacks and incoherent ray tracing methodswhich apply a scattering transfer function at every rough interface. During simulation the incoming power flux is empirically divided into two components, a direct coherent and a scattered incoherent component. The two components are then simulated separately and finally summed up to obtain the partial coherent response of the system. For the scattering behaviour at rough interfaces angular light distributions in the far field are assumed to be valid independent of the layer thickness. For a long time the availability of far field scattering data between all material pairs in the device has been an issue in the use of these methods, as measurements can usually only be performed in air. But recently scattering integral based methods have been developed to directly obtain ARS data from measurements of the surface morphology between arbitrary material pairs, satisfactorily resolving this issue [JZ09; Dom+10; Jäg+11]. Experimental comparisons such as in [Jäg+11] often show a good comparability to the approximate solutions but to the knowledge of the author of this thesis no detailed analysis of possible error sources has been reported yet.

Rigorous Maxwell solvers

The use of rigorous solvers for Maxwell's equations for optical simulation of solar cells with rough textures is not as widely spread as the use of approximate solvers. Simulations of complete solar cells with 2D rough textures have been reported by a few groups only. Publications are known to the author from Fahr and Rockstuhl [Bit+08; FRL08], Jandl [Jan+10; Jan+11], Agrawal [Agr+10; AF11] and Lacombe [Lac+11]. In surface scattering simulation for radar sensing applications a similar methodology has been very well developed and characterized [DB07; HSB95; MLS09; PY04; Sim04; SML09; WC01; ZK00; Bra+00]. For simulation a Monte Carlo sampling of rough surface patches of finite extent is usually performed to obtain statistically averaged target quantities. Isolated geometries combined with localized incoming fields are preferred to periodic geometries to avoid simulation artifacts due to the periodification. For solar cell simulation a laterally periodic setting with a simple incoming plane wave is preferential for the interpretation of the various energy fluxes inside the multilayer cell structure. This is the configuration used by the author and the other groups referenced

above.

3.1.2. Challenges and contribution of this thesis

The main challenge in rigorous simulation of solar cells with rough interfaces is certainly the representation of an extended scatterer. At wavelengths above 900 nm, where absorption coefficients are small and light trapping by the textured surfaces is most important, light can propagate many micrometers within the layers of the solar cell without substantial damping, as illustrated in Fig. 2.4. Rigorous simulation of domains with such a geometric extent is, at least in 3D, not possible with current computational resources. Therefore a Monte Carlo sampling of small surface patches is usually employed. A lateral boundary condition needs to be chosen for these surface patches which is artificial with respect to the experimental conditions. An error may be induced in the simulation result by this choice and the Monte Carlo sampling may not converge to the same average as found under experimental conditions. The problem of unknown lateral optical correlation lengths and domain size effects in rigorous solar cell simulation was briefly discussed by the author of this thesis [Loc+11] and also recently by Agrawal [AF11] but no consequent analysis of this error source has been published yet. Also, no results on the typical convergence of the Monte Carlo sampling in these kind of simulations of solar cells have been published yet.

The work on optical simulation of solar cells with rough interfaces presented in this thesis is a fundamental characterization necessary for any kind of reliable predictive simulations in such complex optical systems. The main points adressed in this work are surface modeling, characterization of optical simulations and evaluation of an approximate solver:

- Any kind of texture optimization by simulation requires a geometric modeling. In section 3.2 the performane of a height autocorrelation function based surface sythesization algorithm for rough surface modeling was characterized with respect to two different experimental TCO roughness types. Modeling surface roughness can be preferential when working with small lateral computational domain sizes. In this thesis the characterized synthesization was used as a basis for the characterization of the optical simulations.

- The multilayer geometry of solar cells, material properties and the requirements on output data make it necessary to fully characterize the simulation algorithm before using it to make any predictions. For this reason an extensive numerical characterization was done as part of this thesis for 1D and 2D rough surfaces in solar cells. The characterization for 1D rough surfaces is presented in sections 3.4.1 and 3.4.2 and for 2D rough surfaces in section 3.5.1.

- The results of 1D and 2D rough surfaces based on identical cell structures and interface height distributions are compared in section 3.5.2.
- Most optical simulation of solar cells with rough interfaces textures is still done using approximate methods. Using the characterized rigorous simulation a direct comparison between rigorous simulation and a scattering based simulator was performed to obtain error estimates for an approximate 1D solver and a critical geometry. The results of this analysis are presented in section 3.6.

3.2. Random surface synthesization

Random surface modeling is generally necessary whenever no measurement data is available. This may be the case in optimizations of the surface morphology, e.g. with respect to light trapping properties. Rough surface models have already been employed for light trapping optimization by Fahr and Rockstuhl [FRL08; Roc+10]. In this thesis, synthesized rough surface data was applied for a different reason, namely to obtain a clear separation of the different error sources which influence the simulation result. The requirement for using synthesized data results from the simulation strategy of computing the average of a sample of small surface representations instead of one large representation (cf. sections 2.3, 3.4.1) and the choice of lateral boundary conditions which comes along with this. The implemented surface synthesization, according to eq. 2.99, removes an error source which is present when relying on experimental data, thus allowing an unbiased characterization of the remaining error sources of the simulation, which is the main focus of this chapter. This rationale for the choice of synthetic surface data is detailed in the following:
In the implementation of the optical scattering problem of thin film solar cells with rough interfaces, it is preferential to apply periodic boundary conditions at the sides of the computational domain for different reasons, described in sections 2.2.3 and 3.4.2. When using experimental data for simulation, the data window can simply be set periodic or the periodification can be realized using a mirroring technique. These two cases are depicted schematically in Fig. 3.1. Both methods lead to the creation of geometric features that are not present on the original experimental surface. In case of the simple periodification of the data window rims with vertical jumps of the surface data are created at the domain boundaries. In case of the mirroring method, ridges are usually created at the domain boundaries. These geometrical features can be a source of artifacts in the optical simulation, especially at metal interfaces where plasmonic effects can lead to strong field localizations. The artifacts induced by rims or rigdes at

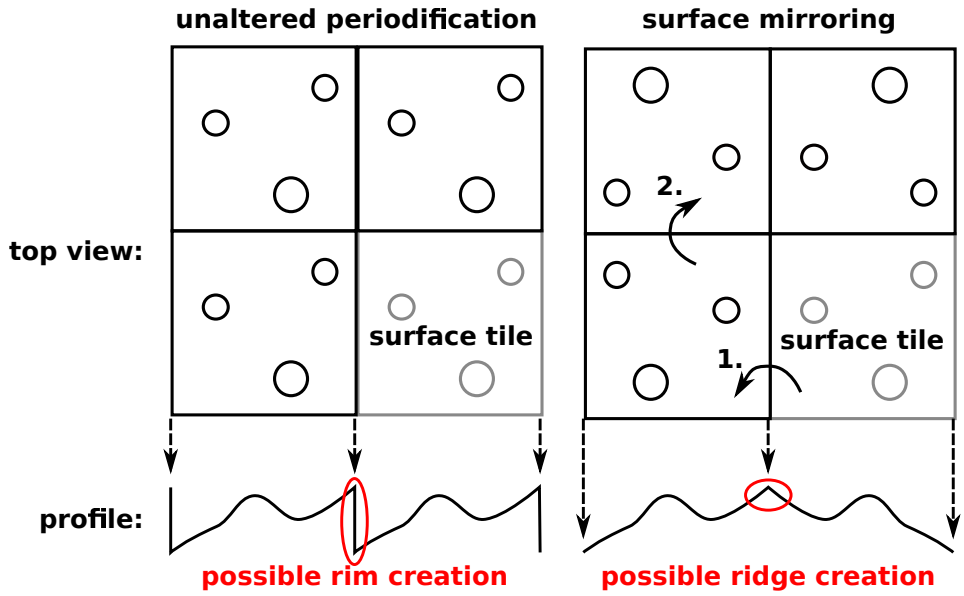

Figure 3.1.: *Schematical representation of trivial surface periodification and periodification by mirroring of the height data. Problems that can occur at the domain boundaries are highlighted by sample profile lines.*

the domain boundaries are not clearly separable as an error source from the error induced by the limited domain size and the periodification. For an analysis of the model error induced by limited domain size and periodic boundaries it is therefore preferential to rely on periodic surface data which is automatically smooth across the periodic boundary.

In practice the magnitude of the errors induced by rims or rigdes at the domain boundaries may actually be small enough to allow good comparability to the experimental case. This mirroring method has recently been used by Jandl for 3D simulation of solar cells from experimental data [Jan+10; Jan+11].

Surface synthesization was performed from height autocorrelation data using the FFT based algorithm described in section 2.4.1. In view of a possible use for morphology optimization in the future, the synthesization procedure was tested on two different typical TCO morphologies:

FTO Fluorine doped tin oxide (SnO_2:F) substrates with rough surface morphologies have already been an industry standard rough TCO for the deposition of thin film solar cells for quite some time [Ben+99]. A commercially available textured TCO sample was used for the characterization. The AFM data was provided by by Schott.

AZO Aluminum doped zinc oxide (ZnO:Al) substrates combine good transparency in the visible range with a low sheet resistance [CT10]. Dependent on the choice of the deposition process and post–deposition etching a large variety of random surface morpholo-

gies can be created [Dau+06]. The requirement for rapid deposition on large areas in PV device production brought sputtered ZnO:Al substrates into the focus of research during the last decade. A distribution of crater–like conical textures can be created from these substrates when post–processed by chemical etching. Size and shape distribution of the texture can be tailored by adjusting deposition and etching parameters [Klu+04; Ber+07a]. The surface sample used for characterization below was provided by Forschungszentrum Jülich and was fabricated as described by Kluth [Klu+04].

The chosen FFT based surface modeling algorithm yielded good results in case of the FTO surface type. The central results of this characterization of the surface synthesization, which were used for the further analysis presented in this chapter, are summarized in Fig. 3.5, Fig. 3.6 and Fig. 3.7.

3.2.1. Preprocessing and periodification of surface data

AFM images taken from surface morphologies are not naturally periodic. Steps or ridges across the boundaries of the surface can lead to artifacts in the fourier transform used to obtain the autocorrelation function. To prevent such effects the AFM data was preprocessed using the following steps:

Background subtraction A linear background is computed and subtracted for AFM image correction. The surface is readjusted to zero mean value after the periodification step.

Best periodic window detection Within a buffer zone along the boundary of the AFM image a data window is searched with a best fit of height and slope across the boundaries in x– and y–direction. A search buffer width of 0.1 times the AFM image width was allowed for this at each boundary.

Periodification A periodification buffer is then defined along the boundary of the obtained data window. Within this zone, height data is periodified across the boundary in both x– and y–direction to obtain a periodic and mostly ridge–free domain. For periodification, the unperiodified data of one boundary is mapped accross the boundary to the other side, weighted by $0.5(1 + cos(d/d_{max}\pi))$, where d is the distance to the boundary and d_{max} the buffer width. A small buffer width of 0.03 of the data window defined in the previous step was chosen for this data periodification.

A sample periodification process of an etched AZO surface together with statistical height and angle data is shown in Fig. 3.2. Both the height distribution and the angle distribution are only

weakly affected by the smoothing procedure. The performance of this periodification process with respect to errors in the height and angle distributions is better for FTO surfaces than for the AZO surface presented here.

Comment on the resolution of used AFM images

AFM data is subject to error sources which limit the resolution of the actual samples surface morphology. First, equally spaced discrete sampling points limit the the lateral resolution of surface morphology. The evaluation point spacing in the AFM images applied here were 35 nm and 39 nm in both directions of a cartesian grid. The studied FTO surfaces, cf. the following section, have the smallest studied feature size with about 290 nm autocorrelation length, measured according to the definition in eq. 2.98. The lateral resolution of the AFM images is therefore considered as sufficient.

The second error source AFM data is subject to is finite tip size. Instead of the surface morphology, which would be mapped using a point-sized tip, the measurement data is always a convolution of the surface morphology with the AFM tip shape. This error source was not considered for the work presented in the following.

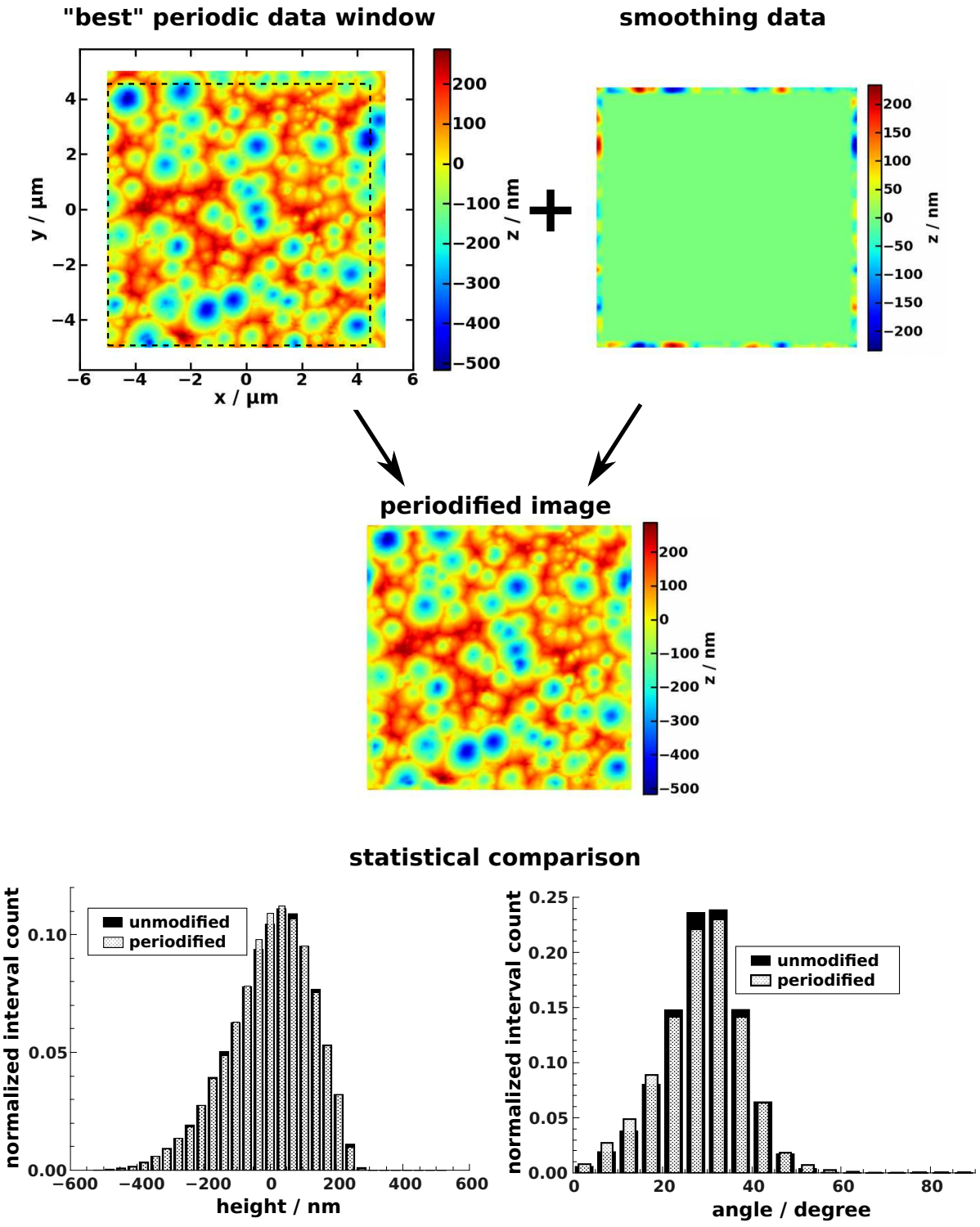

Figure 3.2.: *Sample periodification of an etched ZnO:Al AFM image provided by Forschungszentrum Jülich as described in section 3.2.1. A least error data window is chosen and smoothed across its boundaries. Height and angle (cf. eq. 2.103) distributions before and after the periodification are shown for comparison.*

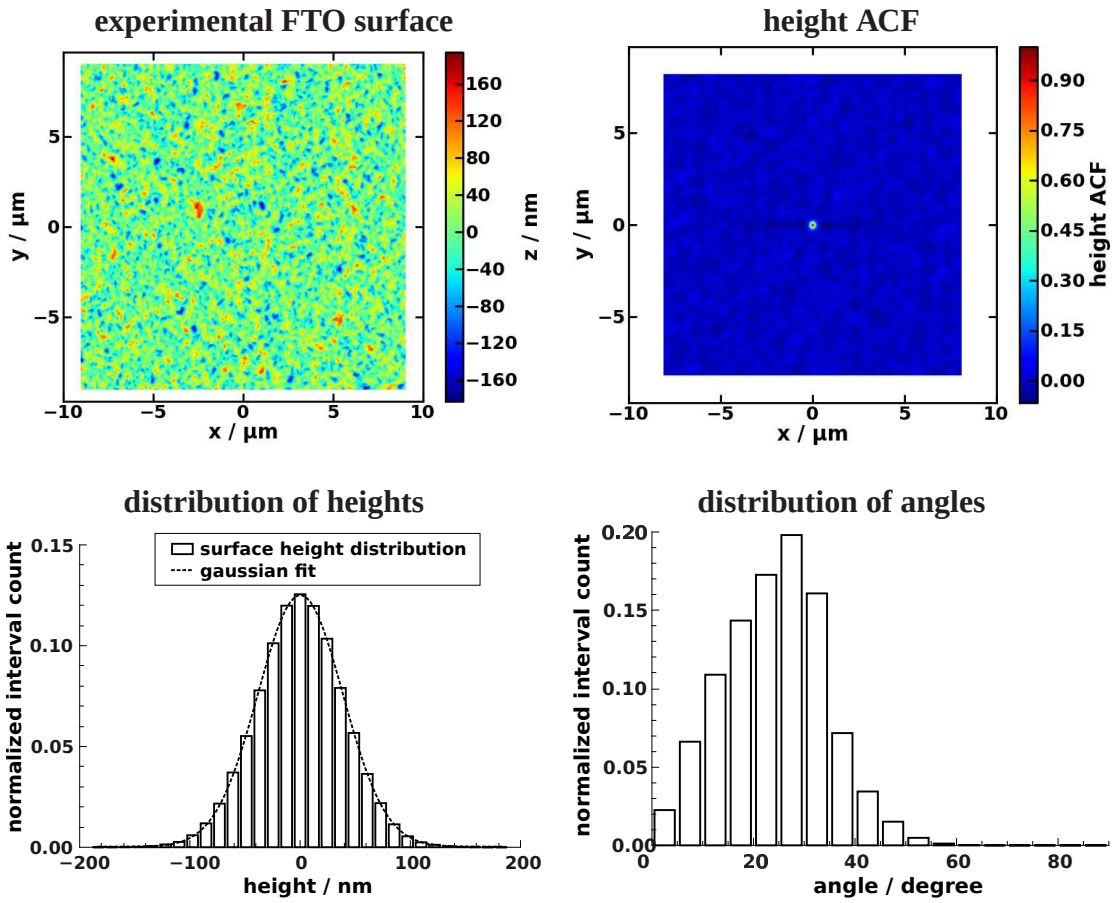

Figure 3.3.: *False color image of AFM data taken from a rough FTO substrate provided by Schott (upper left). The original data was periodified for ACF generation as described in section 3.2.1. The ACF of the image, defined by eq. 2.95, is depicted to the top right. Height and angle (cf. eq. 2.103) distribution of the surface are shown in the second row.*

3.2.2. Characterization and ACF–based modeling of commercially available FTO substrates

Characterization

An $18 \times 18\,\mu$m AFM scan, with 35 nm data point spacing, of a FTO surface taken at Schott Solar is depicted in Fig. 3.3, upper left. In contrast to the etched ZnO:Al surface depicted along with the description of the periodification process above (p. 63) the FTO surface shows no characteristic elemental pattern. The height autocorrelation function depicted to the right of the surface is dominated by a sharp isotropic peak around the origin. Two grooves along the x–axis with sub–zero autocorrelation value can be seen to both sides of the central peak. These features outside the central peak are of a much lower amplitude than the central region.

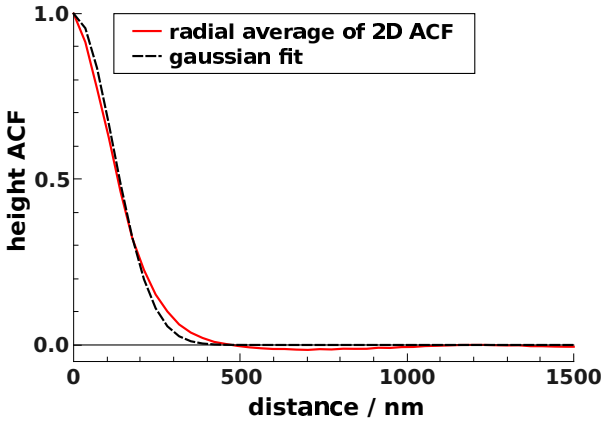

Figure 3.4.: *Radially averaged 2D ACF, computed according to eq. 2.95, with gaussian fit (cf. eq. 2.97) for the FTO surface depicted in Fig. 3.3.*

The height distribution of the surface is very symmetric and has gaussian shape to a high precision, with an rms error of the gaussian fit of only $7 \cdot 10^{-4}$. The local angle distribution has an average around 24°and is slightly asymmetric with a steep descent to the higher values above 35°. This effect is not caused by the data binning. Binning has been kept consistent throughout all height and angle histograms in this section to assure a good comparability. 5° steps from 0° to 90° where chosen for angle histograms and 30 bins in the range from -200 nm to 200 nm for height binning.

The autocorrelation length of about 0.29 μm given in table 3.1 was calculated from a fit of a gaussian model (eq. 2.97) to the radially averaged ACF. The fit is shown together with the radial ACF in Fig. 3.4. The dominating part of the ACF is not exactly of gaussian shape. Abrahamsen [Abr97] suggests to model the radial ACF by the more general exponential function in eq. 2.96 or by choosing a a Bessel or damped cosine function for integration of the negative part of the ACF. But this was not done in this work.

Synthesization of 2D surfaces

Synthetic surfaces were generated in the size of the periodified AFM scan both from the original 2D autocorrelation function and the gaussian model. For visual comparison the periodified

quantity	value
l_{AC} (as def. in eq. 2.98)	0.29 μm
rms roughness	39 nm
angle to global surface normal	mean: 24°, std. dev.: 10°

Table 3.1.: *Numbers for statistical quantification of the FTO surface shown in Fig. 3.3.*

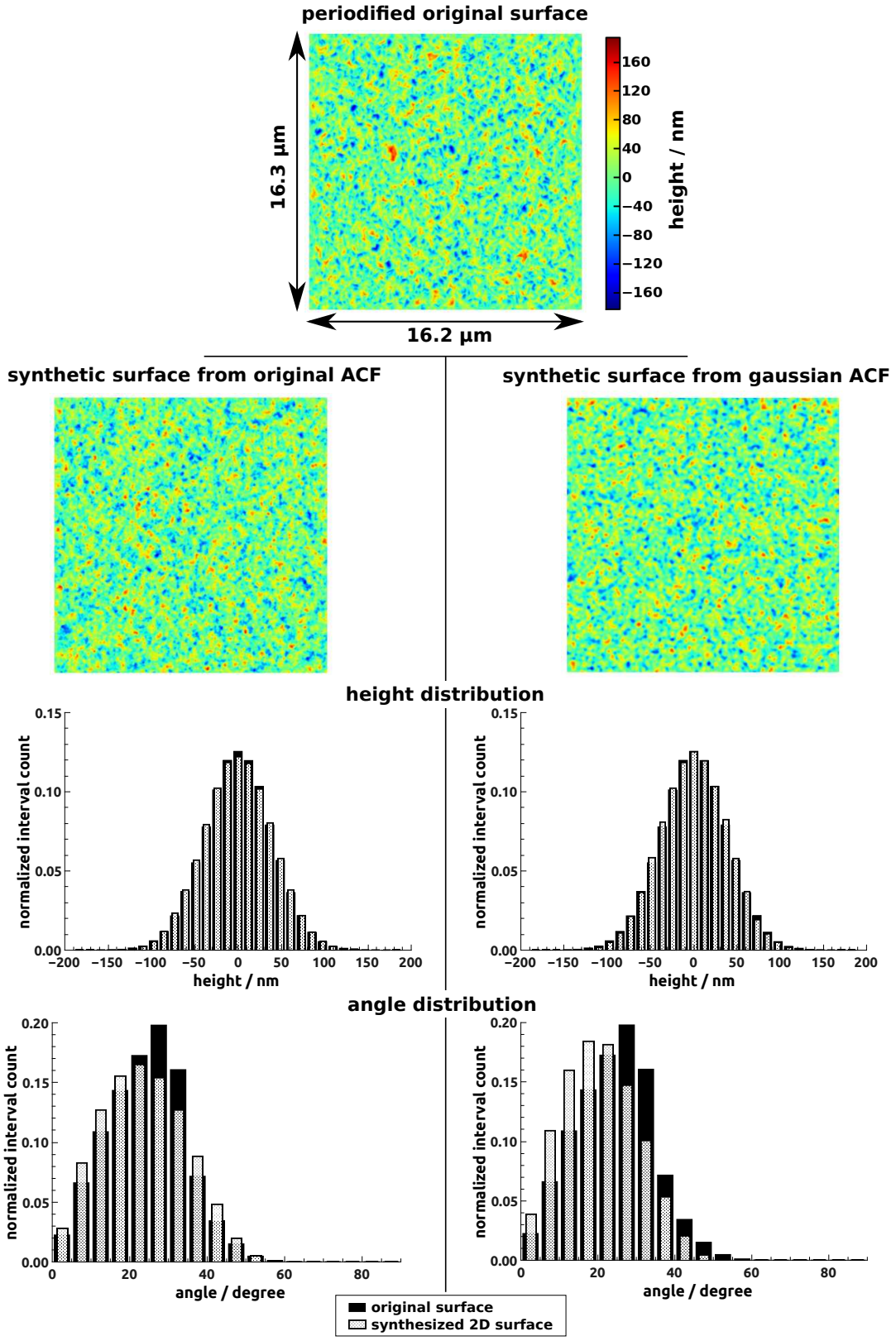

Figure 3.5.: ***Top:*** *FTO surface, periodified as described in sec. 3.2.1.* ***Left column:*** *Synthesized surface generated from the autocorrelation function (cf. eq. 2.95) of the surface depicted in the center of the top row according to eq. 2.99. The corresponding height and angle (cf. eq. 2.103) distributions are shown in the third and fourth row.* ***Right column:*** *Identical plots as in the left column, generated from the gaussian fit to the autocorrelation function of the surface in the top row, depicted in Fig. 3.4.*

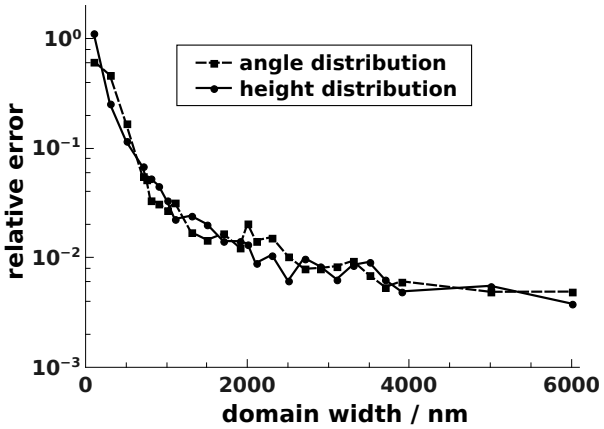

Figure 3.6.: *Relative error of angle (cf. eq. 2.103) and height distribution of small synthesized 2D square surfaces with respect to a 20 µm large square surface. Distributions were averaged over at least 100 representations at every domain width.*

original surface was plotted along with the synthesized surfaces and the corresponding height and angle distributions in Fig. 3.5. Noticeable differences in the false color images are a higher quantity of ridge–like interconnections in the original data compared to the data synthesized from its autocorrelation function and less high–frequency components in the data synthesized from the gaussian autocorrelation function. From the comparison of the two isotropic ACFs in Fig. 3.4 it may be assumed that this lack was caused by the overestimation of the autocorrelation value for small distances in case of the gaussian shape. The height distributions of the original data and of the synthesized datasets compared here show no pronounced differences. The distribution of local angles obtained from the image synthesized using the original ACF is broadened with respect to the original distribution. Its maximum position is shifted by about -5° but the mean surface angle by only $\approx -0.5^\circ$. In case of the synthesization from the gaussian autocorrelation function the maximum position is shifted by $\approx -7.5^\circ$ and the mean surface angle by $\approx -4^\circ$. These shifts were checked with a finer binning and are not due to the choice of the binning.

While the local angle distribution deviates stronger from the experimental surface characteristics when using the gaussian ACF than with the original ACF, the fast descent of this function is beneficial when working with very small surface tiles. As the ACF is defined in real space, a change in domain width directly affects the data window width of the ACF. In the 3D simulations in section 3.5 only small computational domain widths of only a few autocorrelation lengths could be used. For a comparison of simulations with different domain sizes a comparability of the morphology of the rough surfaces needs to be ensured. For the gaussian ACF the relative error of height and angle distributions of synthesized surfaces at various

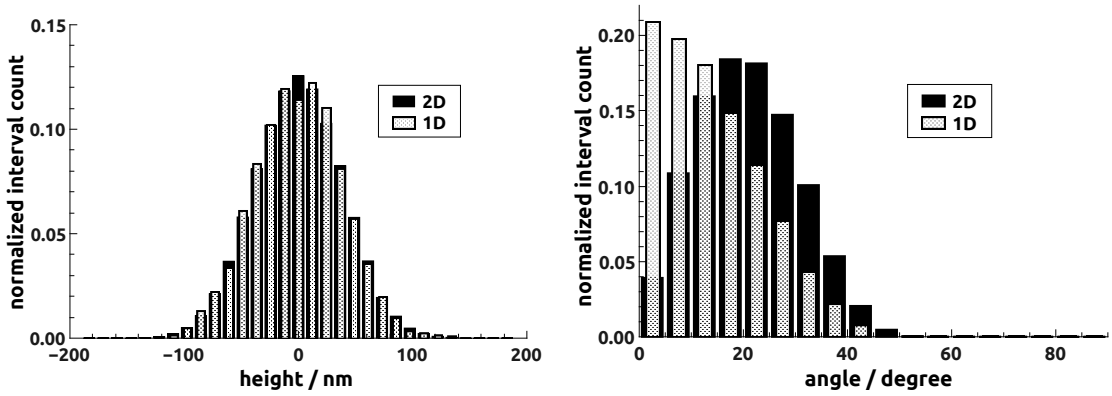

Figure 3.7.: *Comparison of height and angle (cf. eq. 2.103) distributions on 2D and 1D surfaces synthesized from the same gaussian ACF according to eq. 2.99.*

domain widths was therefore tested against the distributions of a synthesized $20\,\mu\text{m} \times 20\,\mu\text{m}$ large surface. A sample of at least 100 surface representations was taken at every domain width to obtain average distributions. The results are depicted in Fig. 3.6. The errors decrease rapidly to $< 10\%$ at a periodicity of twice the autocorrelation length. At this domain width the effective separation of two points is maximally only one autocorrelation length, due to the periodicity of the surfaces. Following this rapid convergence, angle and height distribtutions show a saturation behaviour at relative errors of about 0.5%. The saturation may be induced by round–off errors, insufficient sampling or sampling differences at different domain widths but was not studied any further.

The actual domain widths used for 3D simulation were compared among each other in more detail. The results of this comparison can be found in section 3.5.1.

Synthesization of 1D surfaces

The major part of the characterization of optical simulations in this chapter is based on the simulation of solar cells with 1D rough surfaces. These surfaces were generated from the same autocorrelation function as the 2D surfaces and have the same statistics as 1D cuts from 2D surfaces. Differences between the angle and height distribution between the 2D and 1D surfaces are shown in Fig. 3.7. The height distribution does not change significantly while the local angle distribution does not compare well between 1D and 2D surfaces. The amount of surface parts which are close to horizontally oriented is dominant in case of the 1D surface and not very large in case of the 2D surface. This difference in the angle distribution results from the dependence of the two lateral space dimensions in view of the local surface angle.

Resulting differences in light trapping between 1D and 2D rough surfaces are highlighted in

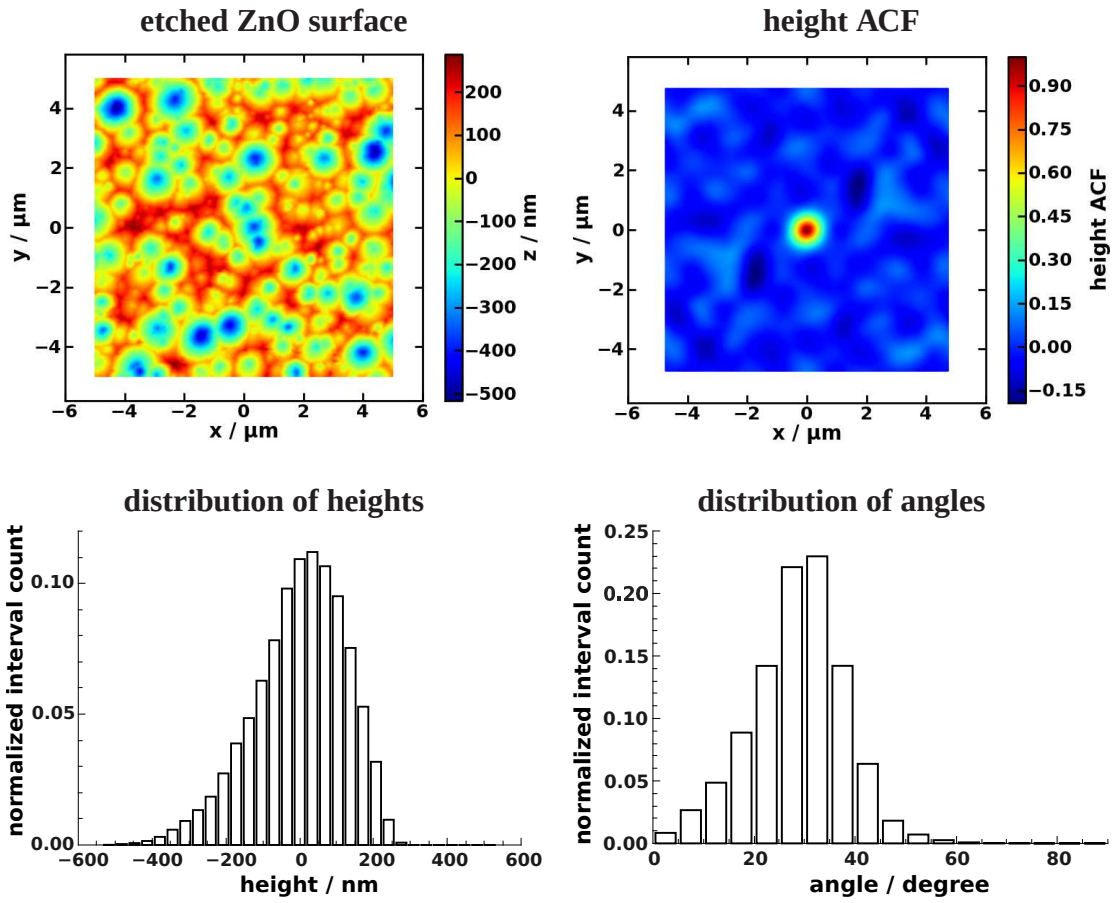

Figure 3.8.: *False color image of AFM data from an etched ZnO:Al surface produced at Forschungszentrum Jülich (upper left). The original data has been periodified for ACF generation as described in section 3.2.1. Height and angle (cf. eq. 2.103) distribution of the surface are shown in the second row.*

a comparison of the simulation results of identical solar cells with 1D and 2D rough surfaces created from the same ACF in section 3.5.2.

3.2.3. Characterization and ACF–based modeling of etched ZnO:Al substrates

Characterization

A sample ZnO:Al surface measured by AFM, with a data point spacing of 39 nm, is depicted in Fig. 3.8 together with its height ACF and its height and angle distributions as characterizing statistical distributions. Characteristic numbers of the surface are provided in table 3.2.

The HCL etching process predominantly created features of a very characteristic elemental

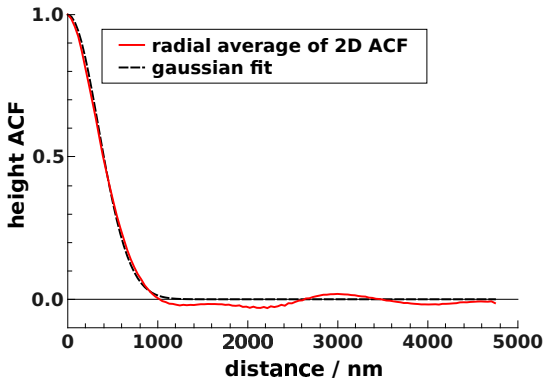

Figure 3.9.: *Radially averaged 2D ACF of the ZnO:Al surface depicted in Fig. 3.8, computed according to eq. 2.95, and gaussian fit (cf. eq. 2.97).*

shape on the ZnO:Al surface depicted in Fig. 3.8, upper left. Isolated conical craters were etched into the surface with a very well defined opening angle of about 120°.

The dominating part of the ACF of the surface depicted in Fig. 3.8, upper right, lies at distances below about 1 μm from the origin. This part is approximately isotropic and of a bell shape. The autocorrelation value drops to ≤ 0 at about 1 μm distance. Distinct features are visible in the lower left and mirrored in the upper right quarter, where the autocorrelation value drops to < -0.15. These features might be due to the two areas in the AFM image where almost no large cones appear and which lie along the appropriate space direction. A radial averaged ACF was computed and fitted with a gaussian model. Both the radial ACF and fit result are depicted in Fig. 3.9. The gaussian fit models the autocorrelation function very well up to a radius of about 1 μm. An autocorrelation length of about 0.83 μm was derived from the fit according to eq. 2.98.

The height distribution of the surface is not symmetric. This is not very surprising as also the height distribution of a cone is not symmetric. The distribution of angles on the surface

quantity	value
l_{AC} (as def. in eq. 2.98)	0.83 μm
rms roughness	126 nm
angle to global surface normal	mean: 29°, std. dev.: 10°
cone opening angle	mean: 118°, std. dev.: 12°
cone depth	max.: $\approx$ 0.65 μm (monotonically decreasing distrib. to max.)
nearest neighbour distance	mean: 0.8 μm, std. dev.: 0.3 μm

Table 3.2.: *Numbers for statistical quantification of the ZnO:Al surface shown in Fig. 3.8. The upper section contains quantities derived from the data field whereas the lower section contains quantities on detected cones only.*

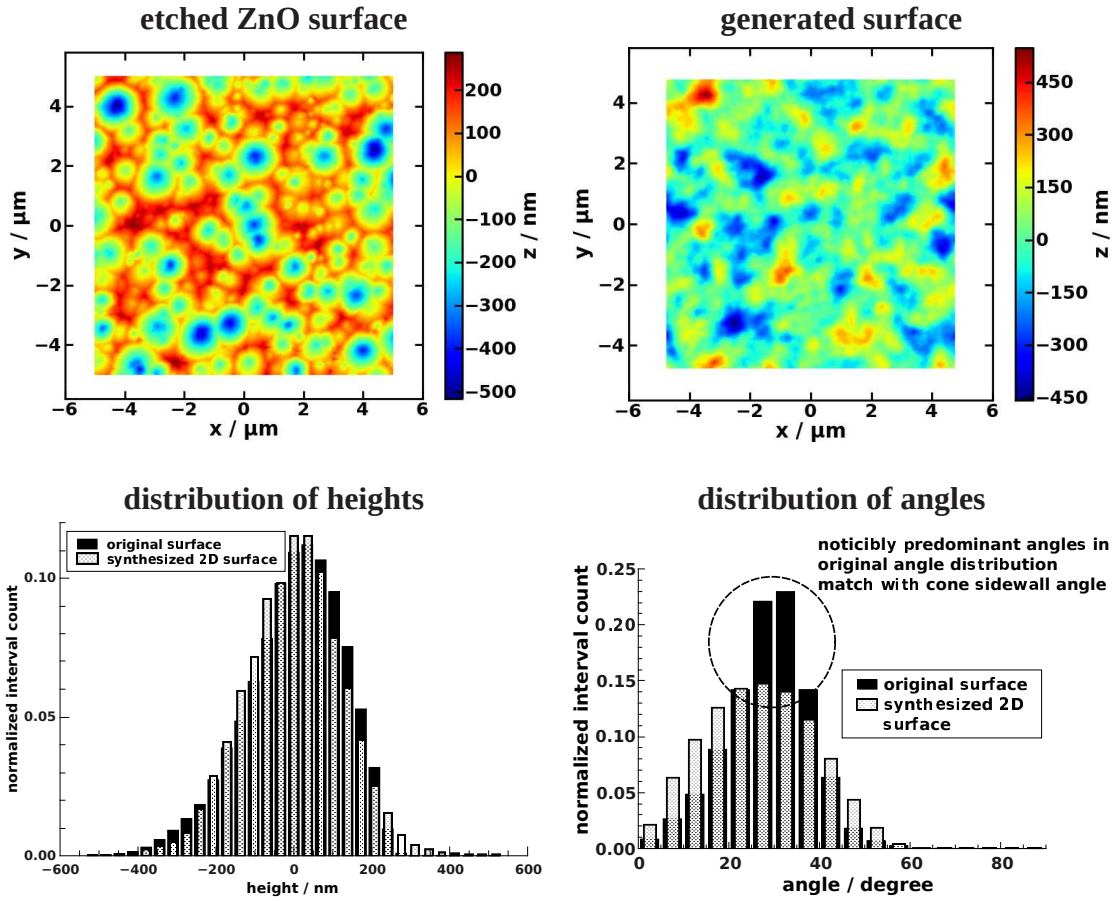

Figure 3.10.: ***Top row:*** *False color image of the AFM data and a synthesized surface generated, according to eq. 2.99, from the 2D ACF depicted in Fig. 3.8.* ***Bottom row:*** *Comparison of height and angle (cf. eq. 2.103) distributions of the experimental and the synthesized surface.*

has a pronounced maximum around 30° which matches the angle towards the global surface normal of the surface of a cone with 120° opening angle. Within the naming scheme of Kluth [Klu+04] the considered surface would be of type “B”.

Synthesization of 2D surfaces

Surface synthesization was performed for this surface with the ACF method described in section 3.2. The original 2D autocorrelation data depicted in Fig. 3.8, upper right, was used for this purpose. Not regarding lateral and height dimensions the synthesized surface depicted in Fig. 3.10 is morphologically similar to the synthesization of the FTO surface depicted in the previous section. It does not show the characteristic shapes of the original surface.

A comparison of the generated height distribution to the original height distribution is de-

picted in Fig. 3.10, bottom left. The generated height distribution does not show the skewness found in the experimental data. A similar comparison of the local angle distribution with respect to the global surface normal is depicted in Fig. 3.10, bottom right. While the angle distribution of the synthesized surface is relatively broad the experimental data shows a pronounced maximum at the surface angle corresponding to the cone opening angle.

3.2.4. Conclusion

The FFT based synthesization algorithm for periodic rough surfaces described in section 2.4.1 showed a good performance in case of the FTO roughness type but not in case of the AZO roughness type. The employed algorithm is not considered a good approach for modeling the AZO surfaces. In this case other synthesization methods need to be developed, which reproduce the characteristic conical shapes of the surface etchings.

As the roughness model for further use in this chapter the gaussian ACF model for the FTO surface roughness was chosen. This choice was made mainly in view of the limited domain size in 3D simulation, to be able to do a series of simulations at several domain widths. Note that the simulated material system is a polycrystalline silicon cell, described in section 2.1.4, with a ZnO:Al front contact.

3.3. Solar cell simulation

3.3.1. Device layout and simulation algorithm

The solar cells simulated in this chapter are single junction polycrystalline silicon solar cells in the superstrate layout with a structure suitably simplified for optical simulation, as described in section 2.1.4. The simplified layout is depicted in Fig. 3.11. Corresponding nominal (flattened volume) material heights are given in table 3.3 and are used for all simulations within this chapter unless noted otherwise. Transmission through 100 nm silver is below 0.4% for wavelengths in the range 400 nm–1100 nm. Transmittance beyond the back reflector is therefore negligible. The set of material parameters used for simulation can be found in appendix A. To include effects from superstrate light trapping the superstrate and the FEM domain were decoupled incoherently as described in section 2.2.3. Optical absorption intgrals within sub–volumes of the finite element domain were calculated from the complex field energy as described in section 2.2.1).

The simulations in this chapter were all based on synthesized rough surface data. The applied surface roughness model was the small scale gaussian ACF roughness model, derived from a tin oxide surface in section 3.2.2. As no model for the thickness dependent change of the surface morphology was available the surface roughness of the front TCO layer was propagated to the following surfaces as shown schematically in Fig. 3.11. A Monte Carlo sampling over rough surface representations was used to obtain average absorptance, reflectance and transmittance values at a single wavelength.

In 2D simulations averages of s– and p–polarization were used to compute the polarization incoherent response of the system (cf. section 2.2.2).

layer	**nominal height in nanometer**
glass	not relevant (no absorption, incoherent coupling)
front ZnO:Al	500 nm
c–Si	1200 nm
back ZnO:Al	85 nm
silver	> 100 nm

Table 3.3.: *Volume equivalent flattened cell height structure as used in most simulations in this chapter.*

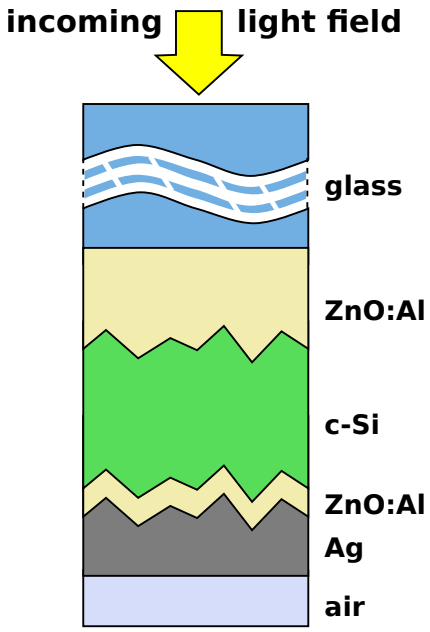

Figure 3.11.: *Optical cell layout of the solar cells with random interfaces as used in the simulations. For the characterization purposes in this chapter the small scale roughness of the tin oxide surface characterized in section 3.2 was applied to the ZnO:Al/silicon interface. The texture is propagated without change to all other rough interfaces.*

3.3.2. Model error sources

Ideally, the space resolved simulation domain for finite element analysis consists of a laterally very large cell model which completely covers rough surface statistics and for which boundary effects are negligible. But memory and computation time requirements of the FEM simulation limit the actual domain size to hundreds of micrometers in 2D and a few micrometers only in 3D. Insufficient statistical information within a single surface representation can be resolved by a Monte Carlo sampling as described in section 2.3. The sampling always converges but not necessarily to the averages of the experimental case of an extended rough surface. In a laterally periodic layout the experimental case should be approximated well if the computational domain is bigger than twice lateral optical correlation length of geometrical features in the solar cell. If the computational domain is smaller there is no natural choice of the lateral boundary condition to be applied to the computational domain for physical reasons. An error is possibly introduced by the boundary condition and needs to be characterized.

Possible boundary condition settings with completely different reflection properties at the domain boundary are periodic boundaries or transparent boundaries to a flat layered medium. Both cases are schematically depicted in Fig. 3.12. In the periodic setting any energy flux

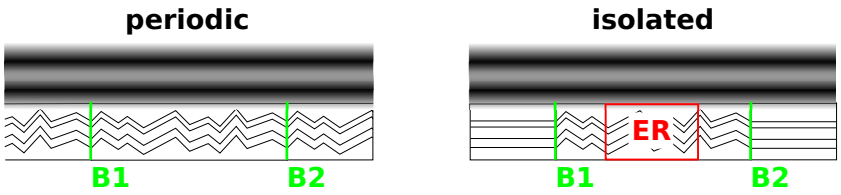

Figure 3.12.: *Illustration of periodic and isolated boundary conditions for rough surface multilayer geometries. See text for details.*

through the interface *B1* into the computational domain corresponds to an energy flux out of the domain through the interface *B2* and vice versa. The position of the periodic boundary is arbitrary and does not make a difference for charge carrier generation at any point in the domain. In case of the isolated layout charge carrier creation close to the boundary of the computational domain will on average be different from carrier generation in the center of the domain because light is scattered only outwards through the boundaries *B1, B2*. If the simulation domain cannot be chosen very large in case of the isolated problem, a suitable technique is to evaluate absorption integrals only in a central evaluation region of the isolated domain, as indicated by the region *ER* in the schematic. When using this method a higher number of surface samples may be required for statistical averaging than in the periodic case.

Both periodic and isolated computational domains were extensively characterized and compared in 2D simulations. The results of this analysis are presented in section 3.4.2. In 3D simulations of solar cells with 2D rough surfaces three different domain widths were compared with lateral periodic boundary conditions to discuss artifacts introduced by the periodicity. The results can be found in section 3.5.1.

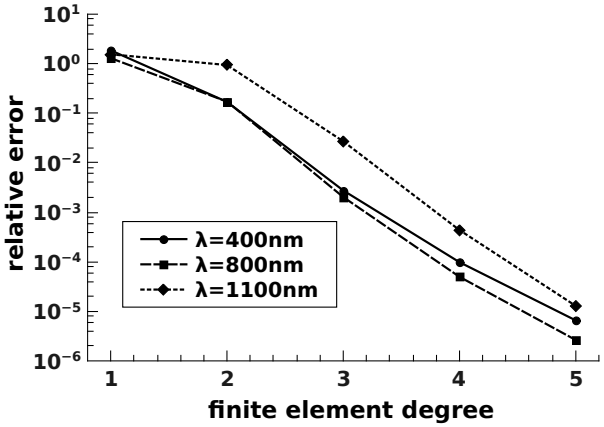

Figure 3.13.: *Convergence of a cartesian grid slice of field values in a 2D FEM problem over finite element polynomial degree for a fixed discretization. The vertical solar cell layout is described in sec. 3.3.1. See p. 26 for expectations on finite element convergence behaviour.*

3.4. Simulations of 1D rough surfaces

This section presents an extensive characterization in 2D as a basis for a more limited rationale in 3D where computational restrictions are much higher. Especially the discretization of surface texture and the finite element solution of Maxwell's equations can be done at a quality where their errors can safely be ignored in comparison to the Monte Carlo sampling error and artificial boundary error to be characterized here. An example convergence for a 200 μm wide 2D cell representation with interface texture is depicted in Fig. 3.13. Finite element solutions of the s–polarized problem where computed up to order 6 which was used as quasi–analytic reference for comparison and normalization. Field values on a cartesian grid slice through the computational domain where used for error measurement. Field values typically show the largest errors. Convergence curves for integral quantities based on intensity like field energy or absorption typically lie below the shown ones by an order of magnitude or more. Memory consumption stayed below 32GB for all finite element degrees in this analysis.

For all 2D simulations in this chapter finite element solutions with an expected relative error lower than 10^{-4} were chosen. The complete characterization of the following sections was done on polarization averaged target quantities. Difference between s– and p–polarization are mainly due to plasmonic absorption in the back reflector and are quantified in section 3.4.3 where the cell results are presented.

3.4.1. Characterization of the Monte Carlo sampling

Monte Carlo convergence analyis was performed on the solar cell layout as defined above (p. 74) excluding the superstrate / air interface, i.e. for the finite element domain embedded between two half spaces of glass and air. Periodic boundary conditions were applied as lateral boundary conditions of the computational domain. The convergence analysis was performed on the absorption integrals of the cell's layers for domain widths between $5\,\mu$m and $80\,\mu$m. A total of $n = 90$ random surface representations was simulated at each domain width. The standard deviation σ was calculated from the obtained distributions of absorptance in the different layers of the solar cell.

Wavelength resolved plots of the standard deviation of samples at all domain sizes are depicted in Fig. 3.14. Estimations on required sample size k at a chosen error threshold were computed from the inverse square root law of the central limit theorem (see also section 2.3),

$$k = \left\lceil \left(\frac{\sigma}{\sigma_{S_k}} \right)^2 \right\rceil , \tag{3.1}$$

where $\sigma_{S_k} < \sigma$ is the desired tolerance level. The resulting sample sizes are depicted in Fig. 3.15 in an order corresponding to the Fig. 3.14. The exact value of an extrapolation to small σ_{S_k} may be questionable but the resulting sample sizes should be useable as an order of magnitude estimate. To highlight layer dependencies and the unfavorable convergence properties of the Monte Carlo method for obtaining low relative errors the standard deviation of the absorptance weighted with the mean value of the absorptance was used to calculate the values in the first column of the diagrams. The absolute absorptance deviation is more interesting for experimental comparison and solar cell performance, as discussed in section 2.2.4, and was used in the second column of the diagrams. To generate the sample size estimates in Fig. 3.15 a threshold of 0.01 was used on both scales.

On the relative scale in the left column of Fig.3.14 the main difference can be noted between the front TCO layer and all other absorbing layers of the device. The relative standard deviation of the absorptance shows no strong wavelength dependency whereas the values of silicon span more than one order of magnitude. The back TCO and silver layers also show a strong wavelength dependency of the relative standard deviation with a correlation to the curves of the silicon absorber for wavelengths above 600 nm. Below 600 nm absorptance in silicon is very high and not much light reaches the rear layers. The wavelength depencency of the curves mirrors the variation of the absorption coefficents of silicon and ZnO:Al which are depicted in appendix A. The absorption coefficient of silicon drops by more than an order of magnitude between 600 nm and 1000 nm wavelength whereas the variation in the absorption

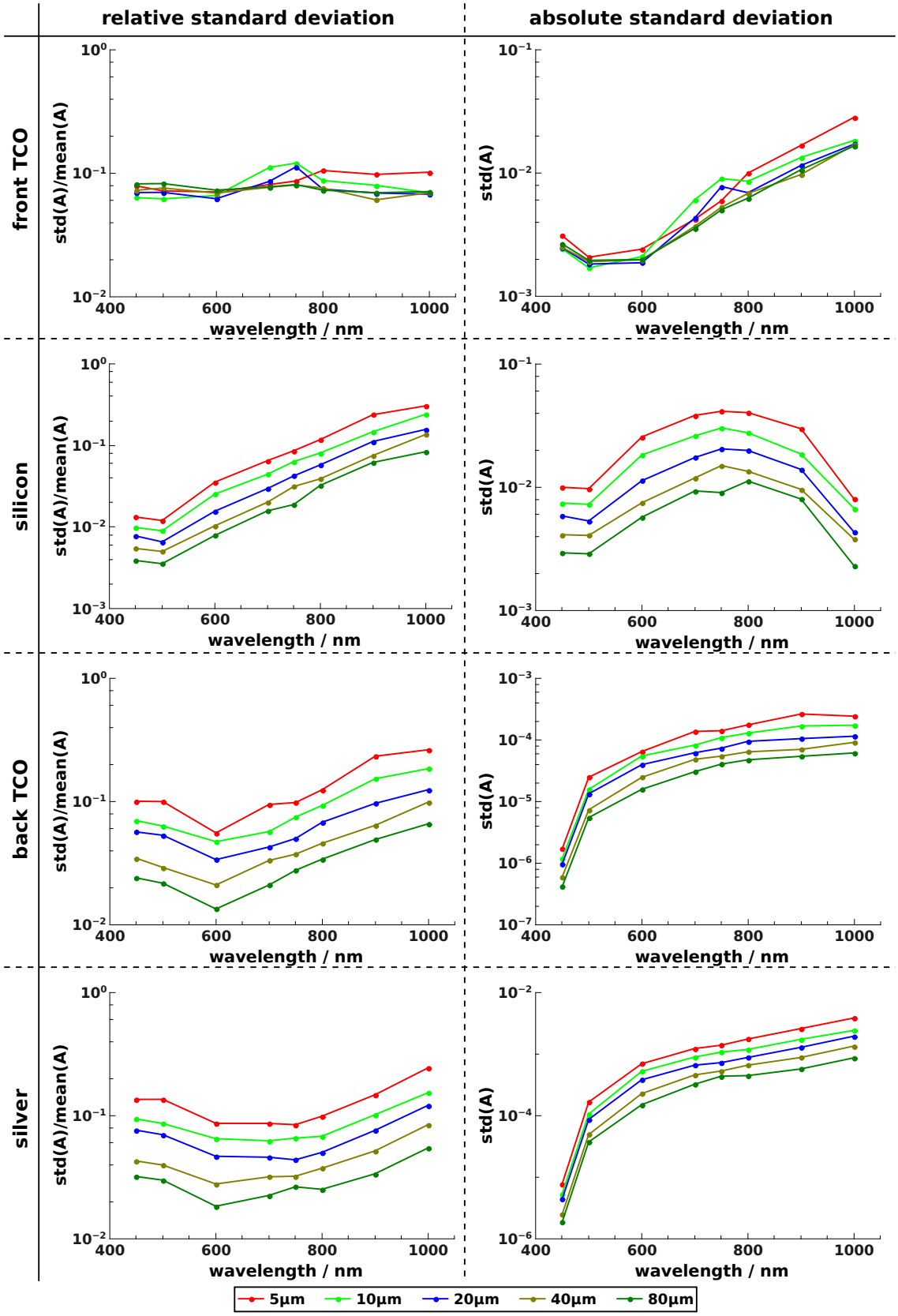

Figure 3.14.: *Wavelength resolved standard deviation of absorptance values in a samples of 90 representations at different domain widths. Diagrams in the left column show the standard deviation in a relative norm while diagrams in the right column show the standard deviation in absorptance units. Necessary sample sizes for 1% error thresholds were derived from this data and are shown in Fig. 3.15.*

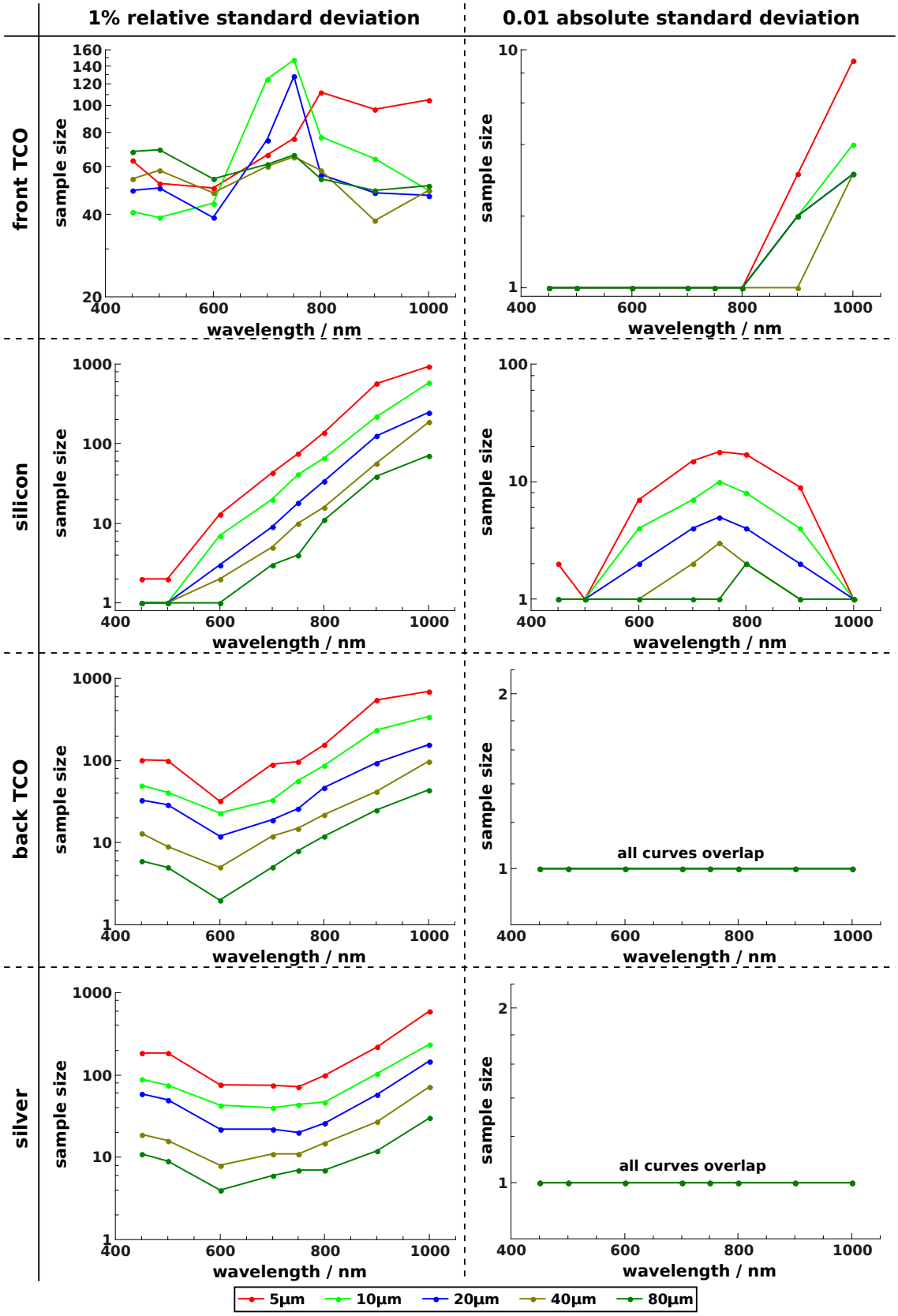

Figure 3.15.: *Required sample sizes to obtain a 1% relative standard deviation (left column) and 0.01 standard deviation of the absorptance (right column).*

coefficient of ZnO:Al is smaller in that range.

On the absorptance scale in the right column of Fig.3.14 the error is clearly dominated by silicon at wavelengths below 800 nm and by ZnO:Al above 800 nm for larger domain pitches. The standard deviation of the absorptance is highest in silicon at wavelengths around 750 nm where the absorptance gain from light trapping is largest. Similarly the increasing absorptance gain in the front TCO can be found in the diagram for that material in the right column. Deacreasing absorptance in silicon leads to an increase of absorptance in the front TCO, i.e. the absorption properties of silicon are reflected in the standard deviation of absorptance in the front TCO. The standard deviations in the back TCO and silver layers are not important on that scale.

The curve shapes in Fig. 3.14 are mirrored in Fig. 3.15 where required sample sizes for reaching a 0.01 tolerance level on either scale are shown. With a dependency on the domain size large sample sizes are required to reach a low relative error in the high wavelength range. The obtained sample sizes in the low refractive index range of silicon match with the sample sizes reported to be used in radar scattering simulations [HSB95] with surfaces of rms roughness and correlation length equal in wavelength units to the etched ZnO:Al surface type described in section 3.2.3. As low absorptance values at isolated wavelengths do not give a high contribution to the cell current the sample sizes depicted in the right columns of Fig. 3.15 are more meaningful for the simulation of a PV device. A maximum number of 20 samples is sufficient for a 5 μm large computational domain to obtain a standard deviation of 0.01 on the absorptance scale.

For the surface generation it is expected that the number of samples required to reach a fixed tolerance level in the statistical distributions reduces to half when the domain width is doubled. An according behaviour was found for the optical response of the silicon, back TCO and silver layers but not in case of the front TCO layer.

3.4.2. Characterization of the boundary conditions

Description

In the previous section the convergence of the Monte Carlo averaging was studied at different computational domain sizes but it was not shown that the solutions converge to the same average value. In experimental measurements areas of a few square millimeters or even square centimeters are usually illuminated on the sample. Domain widths used in simulation are smaller than the experimental extent of illuminated areas and much smaller than the actual sample size. Influences of limited sample size and the chosen lateral boundary conditions

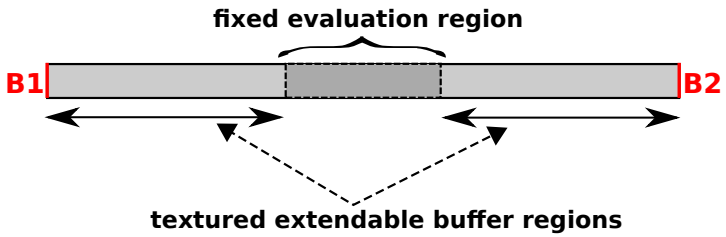

Figure 3.16.: *Schematic of the implemented radius of influence analysis for boundary condition testing.*

therefore need to be characterized. From the path length of 90% absorption in silicon depicted in Fig. 2.4 it can be assumed that with a few hundred micrometer wide computational domains these boundary effects may be safely ignored. The solution should then become a very good approximation to the experimental conditions in the center of the computational domain for all boundary types. Computational domains of that width can be simulated in 2D but in 3D the domain width is usually limited to a few micrometer.

The objective of the study presented in this section was to provide an estimate for the wavelength dependent domain size required to keep boundary effects below a certain error threshold as well as the best boundary condition to be applied for minimal computational domain size. Therefore a comparison of periodic and isolated boundary conditions was performed. Similar studies have been done for optical proximity correction modeling in optical lithography and are known as “radius of influence” analysis [PDW07].

For both applied boundary conditions the domain variant with a central evaluation domain as described in section 3.3.2 was used. The basic idea of the analysis is depicted in Fig. 3.16. The width of the central evaluation domain was chosen to be $10\,\mu$m. For the analysis of average disturbances it is necessary to do a statistical sampling over surface representations as described in the previous section. To keep the boundary condition analysis clear of the effects of error distributions in Monte Carlo averaging and to monitor only the influence of the additional disturbance when going to a larger domain width the simulations for all domain widths were done using the same sample of rough surfaces. For this purpose a sample of 50 large rough surfaces of $200\,\mu$m width was created and stored. For simulation of a specific domain width below $200\,\mu$m a corresponding part of each surface was cut from the sample. To meet the requirements for the isolated domain layout to extend to a flat layered system and for the periodic layout to have identical height values at the boundary the surface roughness was smoothly damped to its mean value in a $2\,\mu$m interval at both boundaries (B1, B2 in Fig. 3.16). This interval was also chosen as the minimum buffer size. The texture sample within the evaluation domain is always identical. When comparing two representations at different domain

widths the geometric disturbance creating the difference in the scattered fields lies between the inner smoothing boundaries of the smaller domain and the respective domain boundaries of the larger domain. As experimental rough surfaces are not periodic the evaluation has been done not only within the set of domain widths of one chosen boundary condition but also of the periodic set to the isolated set.

The solar cell structure used for the simulations in this sections is as described in section 3.3.1 without considering the superstrate light trapping. The light source used for the simulations is a plane wave at normal incidence on the solar cell stack from a glass half space.

Results

The front TCO and silicon layers were considered for discussion in this section because the absorptance in the back TCO and silver layers was comparatively low. These layers had been also been seen dependent on the silicon layer in the analysis of the Monte Carlo averaging presented in the previous section.

Absolute differences of the average absorptance computed in the evaluation domain with reference to a 200 μm wide computational domain are depicted in Fig. 3.17 for the two different boundary conditions. For both considered materials larger computational domains are required in the long wavelength range to reach a chosen error threshold. This can be attributed to the variation of the absorption coefficient of silicon over several orders of magnitude between 450 nm and 1000 nm. The coefficient of ZnO:Al does not vary considerably in that range. Propagation inside the silicon layer therefore also seems to strongly influence absorption in the front TCO layer at large distances. As a consequence errors due to distant disturbances on the absorptance scale (cf. section 2.2.4) are more important in the front TCO layer in the high wavelength range. The difference between the convergence behaviour of the two lateral boundary conditions is not large in case of the front TCO at buffer sizes of 20 μm and above. For the silicon absorber the absorptance deviation from the reference case lies at values below 10^{-2} already at the smallest buffer size when applying periodic boundary conditions. When applying transparent boundaries to a flat layered medium a buffer size of less than ten micrometer to obtain an equally small error. The convergence behaviour with increasing domain size was found to be smooth and monotonic only with the periodic boundary condition in case of the front TCO and with the isolated boundary condition in case of the silicon. With the isolated boundary condition curves are also smooth in case of the front TCO but errors increase at low buffer sizes before convergence towards the reference case starts. There is no smooth convergence behaviour for the absorptance in the silicon layer with increasing domain size and periodic boundary conditions. This might be due to artifacts of the periodicity.

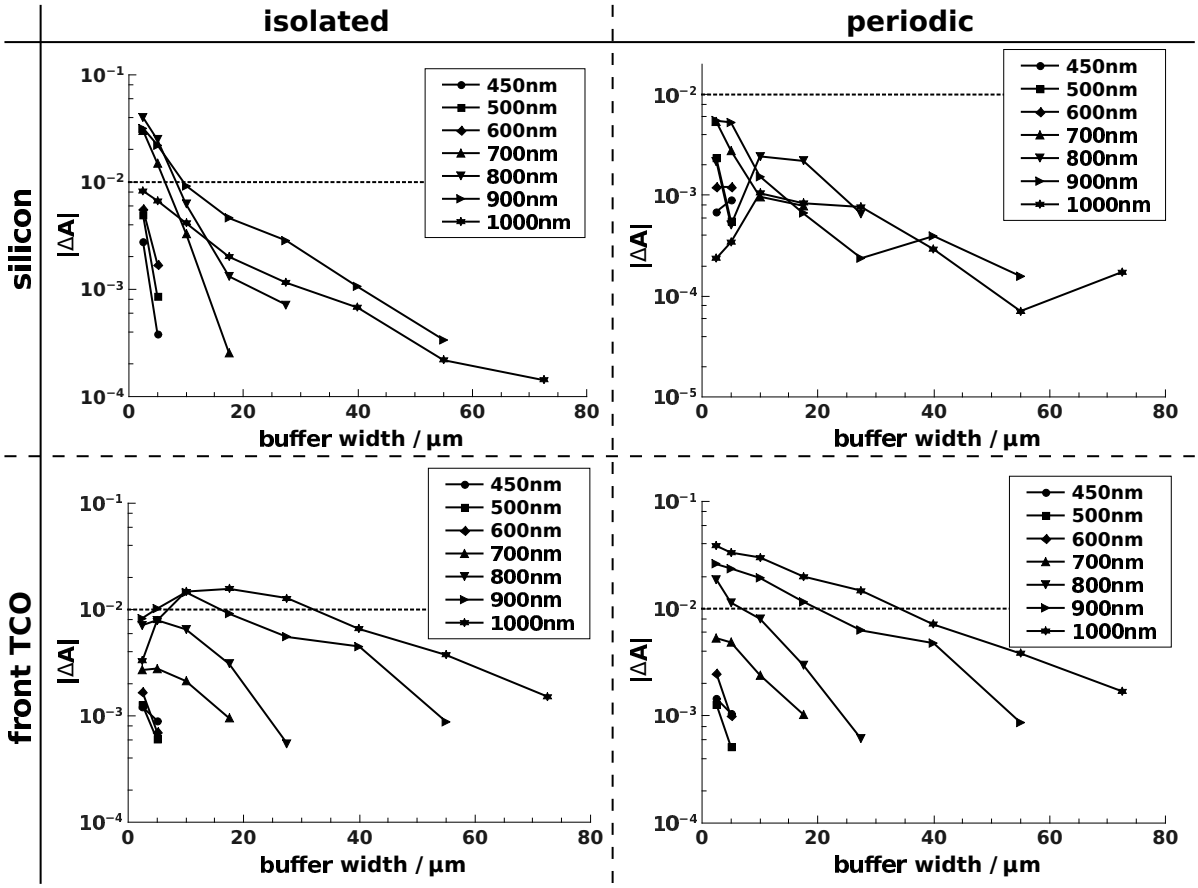

Figure 3.17.: *Plots of the absolute absorptance difference over buffer width in the silicon and front TCO layers. The buffer is applied to both sides of the evaluation domain as depicted in Fig. 3.16. Computational domains were enlarged until the relative absorptance difference with respect to the largest simulated domain size was below 1% for the second and third widest domains.*

For the radius of influence analysis a 0.01 deviation threshold was chosen on a relative and on an absolute absorptance scale, as in case of the Monte Carlo sampling. A relatively simple algorithm has been used for computation of the radius of influence:

- For each boundary condition as well as for the periodic against the reference of the isolated boundary condition and each wavelength, do:
  - Find the last pair of values of which the first is $>= 10^{-2}$ and the second is $< 10^{-2}$ and interpolate the buffer width at the 10^{-2} threshold linearly between the two values on a logarithmic scale.
  - If all values are $< 10^{-2}$ attribute 0 to the buffer width at the threshold value.

The results of this evaluation are depicted in Fig. 3.18. In the first column where absorption

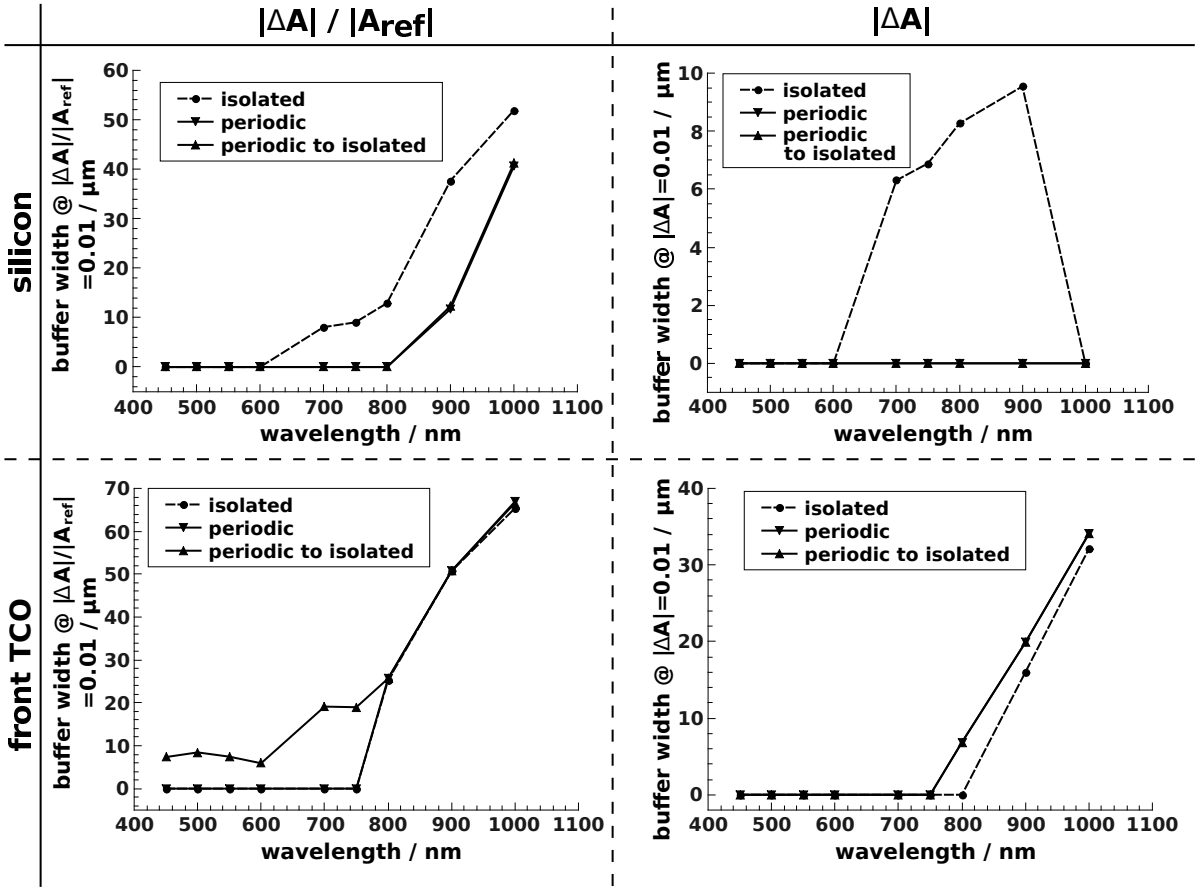

Figure 3.18.: *Buffer width for 1% influence in absorptance relative to the reference solution (left column) and on the absolute scale (right column) for the silicon absorber and the front TCO layers. The buffer is applied to both sides of the evaluation domain as depicted in Fig. 3.16. The initial 2 μm buffer at the two sides of 10 μm wide evaluation region of the computational domain are not included.*

differences to the largest domain reference solution at each wavelength are scaled by the reference solution the required buffer size increases steeply at above 800 nm for both materials. This is the region where the absorption coefficient of silicon gets very low and light trapping effects become important for the solar cell. The comparison on this scale also reveals that the reference solutions for periodic and isolated boundary conditions seem to be very similar already at low buffer size for silicon and at buffer sizes above 20 μm for ZnO:Al. When scaling differences to the incoming power the increase in required buffer size is less dramatic at high wavelengths. For the silicon absorber the choice of a 10 μm large evaluation domain already seems to be sufficiently large whereas in the case of the front TCO required additional buffer size decreases to about 0.5 of the value on the other scale. While for the ZnO:Al the domain size requirements of the isolated and the periodic layout do not differ by much the difference

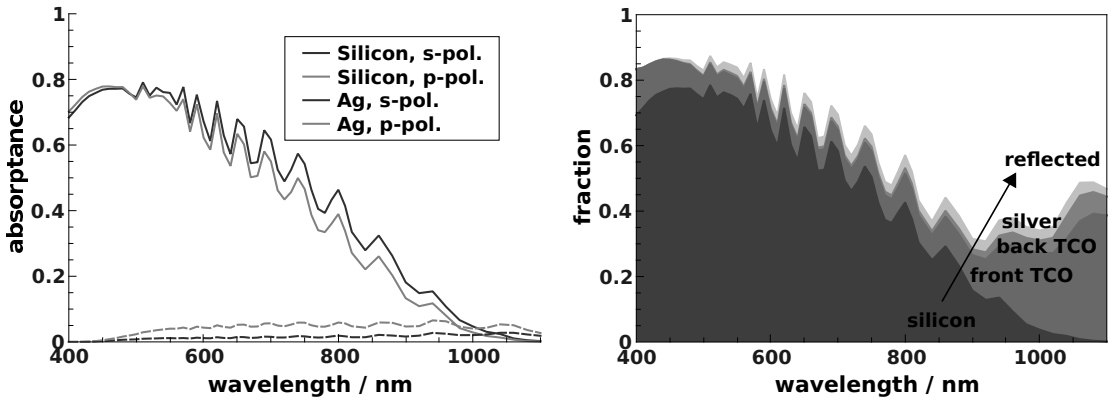

Figure 3.19.: ***Left:*** *Comparison of the silicon and silver absorptance for s– and p–polarization.* ***Right:*** *Polarization averaged fractions of the total device absorptance, absorbed in the individual device layers.*

is more pronounced in case of the silicon absorber where an isolated layout requires a larger buffer size for wavelengths above 600 nm.

The above results slightly favour the use of periodic boundary conditions for light trapping simulation which have the additional advantage that absorption integrals can be evaluated over the whole computational domain and not just its center, as done in this study for reasons of comparability only. This outcome is also favourable in the view of 3D simulations.

3.4.3. Quantum efficiency and losses for 1D rough surfaces

Using the characterization results of the previous sections a solar cell as described on page 73 with a 1D roughness synthesized from the gaussian fit to the FTO autocorrelation function described in section 3.2.2) was computed. Sample sizes and domain widths were chosen such that statistical standard errors are expected to be smaller than 1% of the average value and boundary influences are expected to be below 0.01 in absorptance diagrams. Initial back reflection and superstrate light trapping effects were included in the simulation as described in section 2.2.3.

The results of the computations are depicted in Fig. 3.19. In the left diagram the difference between s– and p–polarized incoming light is shown. The right diagram summarizes polarization averaged absorptance fractions of all materials. In the comparison of polarizations a small difference between the two polarizations opens up at wavelengths above 500 nm. The absorptance fraction of silicon decreases for p–polarized light with respect to s–polarized light. At the same time the absorptance fraction of silver increases by about the same amount. This additional loss can be explained by enhanced plasmonic absorption as propagating polariton

solutions to Maxwell's equations at a flat interface exist only for the p–polarized case [NH06]. As incoming light is generally unpolarized and the local angle distribution on rough surfaces is further isotropic the average of s– and p–polarization has been chosen for the diagram in Fig. 3.19, right. Despite of the scattering surfaces a pronounced interference pattern can still be observed. This is also seen in experimental results for weakly etched ZnO:Al surfaces, as measured by Lechner [LGH04]. Overall the decay in silicon absorptance and reflectance of the simulation agrees well with the least etched TCO from Lechner's series up to 800 nm wavelength.

3.5. Simulations of 2D rough surfaces

Simulations of solar cells with 2D rough surfaces were performed using the same materials, height structure and roughness generating autocorrelation function as for the 1D rough surfaces described in the previous section. Geometric models of small 3D patches of the solar cell were created using the custom 3D grid generation software described in section 2.4.2. An example 3D unstructed grid with 1.5 μm period as used for the computations is depicted in Fig. 3.20, left. Available computational resources with up to 256 GB of RAM would have allowed to use representations of more than 2 μm $\times$ 2 μm area in principal but the required spectral and statistical sampling of rough surface representations lead to the decision to only simulate domain sizes up to 1.5 μm $\times$ 1.5 μm. Samples at 0.75 μm, 1 μm and 1.5 μm domain width in both lateral dimensions were simulated for comparative study. Periodic boundary conditions were applied to the lateral boundaries of the computational domain. A plane wave propagating in the direction of the solar cell stack normal was used as incident field for all simulations. The wavelength range of the simulations was $\lambda = 500 \ldots 1100$ nm for 0.75 μm and 1 μm domain pitch and $\lambda = 600 \ldots 1100$ nm for 1.5 μm domain pitch. Except for the finite element convergence results presented below memory consumption of all simulations was under 60GB.

3.5.1. Characterization

Numerical convergence for a single surface representation

A finite element degree based error analysis was done on a single rough surface surface representation of 1 μm domain width. The complete solver including the incoherent superstrate coupling was used for this test. This was done to include the possibility of increasing error due to insufficient quality of the solution for certain sources on the Bloch periodic grid of

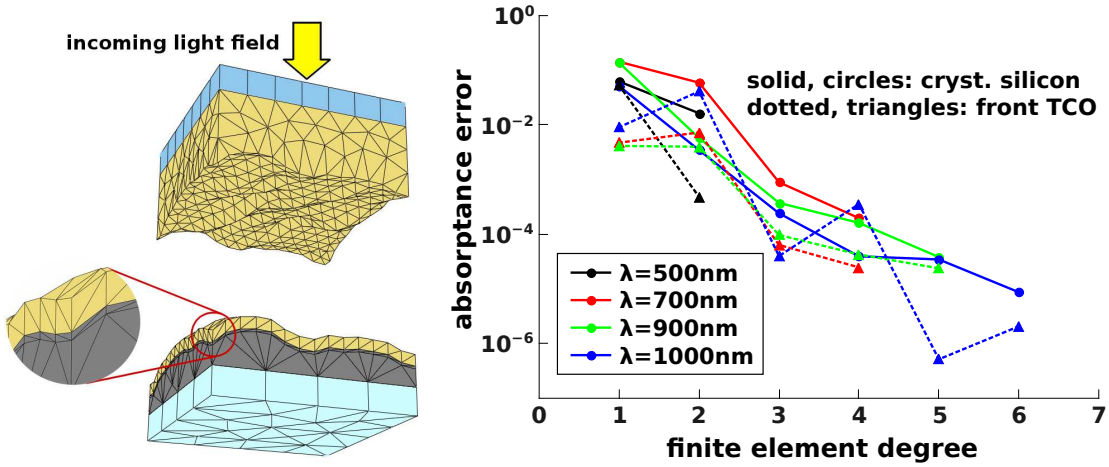

Figure 3.20.: ***Left:*** *Example of a periodic finite element grid. Vertical layout from bottom to top: glass (darker blue) / ZnO:Al (yellow, mean thickness 500 nm) / Si (green, 1.2 µm; removed for grid visualization) / ZnO:Al (yellow, 85 nm) / Ag (grey, min. thickness 100 nm) / air (lighter blue). A thin silver layer at the ZnO:Al / Ag interface (magnified) helps to improve convergence.* ***Right:*** *Convergence of the absorptance integrals in silicon and the front TCO over the finite element degree for a random representation of 1 µm domain period. See p. 26 for expectations on finite element convergence behaviour.*

sources (see section 2.2.3). Errors were computed for the absorbed field energy with reference to solutions with a finite element degree one order higher than the highest degree plotted for all wavelengths respectively. The also experimentally meaningful absorptance scale was used to measure errors, for a discussion see section 2.2.4. The convergence test was done for wavelengths between 400 nm and 1100 nm with a spacing of 100 nm. A subset of results was chosen for presentation in Fig. 3.20, right. The complete set can be found in reference [Loc+11]. A fixed discretization was used at every wavelength. The thin silver layer at the silver / ZnO:Al interface which is highlighted in the grid visualization in Fig. 3.20, left, had shown to significantly improve convergence in a prior study. In case of $\lambda = 500$ nm only two data points could be obtained as a fourth order solution was not possible due to RAM limitations. The error for the silicon absorber is around 0.02 for the silicon absorber in comparison between degrees 2 and 3. The convergence curve for the front TCO at $\lambda = 1000$ nm shows an unexpected increase in error between finite element degree 3 and 4. This artifact might have been caused by the iterative coupling between the glass superstrate and the thin film device and be visible only in the front TCO due to the low absorption in silicon at that wavelength.

The convergence analysis showed that solutions with sufficiently small errors could be obtained throughout the whole wavelength range. For the following results an error below 0.02 was targeted on the absorptance scale between 500 nm and 600 nm wavelength and below 0.01

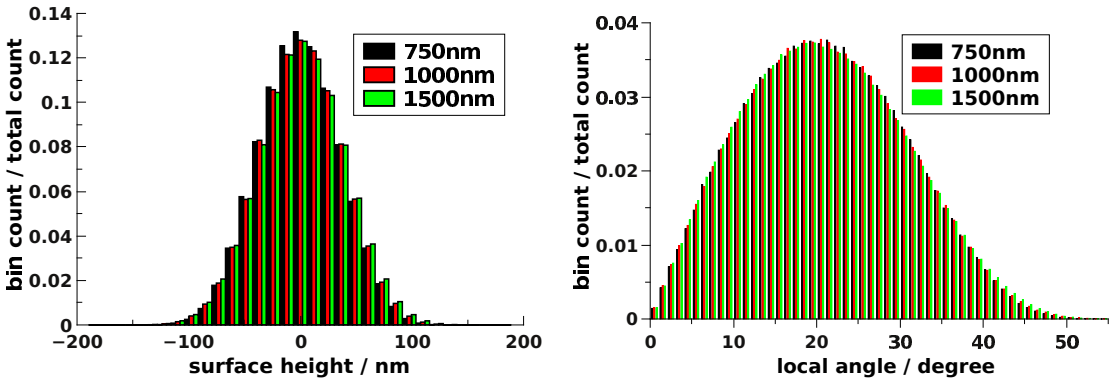

Figure 3.21.: *Comparison of the height and angle distributions of the generated rough surfaces at domain widths of 0.75 μm, 1 μm and 1.5 μm used in the 3D simulations.*

for higher wavelengths.

Statistical sampling

Averaged absorptance and reflectance results were obtained by sampling over a set of representations of the three different domain widths. The smallest domain size was chosen to be 0.75 μm, which is a little larger than twice the autocorrelation length of the ACF used for surface generation. Domain pitches of 1 μm and 1.5 μm were simulated for comparison. The local angle and height distributions at the three different surface periods are depicted in Fig. 3.21. The distributions were averaged over 500 representations each and are quantitatively very similar. Relative differences in comparison to the largest domain period are below 3.8% for the height distribution and below 3.7% for the angle distribution.

For the 0.75 μm, 1 μm and 1.5 μm domain pitches 40, 20 and 10 surface representations were simulated, respectively. A wavelength resolved Monte Carlo error estimation was done from the obtained data, identical to the analysis performed for 2D results in section 3.4.1. As in 2D the main differences were seen between front TCO and absorber layer. The presented results were therefore restricted to these two layers. The relative standard deviations of absorptance in the two layers are depicted in Fig. 3.22. These estimates of the standard deviation of the total population might not be as good as in the 2D case as the sample sizes were smaller. The obtained standard deviations have a similar shape and wavelength dependency as the 5 μm wide sampling in the 2D case.

Wave length dependent standard error estimates at the full sample size were computed from the standard deviations depicted in Fig. 3.22 using eq. 3.1. The estimates were included in

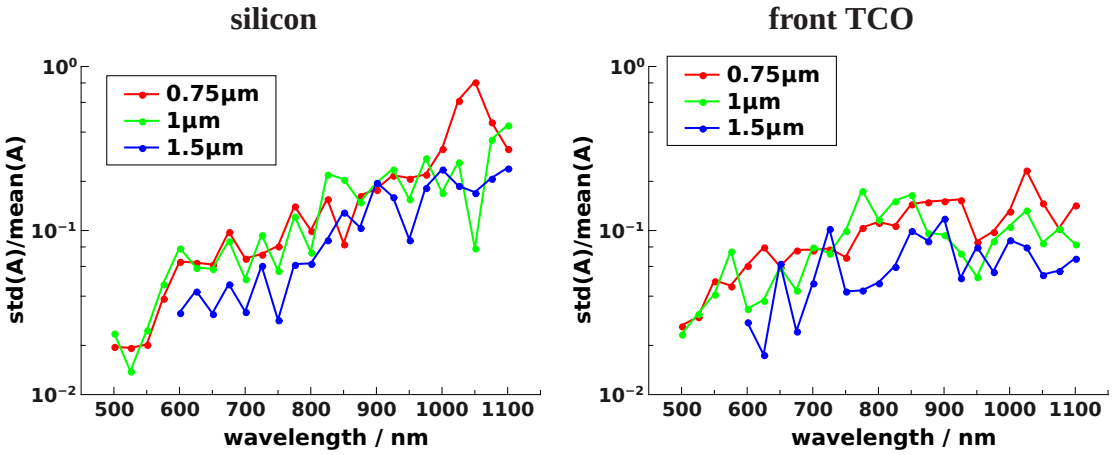

Figure 3.22.: *Wavelength resolved relative standard deviation of the absorptance in silicon (**left**) and the front TCO (**right**). 40, 20 and 10 surface representations were used for 0.75 µm, 1 µm and 1.5 µm domain width respectively. Comparable plots can be found in the analysis of 1D rough surfaces in Fig. 3.14.*

Fig. 3.23 as error bars to the silicon and front TCO absorptance[1].

Domain size effects

A good separation of the statistical sampling from domain size effects as presented in section 3.4.2 for the 2D case could not be done in 3D. Also no reference case at a very large domain width could be computed. The evaluation was therefore based on a visual comparison of the results at the three different domain pitches of 0.75 µm, 1 µm and 1.5 µm. The absorptance of the silicon layer and the front TCO layer are depicted in Fig. 3.23. The diagrams in the first row show the total absorptance. In the second row of diagrams the absorptance due to superstrate light trapping is shown. The error bars in the graphs are estimations of the standard deviation for the sample size calculated at every wavelength and for every material individually. A finite element error estimation was not obtained and averaged for the separate samples. From the above error analysis it is expected to be 0.02 on the absorptance scale between 500 nm and 600 nm wavelength and 0.01 for higher wavelengths. These error estimations were not considered in the diagrams. The statistical error is in the same order as the expected error of the primary solution for most wavelengths and higher for some. Generally expected computational errors are smaller than the differences between the absorptance curves for the different domain pitches.

[1] An error in the interval calculation in the corresponding paper [Loc+11] has been corrected in Fig. 3.23. The standard deviation intervals computed previously for the publication were much too high.

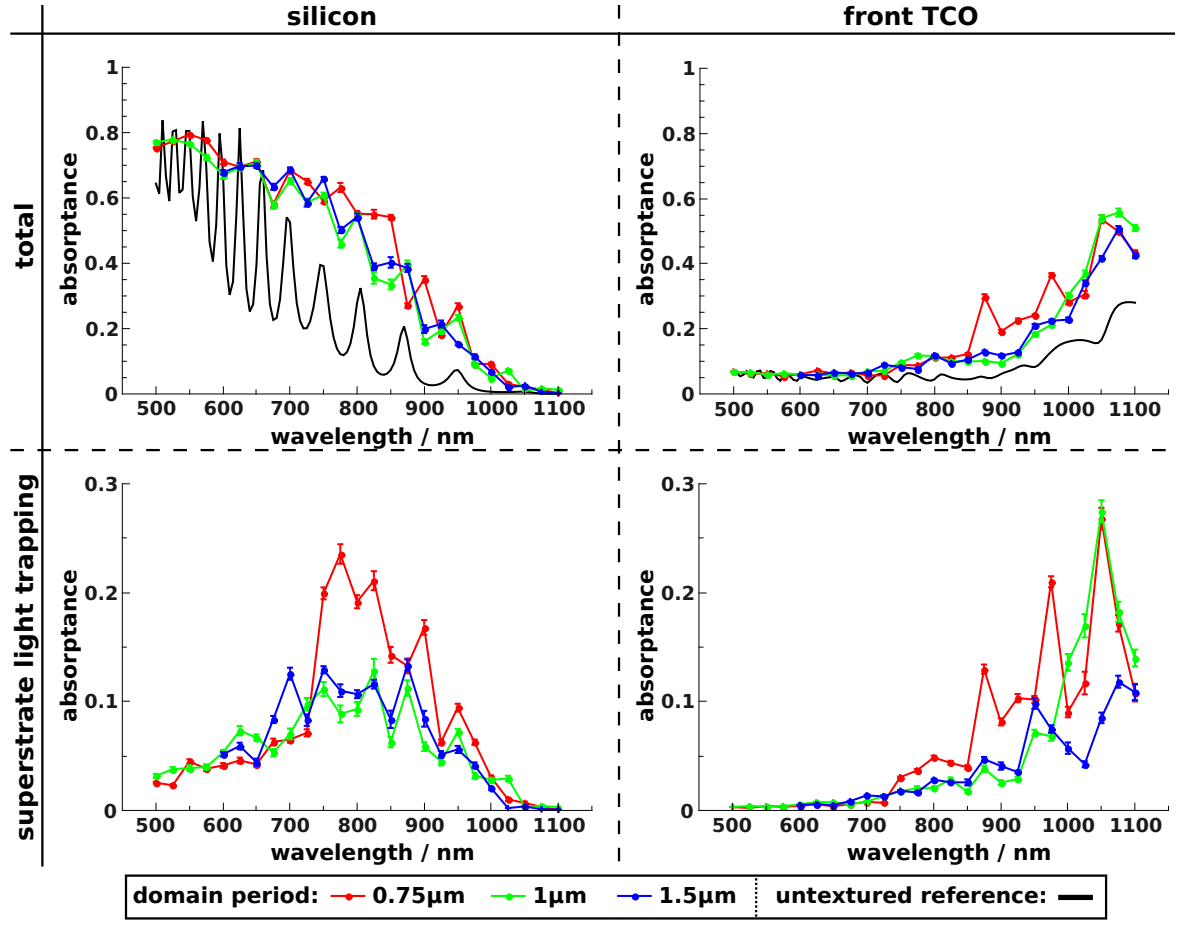

Figure 3.23.: ***Top:*** *Comparison of absorptance in silicon and the front TCO for domain widths* $0.75\,\mu m$*,* $1\,\mu m$ *and* $1.5\,\mu m$*.* ***Bottom:*** *Fraction absorbed after back reflection from the superstrate/air interface. Indicated error bars are estimated standard deviations from statistical sampling (see footnote on p. 89).*

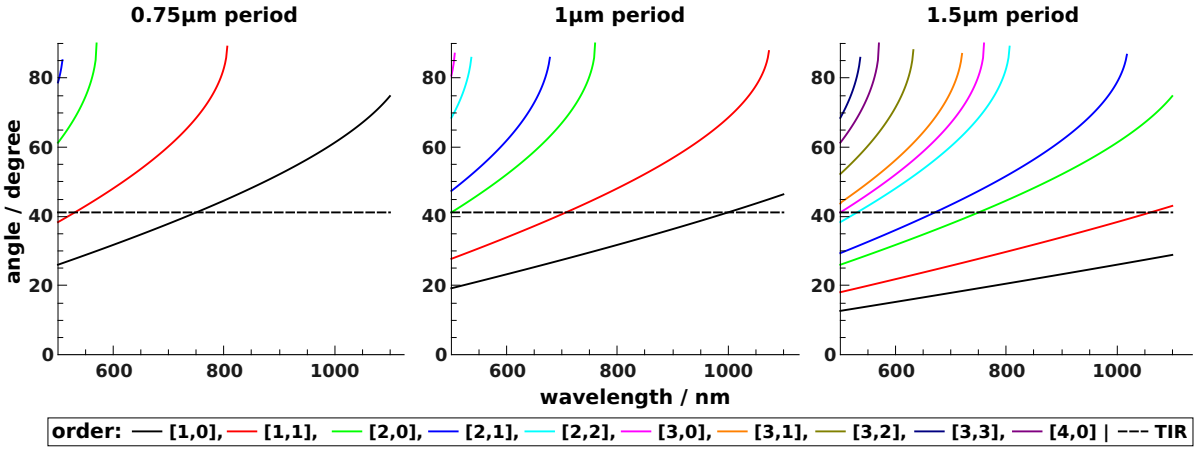

Figure 3.24.: *Propagation angles of reflection orders inside glass for the three domain widths. The angle of total internal reflection (TIR) is marked by a horizontal line.*

In visual comparison the most notable differences between the 0.75 μm domain pitch and the other series appear above 700 nm wavelength for silicon and above 850 nm wavelength for the front TCO. The deviations between the absorptance curves could be partially traced back to the discrete Fourier spectrum of reflected light and the limitation to very few vertically propagating orders in the glass superstrate. Propagation angles of the first non–zero diffraction orders for the three different domain periods are depicted in Fig. 3.24. In case of 0.75 μm domain period all light is defracted into zero order and first order modes at wavelengths above 800 nm. At wavelengths above 750 nm reflection in to the first order modes is at angles above the limiting angle for total internal reflection at the superstrate / air interface in case of this domain period. Visible differences between the absorptance curves as seen in the first row of diagrams in Fig. 3.23 are very similar to the differences in the superstrate light trapping contributions depicted in the second row. The large absorptance increase for the 0.75 μm wide computational domain in silicon for the wavelength range between 750 nm and 925 nm can be attributed to the increased superstrate light trapping efficiency in that spectral range. In case of the 1 μm wide layout the first diffraction order is internally reflected at 1000 nm wavelength and above. When comparing to the 1.5 μm wide layout the most prominent differences can be seen in that wavelength range in the superstrate light trapping contribution of the front TCO in Fig 3.23, bottom right. Additional isolated deviations of about 0.1 are visible at 850 nm and at 950 nm in the absorptance in silicon for these two series. They are not an artifact of the superstrate light trapping but might still be due to the periodic boundary conditions as errors of the statistical distributions on the surfaces and Monte Carlo standard errors were found smaller in magnitude.

3.5.2. Quantum efficiency and losses for 2D rough surfaces

The absorptance fractions of the different layers of the solar cell for 1 μm wide computational domains are depicted in Fig. 3.25, left. Losses in the reflector layers, back TCO and silver, are moderate throughout the whole wavelength range. At wavelengths below 900 nm the same holds for the front TCO layer. Above 950 nm absorption in this layer clearly dominates all other losses. This correlates with the increase of the absorption coefficient of the used ZnO:Al material parameter set in that wavelength range.

The absorptance fraction in silicon still shows interference fringes. Interference visibility is not supposed to vanish completely at the low surface roughness used for the simulations. Experimental quantum efficiencies from cells with a similar structure and low surface roughness show comparable visibility of fringes [LGH04].

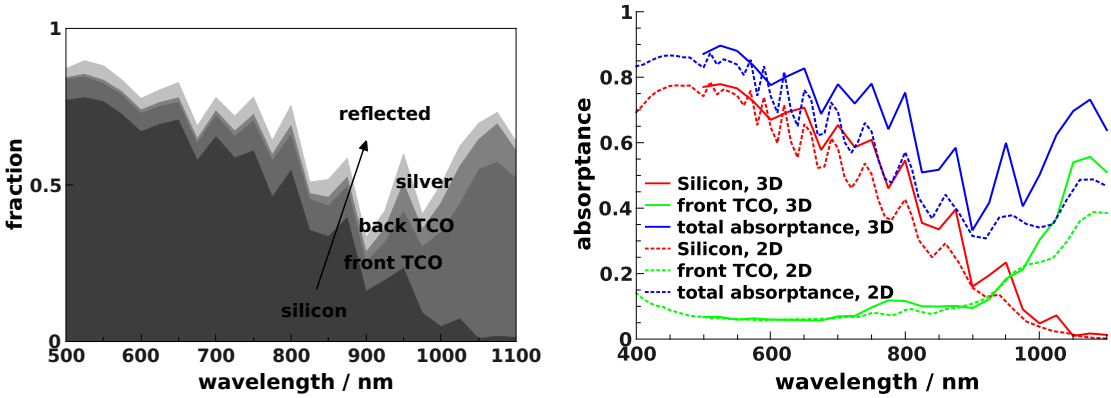

Figure 3.25.: ***Left:*** *Material fractions of the total cell absorptance, simulated with* $1\,\mu$*m domain width.* ***Right:*** *Comparison of results from simulation of 1D and 2D rough surfaces.*

In Fig. 3.25, right, absorptance fractions in the front TCO and silicon as well as the total absorptance of the cell are compared between the 2D rough surface results for $1\,\mu$m domain width and the 1D rough surface results presented in section 3.4.3. No pronounced differences in absorptance exist below 600 nm wavelength. Between 600 nm and 900 nm the absorptance in silicon begins to form a convex "hump" in case of the 2D rough surface which can also be seen in experimental results for solar cells with light trapping. The 1D rough surface results show a more or less linear decrease in the same wavelength range when averaging through the interference fringes. Fringes are more pronounced in 1D roughness as in the 2D roughness case. The results for the front TCO layer do not differ by much up to 900 nm wavelength.

3.6. Rigorous evaluation of a far field data based approximate method

Introduction

Approximate solvers are commonly used to solve multilayer problems incorporating layer interfaces with a random texture in academic and industrial research. For the simulation of wafer cells, where the scattering textures and the wavelength of light are much smaller than the layer thickness, the use of one–dimensional incoherent ray tracing models is adequate and leads to the same results as Yablonovitch's theory [Yab82] for small absorption coefficients [LPS94]. These models, e.g. as described by Schropp and Zeman [SZ98], use measured angular distributions of scattered light or assumptions from scattering theory and geometrical measures of surface roughness to describe light transfer into different angular channels at an interface. Measurement of these distributions is usually done against air which is not the adjacent material inside the photovoltaic device. Especially for interfaces from and to materials with a high refractive index a measurement against air can not be assumed sufficiently close to the light scattering inside the device. Further only information about a limited range of scattering angles inside a highly refractive medium can be deduced when measuring against air. To resolve this issue, several groups recently started applying diffraction integrals like the Rayleigh–Sommerfeld integral to calculate reflection and transmission between arbitrary materials [JZ09; Jäg+11; Dom+10]. These scattering integrals are rigorous solutions to the scalar scattering equations for 2D scatterers in a plane. They can be solved rapidly applying Fourier transformation of the scattering structure. The common approach to transform a surface profile into a plane phase shifting mask using the local height coordinate. This procedure assumes that secondary scattering events can savely be ignored and is known as Rayleigh's hypothesis or Born's first order approximation. This approach is also valid in a mathematical sense if the height of the textures is only a fraction of the lateral feature size [BF79]. The rough surfaces used for light trapping are certainly not within this regime but second order scattering effects should not be prominent in the scattered field at some distance. The scattering integrals are also only used to derive far field intensity data as input to the ray tracing models. Recently a simple scattering model for computation of the angular diffraction on rough surfaces as used in solar cells was validated against rigorous simulations by Rockstuhl [Roc+11].

For thin film solar cells coherence effects can generally not be neglected any more. To resolve this issue models with an added coherent channel have been developed, e.g. by Leblanc [LPS94], Krč [KST02; Krč+03; KST03; Krč+04; ZK08], Springer [SPV04; Spr+05] and re-

cently Lanz [Lan+11]. These solvers were applied for solar cell simulation in many cases and show good comparability between numerical results and experimental quantum efficiencies. They base on the assumption that on reflection or transmission by a randomizing interface only the specular part can carry phase information leading to visible interference effects. This can be motivated by the translational symmetry of the rough surface which also needs to hold for the scattered field and thus does not allow coherent information at non–specular angles [DG09]. Therefore, these simulators assume a low geometrical correlation between two facing randomizing surfaces so that the translational symmetry argument holds between them. In thin film photovoltaics where textures are propagated from one interface to another by directional or conformal growth mechanisms and texture feature sizes are of the same dimension as the layer thickness this is not necessarily true any more. It is therefore interesting to measure how these algorithms perform in comparison to a rigorous simulation with increasing layer thickness.

In the study presented here an approximate solver implementation was compared to Monte Carlo averages of rigorous simulations. The input far field data required by the approximate solver was calculated from rigorous simulations. The studied geometry was a finite layer of silicon with the FTO interface roughness described in section 3.2.2 between two half spaces of air.

Implementation of the approximate solver

There is no general rule on how to introduce phase information into the ray tracing system but for the requirement that energy has to be conserved. The easiest way to ensure conservation of energy is to represent the partially coherent response of the system as the incoherent sum of a completely coherent system and a completely incoherent system. This algorithmic approach is schematically depicted in Fig. 3.26 and used by many implementations of such solvers. The flat multilayer system is calculated using a transfer matrix formalism (see sec. 2.2.1) and the rough multilayer system using ray tracing based on prescribed scattering transfer functions for intensities. The field distribution shown at the bottom of the schematic motivates that this substitutory system might be a good choice at least for some configurations. There is a basic requirement for this kind of splitting to be without error at a single rough interface: In the specular direction the reflected and transmitted power in both systems must be equal (cf. Schropp and Zemans assumptions, [SZ98]). However, this will not always be the case as shown in the right diagram in Fig. 3.26. In this diagram the rigorous polarization averaged power splitting at a 1D rough interface for a 10 μm wide computational domain computed for light incident from crystalline silicon into air and from air into crystalline silicon is compared

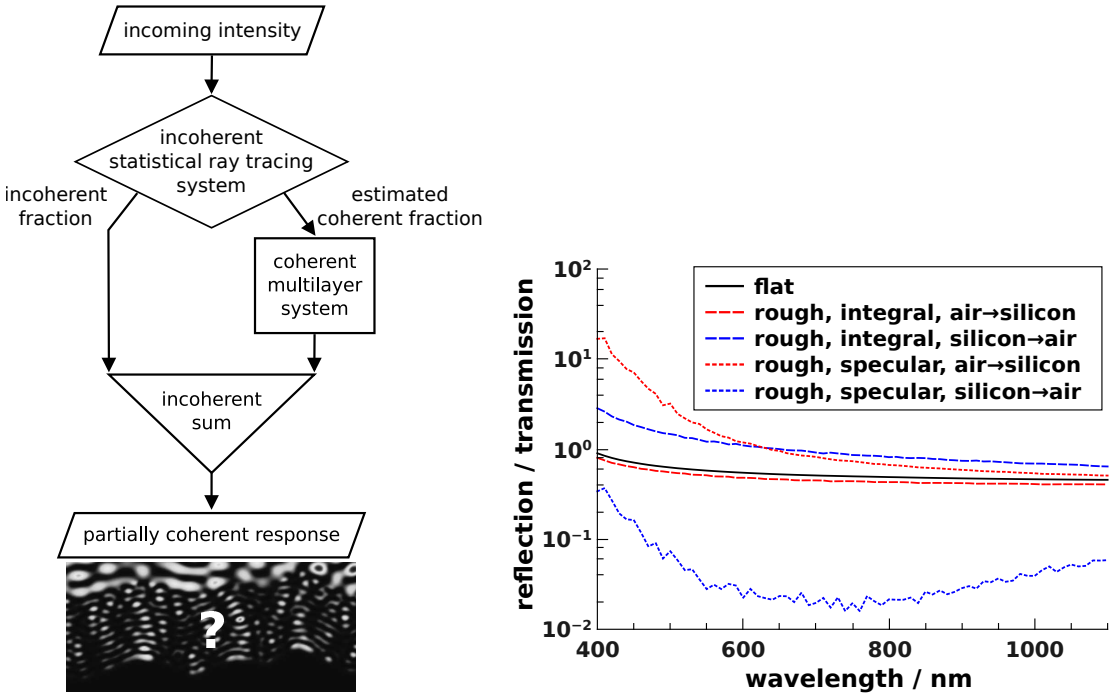

Figure 3.26.: ***Left:*** *Algorithmic concept of approximate 1D simulators for multilayer problems with rough interfaces.* ***Right:*** $\frac{R}{T}$ *at 90° incidence for flat and rough layers in the test case.*

to the flat layout. The diagram shows the ratio of reflected and transmitted power fluxes. The specular fluxes of the rough layout and the flat layout alone do not fulfill the requirement. In case of the total flux the equal splitting requirement is holds quite well for the case where the field is incident in air and transmitted into silicon but not for light incident from the silicon side. The reflection is much higher in this latter case compared to the flat layout. This can be understood recalling that total internal reflection occurs when going from silicon into air already at angles below 17° which leads to a much higher reflection in case of the rough surface of which about half of the surface angles are higher than that limiting angle. The implications of this finding on solar cell simulation using the above algorithm are that errors might be introduced if layer interfaces between materials of high and low refractive index are present, in that order. As the first pass of light can be considered the most important such interfaces occur in single junction layouts only at the backside of the solar cell, where a high quality reflector is present anyway. One therefore can expect that this setting is unproblematic. In tandem cells the situation is different at the intermediate reflector after which a second absorber block follows. The simulation layout studied in this section models the very pessimistic case of a low index dielectric back side material.

Even though the simulator *SunShine* which was developed at the University of Ljubljana

[Krč+03] was available to the author a Matlab based variant of the described algorithm was implemented. The purpose of this was to not further modify the rigorously computed power transfer matrices by interpolation or renormalization. The scalar scattering models in *SunShine* did not allow this data to be passed without further assumptions, even though these probably would not have a large impact. For building the scattering transfer systems a sufficiently large sample of 10 μm wide periodic interface representations was simulated rigorously for specular incidence in air and for incidence on the 1D grid of Fourier modes with Bloch vector 0 and a non–zero real part of the wave–vector in vertical direction in silicon. For all sources reflection and transmission matrices were built including all modes with vertical propagation. Only the real part of the silicon refractive index was taken into account in this computation but low wavelength results presented in Fig. 3.27 suggest this is a valid assumption for the complete wavelength range. This procedure was repeated at every wavelength.

Rigorous results of the three–layer layout air / silicon / air with the same roughness profile on both interfaces and nonzero absorption coefficient in silicon where further computed for various vertical interface distances between 0.05 μm . . . 3 μm.

Results

For the approximate simulation a decision had to be made on how the incoming power flux was distributed into the two systems. As the separation is artificial no rigorous criterion is available for this. One choice consisted in using the remaining initial specular reflection, transmission and absorption after two inner reflections of the ray tracing system. Contributions to the specular channel from secondary scattering where consequently ignored. The energy splitting hardly changes when more reflections are considered. This choice was labeled *"implementation 2"* in the graphs of Fig. 3.27. A large contribution to the coherent channel in the described splitting is due to the primary reflection on the air/silicon interface. For testing purposes this contribution was not added to the coherent but to the incoherent channel and labeled *"implementation 1"*. As a third choice a completely incoherent ray tracing with scattering interfaces was added to the analysis and marked *"incoh. ray tracing"*. The flat coherent system was included in the spectrally resolved diagrams as a second reference for interference positions besides the rigorous solution of the interface textured layout.

A comparison of the spectrally resolved absorptance computed with the described algorithms is shown for two silicon layer thicknesses in the top row diagrams in Fig. 3.27. The examplarily chosen layer thicknesses show the typical offsets found for low layer thickness of a few hundred nanometers or less and high layer thickness of 1 μm and above. Pure ray tracing overestimated the absorptance in all cases. It matched only with the rigorous solution

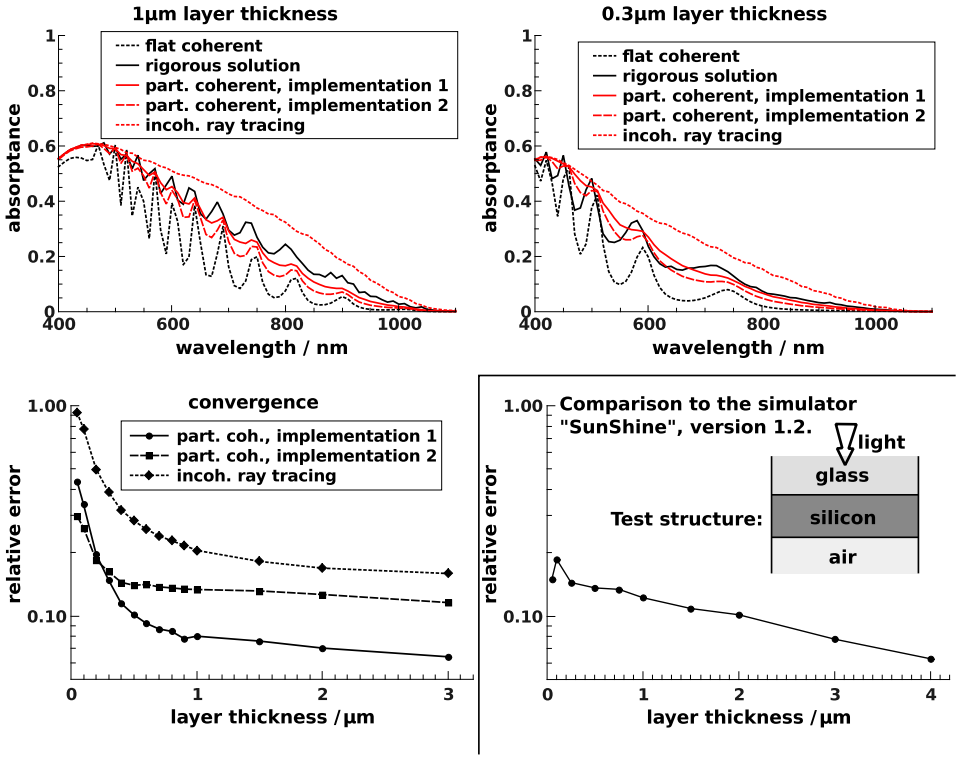

Figure 3.27.: ***Top:*** *Results of rigorous solution, approximate models with two types of coherency splitting and the completely incoherent ray tracing case. Solutions of the flat multilayer system are included for comparison. Details on the two partially coherent implementations can be found in the text of the "Results" section, on page 96.* ***Bottom left:*** *Convergence of the three approximate models against the rigorous solution.* ***Bottom right:*** *Convergence of a test case compared to the simulator SunShine, version 1.2.*

at low wavelengths where almost complete absorption is expected at the first pass of light. As the initial energy transfer at the top interface was computed rigorously and the equal splitting requirement of the coherent and incoherent channels is approximately fulfilled for energy transmission from air to silicon (cf. Fig. 3.26, right) all approximate algorithms performed well in that wavelength range. The partial coherent ray tracing solutions approximated the rigorous solution much better than the incoherent ray tracing but consequently underestimated the absorptance at layer thickness higher than a few hunder nanometers in the long wavelength range. A considerable amount of light is expected to reach the rear interface in that wavelength range for all tested layer thicknesses. The empiric choice labeled *"partially coherent 2"* reproduced the visible interference pattern well at larger layer thickness. The second empirically chosen energy splitting labeled *"partially coherent 1"* with less energy attributed to the coherent channel approximated the absorptance of the rigorous solution better at high

layer thickness but reduced the visibility of interference patterns considerably. Both partially coherent models underestimated the amplitude of the interference fringes in case of small layer thickness. Most significantly in the graphs for 0.3 μm but also for 1 μm layer thickness the positions of the interference pattern of the flat layout and the rigorously computed rough layout do not match. Hence the flat layout is not an ideal choice to approximate the interference pattern.

The relative integral error of all three approximate algorithms against the rigorous solution was computed using trapezoidal integration over the wavelength range. Results are depicted in Fig. 3.27, bottom left. The convergence of all algorithms with increasing layer thickness was found to be rapid up to about 0.5 μm layer thickness and considerably slower above. That shape of the convergence curves could be strongly determined by the absorptance properties of silicon and hence the normalization integral. Purely incoherent ray tracing showed an error of still 20% at a silicon layer thickness of 1.5 μm. The intuitive splitting of incoming power *"partially coherent 2"* provided the best approximation already at low layer thickness but converged only to about 14% deviation at 400 nm layer thickness . The non–intuitive partitioning *"partially coherent 1"* lead to a better approximation of about 7% at 1 μm layer thickness.

A similar convergence study was done using the simulator *SunShine* instead of the matlab implementation. The version of SunShine *SunShine* provided by the University of Ljubljana did not allow to completely stay within the diffraction intensities obtained by rigorous simulation. Part of the scattering model used assumptions from scalar scattering theory to evaluate angular distribution of light when scattering at interfaces. The layer structure used for this comparison is depicted in the inset of Fig. 3.27, bottom right. It differs somewhat from the layout discussed above, as the light is incident from a glass half space, not from air. *SunShine* also provides a switch triggering completely coherent simulation for very thin layers. For the simulations presented here this switch had been activated for layers thinner than 100 nm. Apart from the low thickness region where *SunShine* performed better the convergence to a rigorous solution was found to be comparable to the results obtained with the Matlab implementation.

Conclusion

The monitored convergence against the rigorous solution in case of the test layout, which lacks a back reflector, is clearly not sufficient at the typical layer thickness of silicon solar cells. Literature comparisons to experimental EQE data suggest that the semi–coherent ray tracing method performs well in presence of a back reflector. The simulation results included here suggest that care should be taken in application of the empirical algorithm if layers of low

refractive index follow layers of high refractive index in the solar cell layout, as for example in case of intermediate reflectors. An extension of this analysis to layouts including a back reflector and optionally an intermediate reflector are planned for future work.

3.7. Summary

The synthesization of rough surfaces from height autocorrelation data presented in section 3.2 yielded good results for modeling of FTO surfaces but did not perform well in case of etched ZnO:Al surfaces. It can therefore not be regarded as a generally applicable method and requires an individual characterization for each TCO type. The results for the etched ZnO:Al surfaces suggest that the method might also not perform well for other TCO surface morphologies with strong fabrication fingerprints, such as LPCVD deposited ZnO:Al surfaces, which consist of randomly grown triangular pyramids. Placing characteristic shapes at random positions according to density and to a size distributions extracted from AFM data might be the method of choice to synthesize these characteristic ZnO:Al surface morphologies. This was recently also suggested by Agrawal [AF11].

The main result of the simulations presented in this chapter was a quantification of possible model errors. The most important requirement on the surface synthesization method was to yield statistically identical surfaces over a wide range of domain sizes. The ACF based synthesization approach was found to maintain the surface statistics to a high degree also for very small domain widths. The automatic periodicity of the surface tiles and smooth continuation over the domain edges provides a further advantage for characterization purposes as compared to mirrored surface cuts from large aperiodic surfaces.

The detailed characterization of the Monte Carlo averaging and the boundary influences for 1D rough surfaces, in section 3.4, showed that low relative errors are hard to obtain for wavelengths above 900 nm. A few tenths of geometry representations of over 100 μm domain width had to be averaged to reach 1% relative error at these wavelengths. The large domain width was seen to be a requirement of the errors introduced by the artifial lateral domain boundaries, which do not approximate well the experimental case of an extended rough interface. For efficiency prediction in photovoltaic application absolute errors on the absorptance scale are more important than relative errors. On that scale errors smaller than 1% of the incoming power could be assured already for a few geometry samples of moderate size. Periodic boundary conditions are preferential for small domain widths as compared to isolated boundary conditions in the radius of influence analysis.

The Monte Carlo sampling required for simulation of solar cells with 2D rough surfaces yielded comparable standard deviations of the absorptance as in case of the lowest domain size tested for the 1D rough surfaces. Domain size limitations in 3D simulations indicate that small relative errors can not be reached in simulation of 2D rough surfaces. Generally it can be assumed that domain boundary induced errors converge faster with increasing domain size

in case of 2D rough surfaces, where the intensity of trapped light decays as $1/r$ within the layer where it is trapped, with r being the distance to the disturbance and without considering absorption. For 1D rough surfaces the intensity of trapped light does not decay with increasing distance. Without damping through absorption or by escape from the trapping layer the threshold based radius of influence may become infinity in that case. The convergence of the errors induced by domain size limitation with increasing domain size for 1D rough surfaces is therefore a pessimistic estimate for the case of 2D rough surfaces, which is only based on loss mechanisms and not on distance effects. In 2D rough surface simulation, the absorptances in silicon and the front TCO yielded a good comparability already between domain sizes of $1\,\mu$m and $1.5\,\mu$m.

Simulated cells incorporating 2D rough surfaces and 1D rough surface slices were compared in section 3.5.2. Surface slices have an equal height but different angle distribution as compared to 2D rough surfaces. The results yielded a good comparability of the total absorptance and the absorptance in silicon for wavelengths below 600 nm. This can be explained by considering the results for transmission through a low refractive index into a high refractive index medium presented in section 3.6. The total power fraction transmitted through the rough interface should be comparable to the flat layout and most of the light is absorbed before reaching the back reflector in that wavelength region. The height and angle distribution therefore do not have a substantial influence on the absorptance results and the computed values from 1D and 2D roughness are comparable. Above 600 nm wavelength, where light trapping effects become important, the computed silicon absorptances for the 1D and 2D rough surfaces differed considerably. The high absorptance contribution by superstrate light trapping depicted in Fig. 3.23 which was approximated using the incoherent coupling described in section 2.2.3 suggests that this contribution can not be ignored in the prediction of cell the efficiency at wavelengths above 600 nm.

A simple three layer layout, {air or glass}/silicon/air, was chosen for the comparison between rigorous and approximate methods in section 3.6. A notable difference in total reflectance was shown between reflection from the rough and the flat silicon/air interface at normal incidence. As early scattering events make the highest contributions to absorptance, transmittance and reflectance, the reflectorless layout was clearly not a favorable choice in view of the implementation of the approximate solver. The performance of the partially coherent ray tracing system was found to be much better than of the flat layer solution or the purely incoherent ray tracing with far field angular scattering data. In the simulations with the custom solver implementation, deviations of 14% in an integral norm to a rigorous solution were reached at a few hundred nanometer layer thickness. For thinner layers the error in-

creased considerably. Employing the far field scattering distributions is clearly not applicable in case of very thin layers. A special treatment of thin layers, as applied in the simulations with the solver *SunShine*, allowed for a much lower error in that range of layer thicknesses. For layer thicknesses above a few hundred micrometers convergence with increasing layer thickness against the rigorous solution was found to be slow for both solver implementations in the tested case.

3.8. Conclusion

A surface synthesization method was characterized with respect to experimental rough surfaces. The synthesization method was found to be suitable for the generation of typical FTO substrate morphologies. The convergence of a Monte Carlo sampling of small rough surface patches and the artifacts introduced by the artificially chosen lateral domain boundaries were studied for 1D and 2D rough interfaces. The detailed analysis on 1D rough interfaces reveiled that sufficient convergence for experimental comparison could be reached for sampling over less than 20 surface realizations at a very small domain width. Periodic boundary conditions were found to be a better choice than isolated boundary conditions in combination with buffer regions for representing the experimental case of an extended rough surface. At high wavelengths, domain sizes of up to a several ten micrometers were necessary for sufficient convergence of the sample average absorptance to the case of extended 1D rough interfaces.

A comparison of three domain sizes for cells with 2D rough interfaces revealed simulation artifacts introduced by the limited simulation domain size and laterally applied periodic boundary conditions. However, a good comparability of silicon absorptance was reached already for domain widths of $1\,\mu$m and $1.5\,\mu$m. The required Monte Carlo sample size was found to be comparable to the sample sizes required for 1D rough surfaces.

Simulations of single junction thin film silicon solar cells with 1D and 2D rough interfaces yielded comparable results in the low wavelength region where silicon has a high absorption coefficient. However, in the spectral region above 600 nm wavelength, where light trapping effects become important, the silicon absorptance was seen to be significantly higher in case of the 2D rough surface. Hence, 3D simulations seem to be necessary in that wavelength range for a correct prediction of cell efficiencies.

Using the characterized rigorous simulation of 1D rough surfaces, the performance of an approximate statistical ray tracing solver with an optionally coupled coherent transfer system was evaluated. The performance of a partially coherent approximate solver was found to be much better than of a purely incoherent ray tracing system. However, no satisfying low error

level could be reached at typical layer thicknesses of solar cells. The bad convergence against the rigorous solution is attributed mostly to the lack of a back reflector in the tested layout.

Many results reported in literature have shown that the semi–empirical statistical ray tracing methods can give a good insight into the multilayer optics of absorbing systems with rough interfaces. The availability of good approximations to angular resolved scattering between arbitrary materials through computationally inexpensive models makes them applicable from surface topography and refractive index measurements only. But the comparison done within this thesis suggest that a characterization needs to be made for the studied layer system and that care has to be taken in the evaluation of results from these methods for reflectorless layouts or if intermediate reflectors are present. A special treatment of very thin layers, as implemented in *SunShine*, is regarded as necessary.

4. Periodic scatterers for light management in thin film silicon solar cells

This chapter presents optical simulations of the novel periodic light management textures developed at Helmholtz–Zentrum Berlin. The chapter begins with a summary of prior work on light trapping in periodic geometries, available patterning methods suitable for photovoltaic device manufacturing and a discussion of the possible advantages of periodic texturing in section 4.1. In section 4.2 the contribution of this thesis is presented in detail. Simulations of periodic light trapping textures were done along with an experimental realization of one of the simulated textures. Section 4.2.2 presents the experimentally realized texture and its geometrical reconstruction. A verification of the optical simulation of the reconstructed model with an absorptance measurement can be found in section 4.2.5. The experimentally realized textures were scaled and tested with various back reflector concepts in the simulations to find an optimal light trapping layout. The results of these variations are presented in sections 4.2.6, 4.2.7 and 4.2.8. They suggest that the experimentally realized texture in combination with a flat back reflector or possibly a detached back reflector layout could allow a light trapping for polycrystalline thin film absorbers, which is beyond the level achieved in microcrystalline thin film silicon solar cells with etched AZO random textures. The chapter concludes with a discussion of the performed simulations.

4.1. Introduction

4.1.1. Prior work

Periodic scatterers for light management in solar cells have been a topic of research already for geometrical light trapping in wafer cells for over twenty years. Campbell and Green studied the influence of V–groove textures as well as regular and shifted pyramidal grids on cell

absorption by ray tracing analysis [CG87]. They concluded that substrates with an optimized regular patterning on the front and back side could outreach the efficiency gain of a lambertian randomizing front surface for a wide range of incident angles. Other groups extended the ray tracing analysis for wafer cells, e.g. by considering hexagonal grids and varying unit cell textures [HZW10]. Sizes of the textures considered for wafer cells range typically from ten to a few ten microns. The thickness of wafer cells of about 200 μm allows for such texture sizes for which ray tracing analysis compares very well to experimental results [YUF06; HZW10].

Identical textures as used for wafer cells were subsequently also proposed for implementation in thin film solar cells using a conformal growth of the thin film structure on the regular light trapping super–pattern. Thorp [TCW96] simulated V–shaped grooves, reaching cell currents close to idealized lambertian light trapping for thin film silicon solar cells with 10 μm effective thickness when using asymmetric gratings and tapered films. However such film geometries would be very difficult to fabricate. Generally conformal thin film textures deposited on large surface currogations benefit almost exclusively from multiple geometrical passes through the cell as the possibility for light to be trapped at angles below the escape cone within the active layer is very low. Such kind of trapping is achieved with the micrometer scale random texture presented in the previous chapter of this thesis. However, even experimentally optimized random textures do not perform as well for thin film silicon solar cells as predicted by the geometrical limits. Instead of the predicted light path length improvement factors of almost 50 at the band edge of silicon, LPIF values of less than 20 have been determined for microcrystalline thin film silicon solar cells [Ber+06]. Thorp [TCW96] suggested a combination of a periodic super–texture with lambertian light trapping, which according to his estimations would yield a good light trapping performance also for non–ideal lambertian light trapping.

In recent years most approaches to light trapping improvement in thin film solar cells are based on diffraction into guided modes of the thin film device. This requires a planar device layout with small surface currogations of the interfaces which make the coupling of incident light into guided modes possible. Sub–micron scale periodic patterns have shown to be a good competitor to random surface texturing for this purpose [HS07]. Generally, periodic interface patterns can always be regarded as a diffraction grating, scattering into a discrete set of modes of the absorber bulk. The unit cell shape determines the modal structure of guided modes and the scattering potential into each mode. Recently, Yu developed a theory predicting wave–optical limits for light trapping based on a statistical energy distribution into the modal structure of a uniform absorber layer [YRF10a; YRF10b]. In his papers he proposed 1D and 2D grating layouts with band–edge absorptions beyond the geometrical limits. His

propositions were not based on actual solar cell structures as no low index front layer was present. Haug et al. [Hau+11] experimentally verified the excitation of guided modes in grating structures. They further provided a more conservative estimate of limiting efficiency for thin film solar cells with TCO layers of non–negligible thickness and absorption, $4(n_{\mathrm{Si}}^2 - n_{\mathrm{TCO}}^2)$, which evaluates to less than 40 at the band edge of silicon.

Periodic textures have further been proposed and implemented as dielectric back reflectors [Ber+07b; Zen+08] and photonic crystal intermediate reflectors for stacked multi–junction layouts [Bie+08; Bie+09] and anti–reflection coatings [Tse+11].

4.1.2. Deterministic surface nano–patterning techniques in photovoltaic research

Due to the strong economic constraints imposed in thin film solar cell production not many of the proposed periodic designs were brought to application until now. Elaborated patterning techniques like optical lithography or writing with focused particle beams have processing times and costs which are far beyond the requirements to be fulfilled for inclusion into production lines. In recent years, nano–patterning methods capable of creating both, random and periodic surface textures, have been brought to industrial application and are now a subject of research also for photovoltaic application. Simple, economic and scalable patterning techniques include colloidal lithography [OY01; ISA08; Nun+10; Wan+09] and nano–imprint lithography [Guo04; Li+03; RV+09; Son+11a]. Colloidal lithography is very easy to apply but limited to shape factors provided by the thus deposited particles, usually spheres in the sub–micron and micron range which assemble to layers with a dense packing structure [ISA08; Nun+10; Wan+09]. Better control of texture shape requires the use of deposition masks [OY01]. The colloids can also be used as a mask for subsequent deposition and etching steps, thus forming e.g. spherical voids or U–shaped craters which may have application as selective photonic crystal reflector [Ber+07b; Bie+08; Bie+09], scattering interface [Zhu+08] or ARC [Tse+11]. Other methods of self–assembly suitable for photovoltaics work with self–ordered metallic structures which can be implemented as back reflector layer [Sai+08; SK09] or used as deposition masks [She+11a]. Further columnar material growth is gaining popularity in thin film solar cell design as it provides a combination of properties of electrically very thin devices with optically sufficiently thick devices [GY10; KAL05; Kel+10; Kel+11; Li+09; Siv+09; Van+11]. These methods allow to realize many different surface textures. However, the use of self–assembled systems limits the design parameters to the geometry provided by the characteristic shape and assembly. Fine-grained control is possible through the use of de-

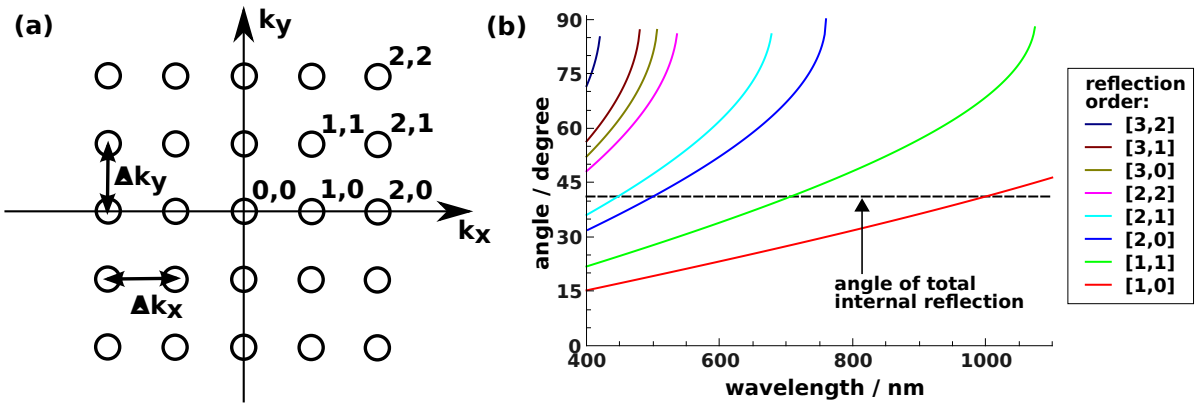

Figure 4.1.: ***(a)*** *k-space grid of discrete Fourier modes. The dependent third dimension has been omitted.* ***(b)*** *Propagation angles of various modes in the glass superstrate of a cell patterned with* $1\,\mu m$ *square periodic texture.*

position masks which reduces the assembly to the replication of a master, thus cancelling the benefit of cost efficient self–assembly.

In contrast to colloidal lithography nano–imprint methods are completely replica–based. A reuseable negative stamp is impressed into a soft substrate which is subsequently hardened. This lithographic technique allows creation of high–aspect textures with high aspect ratios [Guo04; Li+03]. Feature sizes as small as a few hundred nanometers can be imprinted on larger areas than with optical lithography and at a considerably lower cost. Large–area imprints are currently readily available on plastic substrates and have already been implemented in a–Si/μc–Si solar cells using low temperature deposition techniques [Söd09; Söd+10]. The use of solgel–based imprinting on rigid substrates as glass has been suggested for production of light management textures already a while ago by Brendel [Bre+97]. Currently, the solgel imprint method is being transferred to large–area coating of glass substrates. Modern solgels also survive the deposition and crystallization steps involved in the fabrication of thin film silicon solar cells. The properties of silicon deposition and crystallization to polycrystalline material on solgel textures have been studied by Sontheimer et al. [Son+09; Son+10; Son+11b; Son11; Son+11a]. The use of solgel based replicas for random and periodic texturing of thin film solar cell substrates was also reported by other groups [Hei+08; Wei+10; Bat+11a; Bat+11b; RV+09].

4.1.3. Advantages of periodic scatterers for light management

The discrete modal structure can generally be seen as the advantage of periodic textures over random textures as it allows a tayloring of light trapping properties to specific wavelength

regions. Often the same argument is used to promote random textures as beneficial in comparison to periodic textures as they provide good light trapping properties over a large wavelength range and for all incident angles. Practically and especially for polycrystalline thin film silicon solar cells, which can be deposited a few microns thick without substantial electrical losses, the wavelength range where efficient light trapping is needed is only about half of the complete absorption spectrum. Already moderate path length enhancement leads to good absorption characteristics below 750 nm wavelength, e.g. in [Ber+06]. Agrawal [AP09] showed that a combination of scattering elements and planar waveguides of different effective refractive index could lead to a very good light trapping in amorphous silicon cells.

Additionally to the single–pass light trapping properties of the texture an optimal choice of the texture period can lead to additional light trapping by total internal reflection at planar interfaces, e.g. the superstrate–air interface. From the horizontal wave vector component

$$k_{\parallel}(m_x, m_y) = \frac{2\pi}{L}\sqrt{m_x^2 + m_y^2}\,, \tag{4.1}$$

where m_x, m_y are the indices of the diffraction order as shown in the left diagram in Fig. 4.1 and L is the unit cell pitch, the angle of propagation of a periodic field with zero Bloch vector in a material with refractive index n is defined by

$$\theta(m_x, m_y) = \arcsin\left(\frac{k_{\parallel}}{k_0 n}\right). \tag{4.2}$$

Here k_0 is the norm of the vacuum wave vector. The limit wavelength for total internal reflection at the interface to a material of refractive index n of a diffraction order for a square periodic grid is given by $k_{\parallel} = k_0 n$ which yields

$$\lambda(m_x, m_y) = \frac{Ln}{\sqrt{m_x^2 + m_y^2}}\,. \tag{4.3}$$

Fig. 4.1, right, shows the propagation angles of various discrete diffraction orders of normally incident light inside the glass superstrate for a texture period of $1\,\mu$m. The angle of total internal reflection was included in the diagram as a horizontal line. A beneficial effect of total internal reflection to light trapping has already been seen as an artifact in the 3D simulations of rough surfaces in the previous chapter (p. 86) for the 750 nm periodic cell layout. This gain by multiple passes through the solar cell had a sufficient band width to cover most of the spectral region where light trapping is important. Possible gains by internal reflection are studied for a specific periodic texture in a later section (4.2.7) of this chapter. Random textures do not

easily allow such kind of spectral tuning.

Optimizations of 1D and 2D grating textures have been performed by many groups already [CK+09; Wei+10; Zen+08; HS07; Isa+; Pae+11a; She+11b; She+11a]. Most of the designs that were studied for implementation in micro–crystalline and crystalline thin film silicon devices did not exceed the state-of-the-art light trapping provided by a random texturing of the front TCO interface, given e.g. in [Ber+06; LGH04]. Some have very good light trapping properties but were not designed with fabrication and electrical properties in mind, as the one proposed by Agrawal [Agr08; AP09]. For amorphous silicon solar cells a recent development has been made through the use of substrates with cones on a hexagonal lattice [Zhu+09; Zhu+08; Zhu+10]. Material growth on the substrates did not lead to a shifted replication of the underlying texture but to growth of dome–like silicon surfaces on the pointy cones of the substrate. The solar cells showed very good light trapping properties with no strong dependence on the incident angle.

In case of polycrystalline silicon, which is regarded as the base material for solar cells throughout this thesis, deposition and growth characteristics are further constraints imposed on the optical design. Sontheimer [Son11; Son+11b] showed that for electron–beam evaporated and solid–phase crystallized silicon compact polycrystalline growth was possible on mildly textured substrates only. Strong texturing lead to creation of porous regions after crystallization which results in a considerable degradation of the electrical properties of the cell. A better control of crystal growth was found on periodic substrates with $\frac{\text{height}}{\text{period}}$–ratios of more than 0.5. Still porous and amorphous regions existed as in the case of high–aspect random texturing but their deterministic distribution allowed a removal by selective etching process. The remainder of the etching process was grid of high–quality crystalline material. The process could be scaled to over $4\,\mu$m material thickness on a substrate with a rectangular periodic grid with $2\,\mu$m pitch. The underlying substrate has features which are close to the cones described above, which provided high quality light trapping for amorphous silicon cells. In polycrystalline thin film silicon technology the most important advantage of periodic patterning lies in the combination of a good light trapping texture with high quality material growth characteristics. The optical properties of the textures produced experimentally by Sontheimer were studied by simulation by the author of this thesis and are presented throughout the rest of this chapter.

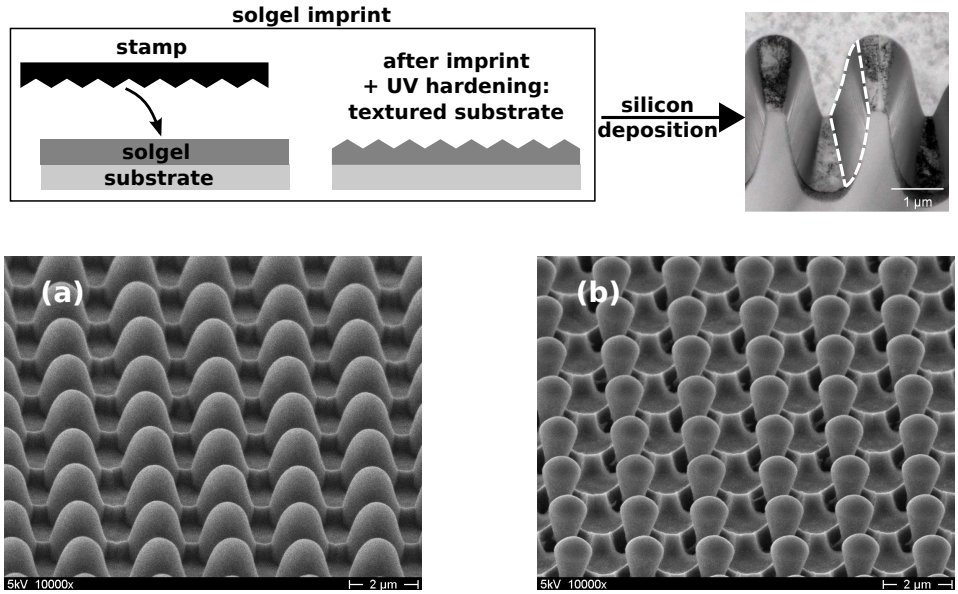

Figure 4.2.: ***Top left:*** *Schematic of a solgel imprint process. A stamp with the negative of the desired texture is pressed into the solgel which is subsequently hardened by UV exposure.* ***Top right:*** *TEM of a 1.4 µm thick silicon layer deposited on a textured solgel and crystallized by SPC. The material at the flanks which is highlighted remains amorphous to a high degree whereas the other regions where transformed into crystal grains.* ***Bottom:*** *SEM view of the deposited silicon before and after selective etching of amorphous parts.*

4.2. Nanodomes – a realistic texture for light trapping created by a nano–imprint technique

4.2.1. Experimental fabrication and characteristics of silicon dome structures on solgel substrates

Nano–imprint lithography textures are created by a stamping procedure. The top left schematic in Fig. 4.2 depicts the solgel based imprint process. After deformation of the solgel surface by the stamp the solgel is hardened by UV light. Then the stamp is removed from the textured solgel. The cross–sectional TEM image on the top right of Fig. 4.2 demonstrates for a 2 μm square periodic texture that substrate textures with high aspect ratios can be produced using this technique. On top of the solgel, which is colored light gray in the image, an amorphous silicon film, colored in darker gray, was deposited by electron beam evaporation and then crystallized by SPC. The resulting material featured crystallites on top of the conical substrate texture and a grid of high qualitity polycrystalline material in the valleys. Only at the flanks of the texture a columnar growth of amorphous material was found, marked by a white border in

the TEM image. In a selective etching step following the crystallization these amorphous parts were entirely removed without destruction of the crystalline parts. The remaining crystalline texture consists of a silicon grid and isolated cone–shaped crystals on the tips of the solgel substrate. Details of the fabrication process and of the material characterization can be found in Tobias Sontheimer's thesis [Son11] and corresponding papers [Son+11a; Son+11b].

4.2.2. 3D reconstruction of the periodic unit cell from TEM images

Due to the high aspect ratio of the solgel and silicon surfaces a direct measurement of the 3D textures by AFM was not possible. The similarity of the grating unit cell to the function $z(x, y) = \cos^2(x) + \cos^2(y)$ suggested a scaling of this function with radial power functions to fit the shape to the experimental geometry. Unfortunately, the actual geometry was deviating too much from this model function and no satisfactory results could be obtained by scaling. Therefore a more general approach for 3D geometry reconstruction was developed based on experimental TEM data.

Reconstruction procedure

The best available data was a cross–sectional TEM image of the $2\,\mu$m periodic solgel substrate with a nominally $1.94\,\mu$m thick silicon layer showing a cut plane through many unit cells. A small sector of the TEM image is depicted in Fig. 4.3, (a), and marked as "vertical TEM cut". The schematic on the left side of the Figure visualizes the reconstruction procedure applied for 3D geometry reconstruction from the cross–sectional TEM data:
Imperfect alignment of the sample lead to a cut direction not collinear to the grid vectors as visualized by the red line in the SEM top view marked "top view". The TEM image was more than $100\,\mu$m large and contained a few sweeps through the complete unit cell. Over about half of the image spline curves were traced manually to the solgel and silicon interfaces, visible as pink and yellow lines in the TEM sector depicted in Fig. 4.3, (a). The obtained curves were polygonalized and mapped to a quarter of the unit cell using an inital guess for the propagation angle α of the TEM cut. The propagation angle was subsequently fitted to about 2.38°. The resulting surface morphologies of the reconstruction process are depicted in the bottom left box of Fig. 4.3.

Adaption of the model to different silicon heights

Silicon growth using electron beam evaporation as deposition method was found not to be strictly in normal direction. Hence surface morphology of the silicon top surface changes

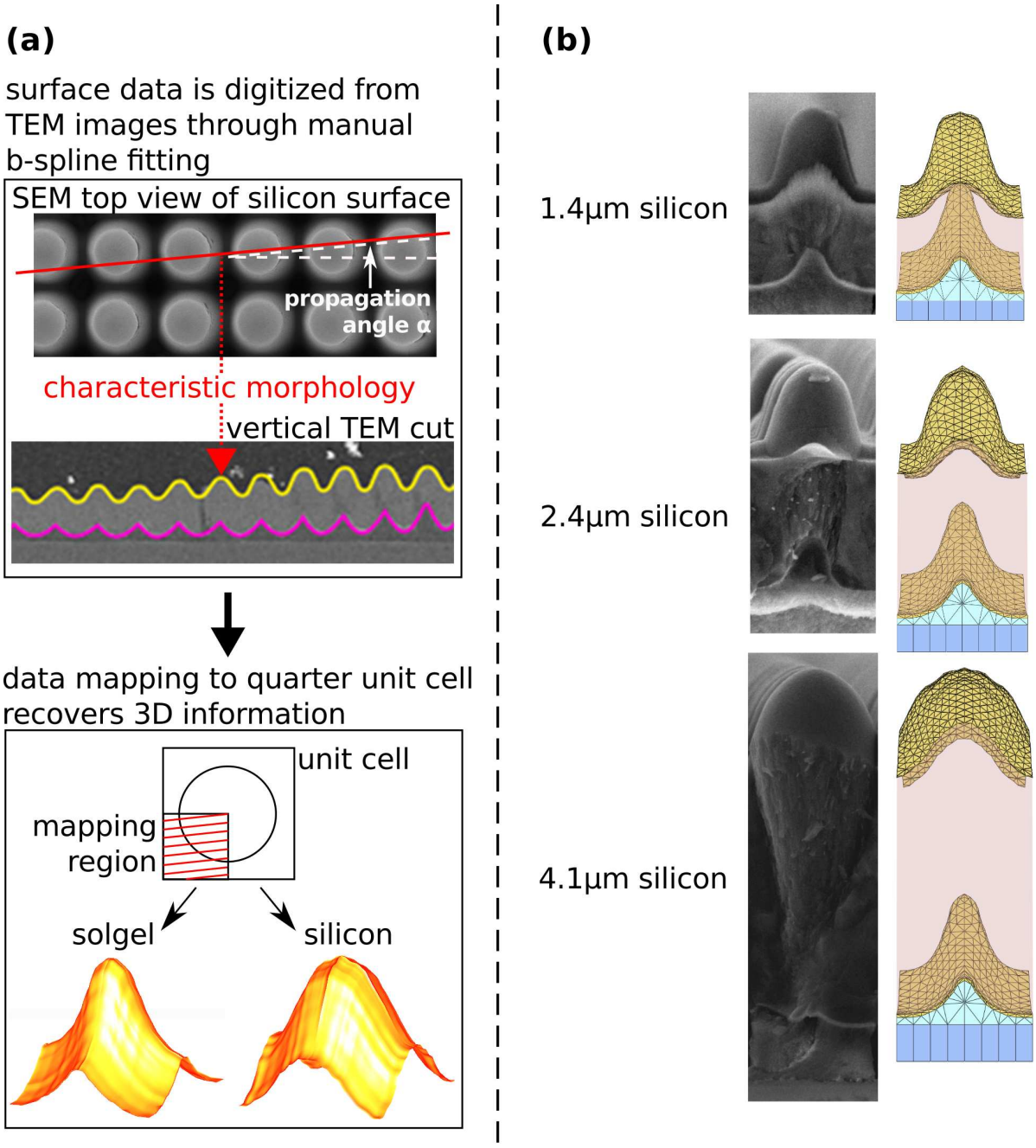

Figure 4.3.: ***(a)*** *Schematic of the 3D recovery process of the unit cell texture from a cross–sectional TEM image. Nominal silicon height was 1.94 µm. Only a small part of the TEM image used for reconstruction is shown here. Details about the reconstruction are given in the text.* ***(b)*** *Reconstructed unit cells for different silicon deposition heights. The shape of the reconstructed silicon surfaces shown in (a) was adapted to the cross–sectional SEM images shown side by side with the computational models. Bottom and top surface of the silicon layer are visualized in yellow. The actual silicon volume was removed for interface visualization and is schematically superimposed as an area shaded in light red.*

with layer thickness. No reconstruction based on the procedure described above was done to obtain 3D models of these surfaces. Instead cross–sectional SEM images were used to define a radial shifting function mapping from the cross–section of the reconstructed surface at 1.94 μm nominal silicon height to the surfaces at 1.4 μm, 2.4 μm and 4.1 μm nominal height. The obtained shifting functions were linearly extrapolated to higher radii and applied to the reconstructed 3D data set. The resulting geometric models are shown on the right side of Fig. 4.3 in a side–by–side comparison to the SEM image used as data source. A small correction was also applied to the reconstructed solgel surface from the comparison to the images of the etched texture depicted in Fig. 4.4 as flanks had been found to be steeper than in the original reconstruction.

The volume between lower and upper curved surfaces in the geometric models have been adjusted to the nominal heights measured on untextured reference samples. Evaporation is a physical deposition method, thus the amount of material deposited on a surface per unit area should not be strongly dependent on the morphology. As the models with known silicon volumes compare well with the SEM images this can be assumed as justified.

Modeling of the selective etching process

Etching of the amorphous silicon parts at the flanks of the solgel peaks created a circular groove around the peak with bounding silicon surfaces that were found to be close to a conical shape. A cross–sectional SEM image of the result of etching a sample with 2.4 μm nominal silicon thickness is depicted in Fig. 4.4. The inner and outer conical surface have approximately the same opening angle θ. From an average over a few cones of a SEM image this angle was found to be approximately 20° with only very small deviations. The horizontal radial distance between inner and outer surface was measured as approximately 0.34 μm. In the geometrical model conical surfaces were used to represent the material interfaces created by the etching process.

4.2.3. Cell layout and material parameters

For the solar cell simulations in this chapter a model device structure very similar to the one for rough surfaces described in section 3.3.1 of the previous chapter was used. The solar cells where assumed to be illuminated through their glass superstrate. As no exact set of material data was available for the solgel it was assumed to be non–absorptive with the same refractive index as glass. A vertical surface shift was used to create a front TCO layer which had a vertical thickness of 300 nm unless indicated otherwise. The layer can be seen in Fig. 4.4

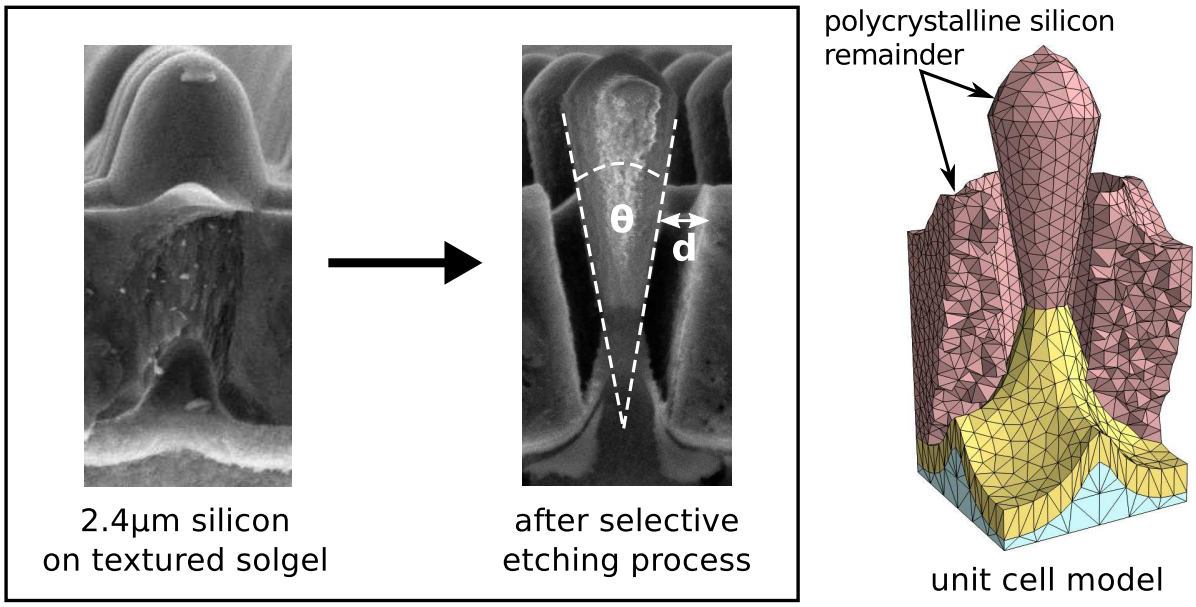

Figure 4.4.: ***Left:*** *Cross–sectional SEM image of the 2.4 µm thick silicon layer before and after the etching process. The cone opening angle was evaluated to $\theta \approx 20°$. The distance between the inner and outer conical surfaces delimiting the amorphous material region has been measured as $d \approx 0.34\,\mu m$.* ***Right:*** *Computational model of the unit cell with conical etchings.*

in yellow below the silicon absorber, colored light red. In simulations of etched structures the conical cuts into the silicon were assumed to be filled with air[1]. At the back side of the silicon absorber different reflector layouts are used throughout this section. In case of the conformal ZnO:Al / silver reflector a local surface normal growth direction of the ZnO:Al layer was assumed to avoid very thin layer thickness at steep flanks. The normal thickness was assumed to be 85 nm. Material parameters of the different materials as used for the simulations are given in appendix A.

4.2.4. Numerical convergence

Numerical convergence was tested for a complete solar cell layout. The reconstructed etched silicon absorber of 2.4 μm nominal height before etching, depicted in Fig. 4.4, was therefore completed with a conformal ZnO:Al / silver back reflector. The cross–sectional view of the computational domain is shown along with the convergence diagrams in Fig. 4.5. A plane wave normally incident from the glass half space was used as the incident field. As in case of the rough surfaces in the previous chapter both the relative error and the absolute error of the

[1] When building an actual PV device of these etched textures a filling of these gaps with material might be required.

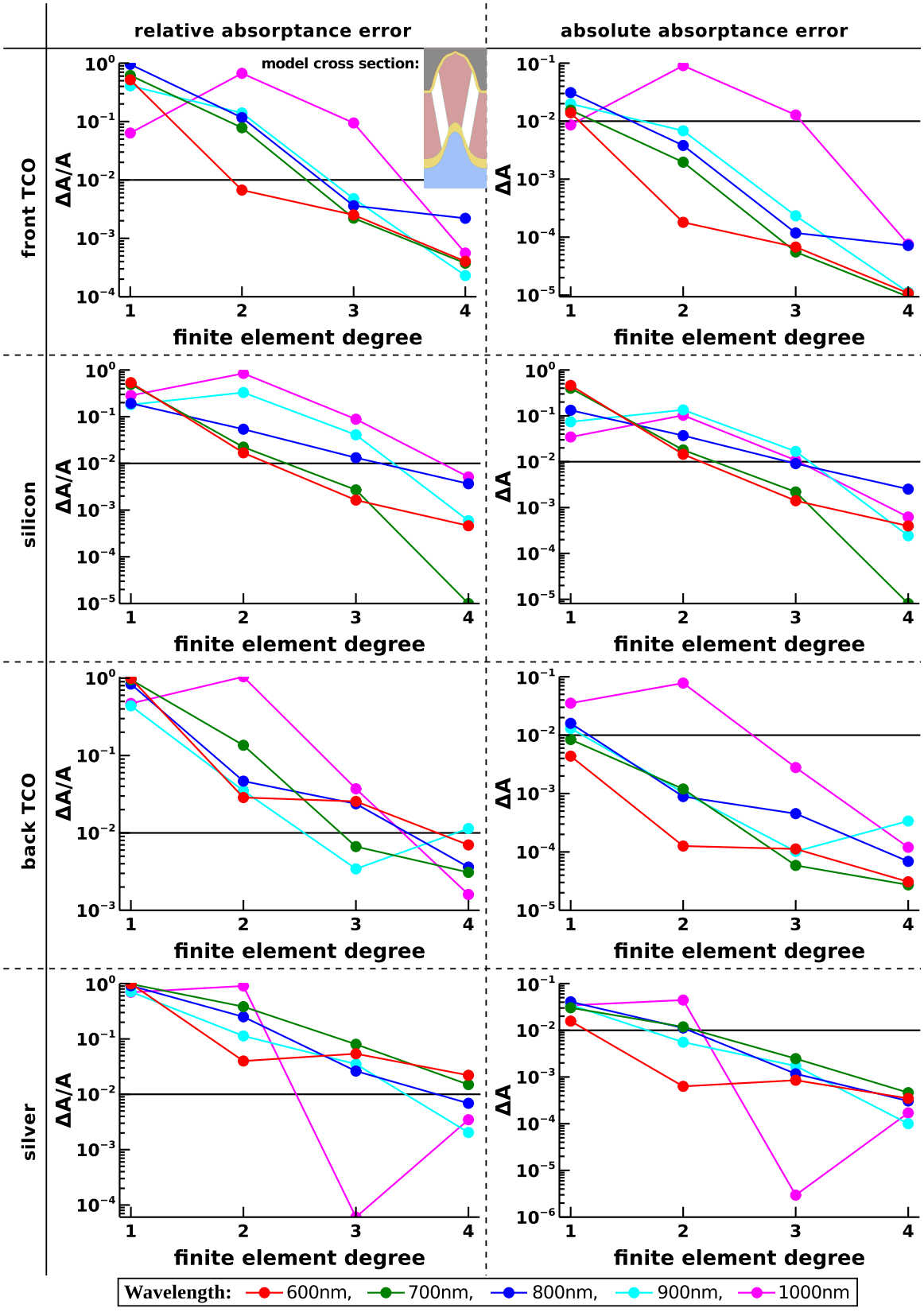

Figure 4.5.: *Relative and absolute absorptance error are plotted versus the finite element degree for the absorptive layers in the device. The discretization of the computational domain was kept fixed at every wavelength. Solutions of one order higher than the highest displayed order were used as reference solutions. See p. 26 for expectations on finite element convergence behaviour.*

computed absorptance in the different material regions were monitored to obtain the computational settings for the following simulations. For evaluation of the results and experimental comparison a high relative precision is not needed in materials with a very low absorptance. Considering the absolute absorptance error for the choice of numerical settings while having the relative error in mind allows for a good trade–off between quality of the solution and computational costs. In case of the dome–like structures with a thin front TCO layer deposited on the textured substrate, absorptance is quite low in all layers except for the silicon absorber. Thus silicon dominates the choice of the finite element degree for most wavelengths. For all following simulations a choice of computational settings was made which satisfied a 1% absorptance error threshold in this error analysis. At wavelengths between 850 nm and 1000 nm 4^{th}–order elements were used to ensure a very good quality of the solution in that wavelength range. Maximum edge lengths in the unstructured grids were enforced by the grid refinement routine of the finite element solver prior to computation.

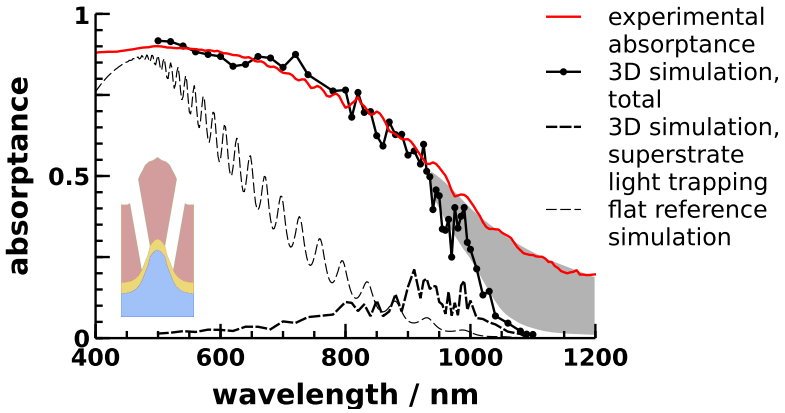

Figure 4.6.: *Comparison of experimental absorptance measurement and simulated absorptance for a nominal silicon height of 2.4 µm deposited on a textured substrate. Measurement and simulation were done for the geometry obtained after etching of amorphous residues. A schematical cross section of the geometrical model is depicted in the inset. A thin layer of ZrO_2 is present between glass (bottom) and silicon (top) domains. Additionally to the 3D simulation, a 1D simulation based on nominal material heights was included for comparison. Details on the marked region between 3D simulation and experimental spectrum are given in the text.*

4.2.5. Experimental verification of the computed absorptance

An experimental absorptance measurement was made available to the author by Tobias Sontheimer. For the measurement an integrating Ulbricht sphere with a reference beam and a sample holder placed inside the sphere was used. In contrast to the reflection–transmission setups often used this setup should produce much smaller artifacts in case of scattering samples, as no light can be scattered out of the entrance cone of the Ulbricht sphere. The absorption measurement was performed on etched samples of 2.4 µm nominal silicon height and no back reflector, as depicted in Fig. 4.4. An intermediate layer of about 70 nm ZrO_2 was present in between the solgel and the silicon parts of the measured sample. The sample absorptance was measured for light incident through the sample substrate, at a very small inclination of 10° between the substrate normal and the incident beam.

Simulations of a cell model corresponding to the experimental sample were performed for normally incident light. The experimental and computed results are compared in Fig. 4.6. A schematic cross–sectional view of the simulation domain, with enlarged intermediate ZrO_2 layer thickness, is included in the diagram. The full geometrical model of this cross section is depicted in Fig. 4.4. Both the 1D and the 3D simulation included in Fig. 4.6 were performed including multiple reflection between the superstrate / air interface and the solar cell model using the algorithm described in section 2.2.3. The 1D calculation of the flat layout was done

using the nominal material heights computed from the 3D model. The material parameters used for simulation can be found in appendix A.

Correspondence between simulated and measured curves is very good for the wavelength range between 500 nm and 920 nm. Both absorptance curves, from 3D simulation and measurement, lie considerably above the 1D simulation with same material volume. This highlights the strong light trapping achieved by our corrugated silicon surface already by total internal reflection from the back surface, which happens at angles above about 17° at silicon / air interfaces and was the motivation for the detached reflector design studied in section 4.2.8. For wavelengths above 920 nm, the simulated absorptance rapidly converges to zero towards the band edge of crystalline silicon. The experimental absorptance, in contrast, levels off to about 20% at wavelengths above the silicon band edge, resulting in the region of high difference between model and measurement which is marked as a gray area in Fig. 4.6. The same high absorptance in that spectral range was also measured independently using the PDS method [Son11] and therefore is not considered an experimental artifact. This high sub band gap absorptance should not be present for a crystalline silicon absorber and may arise from absorption by defects in the non-optimized experimental polycrystalline absorber material. As defect absorption is not included in our simulation model, a defect free experimental absorber should show a similarly reduced high wavelength absorption as present in the simulation. Comparability of simulation and experiment is therefore not good close to the band edge. However, the very good correspondence in the lower wavelength region, where experimental optical material properties should be close to crystalline silicon, verifies the high quality of our model.

The results of this experimental comparison also highlights the importance of taking the superstrate light trapping into account to be able to accurately predict absorptance for optical systems coupled to a substrate, like solar cells in superstrate configuration.

4.2.6. Incoupling of light into silicon

Using the reconstructed solgel surface morphology depicted in Fig.4.3, bottom left, an analysis of the transmittance through the front layers of the solar cell into a silicon half space[2] was simulated for several variations of the interface texture. The vertical device layout in these simulations consisted of three layers, two infinite half spaces of glass and silicon and an intermediate ZnO:Al layer. Both interfaces of the intermediate layer had the morphology of the reconstructed solgel interface. The vertical layer thickness chosen for the ZnO:Al layer

[2]The word “incoupling” is used in this context to describe the transmittance through the front layers into a silicon half space. This should not be confused with coupling into guided modes.

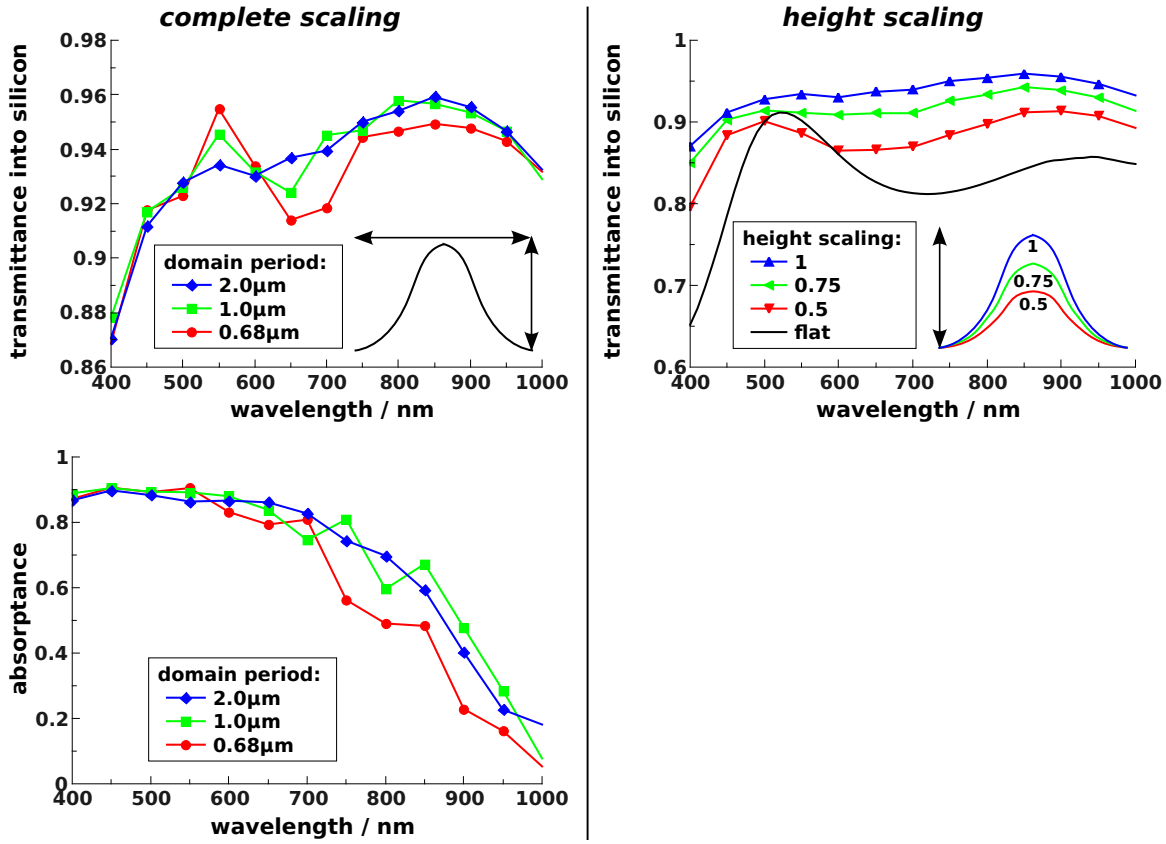

Figure 4.7.: ***Top row:*** *Transmittance from a glass half space into a silicon half space through a textured glass interface and an intermediate 200 nm thick ZnO:Al layer. The solgel interface texture was scaled in all directions (**left**) and only in the vertical direction (**right**).* ***Bottom left:*** *Absorptance of the silicon layer in simulated solar cells with a nominally 2 µm thick silicon layer and a ZnO:Al/silver back reflector, at identical interface texture scalings as in the diagram above. Nominal material heights were kept constant at all scalings.*

was 200 nm. The transmittance into silicon was calculated by evaluating the real part of the normal energy flux through the ZnO:Al/silicon interface, as defined in term III of eq. 2.30. As discussed in the fundamentals chapter (see Fig. 2.6 and corresponding text) the convergence of this surface integral is usually not as good as for the volume integrals. The finite element degree was therefore set to at least one order higher than defined by the 1% thresholds in section 4.2.4.

The transmittance into silicon was evaluated for two different simulation series. In one series the interface was scaled in all directions, thus changing the height distribution but not the angle distribution. In the other series a scale factor was applied in the vertical direction only, changing both the height and the angle distribution. The vertical thickness of the intermediate layer was left unchanged so that the material volume of ZnO:Al per unit area was constant.

The results of the simulations are presented in Fig. 4.7, top row. In case of equal scaling in all three space directions, which is shown in the left diagram, no pronounced changes in the transmittance are observed. Light incoupling into the silicon absorber is very good with values around 94% of the incoming light in glass. The curves for the three tested scalings with unit cell periods of 2 μm, 1 μm and 0.68 μm coincide in most of the tested spectral range. Differences exist in the wavelength range from 500 nm to 700 nm where an interference pattern is visible. This interference gets more pronounced with decreasing unit cell size. Maximum deviations of less than 3% can be found in that wavelength region. In case of exclusive height scaling which alters the angle distribution of the surface a continuous reduction of transmittance towards the transmittance of the flat layout can be monitored for scale factors smaller than one. Transmittance was reduced by about 10% when the surface texture was scaled to about half of the original height. Thus the angle distribution of the unit cell seems to be of much higher importance than the period and the height distribution regarding light incoupling. In case of the considered periodic texture this statement does obviously not hold for light trapping effects as can be seen from Fig. 4.7, bottom left. The solar cell structure considered for this computation consisted of effectively 200 nm of front ZnO:Al, 2000 nm of silicon, 85 nm of back ZnO:Al and a silver reflector. At both interfaces delimiting the front TCO the solgel texture was applied whereas at both interfaces delimiting the back TCO the reconstructed silicon top interface for 1.94 μm nominal silicon height was applied. Nominal material heights were kept constant at all scalings. A plane wave normally incident from a glass half space was used as light source. The silicon absorptance plotted in the diagram does not show pronounced differences at wavelengths below 700 nm. However, at larger wavelengths, where light trapping becomes important, the two samples with larger feature size clearly show a superior light trapping compared to the smallest feature size. In that wavelength range the transmittance into silicon did only show minor differences.

4.2.7. Influence of the texture period on light trapping

The whole experimental fabrication process of imprinting and material deposition is scalable to a high degree, as demonstrated by the TEM image of a 300 nm periodic solgel texture with nominally 270 nm of silicon deposited on top depicted in Fig. 5.1 on page 137. The amorphous material growth emerging from the flanks of the solgel texture as described in section 4.2.2 limits the material height of high quality silicon which can be effectively deposited on the textures. For solar cell optimization it was therefore of interest whether a better light trapping could be achieved at smaller domain pitches with correspondigly lower amounts of absorber material deposited on the substrates. The computational model used for this simulation series

consisted of the solgel with 300 nm of ZnO:Al and nominally 2.4 μm of silicon deposited before the etching process. As for the experimental comparison in section 4.2.5 the etched unit cell layout was used. For this analysis the model depicted in Fig. 4.4 was completed with a back reflector consisting of 85 nm of ZnO:Al grown in the surface normal direction and a silver layer of a minimal thickness of 100 nm. A cross–sectional view of this layout is shown in the center of Fig. 4.8. In the scaling process the whole unit cell was scaled in all dimensions, so that all layer thicknesses decrease accordingly. This assures best conformance with the fabrication process although it may be criticized that no working solar cells can be built from the resulting specifications in case of very small domain periods.

Superstrate light trapping can be optimized to a selectable wavelength region in case of periodic layouts. The first diffraction order in the superstrate just depasses the critical angle for total internal reflection on the superstrate / air interface when the vacuum wavelength equals the texture domain period, as described by eq. 4.3. Over a range of vacuum wavelengths larger than the domain period a second pass through the solar cell is then assured for light reflected into the first diffraction order. In case of normally incident light one would therefore suspect the best choice of the domain period for gains by superstrate light trapping to lie between 700 nm and 900 nm. An example diagram of propagation angles over wavelength is depicted in Fig. 4.1 on page 108 for a domain period of 1 μm.

Simulations for optimization of single pass absorptance of a solar cell using periodic grating textures have already been made by many research groups. One optimal pitch for single pass light trapping under normal incidence which was repeatedly reported in literature lies around 800–900 nm texture period. A second pitch groups frequently reported is around 450–500 nm texture period. Weiss [Wei+10] and Zeng [Zen+08] reported periods of 833 nm and 500 nm respectively for 1D rectangular gratings and crystalline silicon absorbers. Čampa [CK+09] found optimal texture periods of 600–750 nm for sinusoidal 1D gratings with different grating heights and μc–Si single junction cells. His best results stay at a high level also at texture perdiods up to 900 nm. Sheng [She+11b] optimized 1D triangular and saw–tooth shaped grating textures, reporting an optimal period of 900 nm in both cases. Agrawal [AP09] and Isabella [Isa+] reported optimal pitches of 450 nm and 500 nm using different grating textures with material and device stack height parameters of amorphous silicon solar cells. For a 2D periodic pyramidal texture Haase [HS07] reported 850 nm as best texture period. More recently, Paetzold [Pae+11b; Pae+11a] found an optimal texture period of 500 nm for 2D periodic plasmonic reflection grating back contacts in μc–Si thin film solar cells.

In all optimization studies mentioned above the device height structure was kept constant. This is not the case in the scaling analysis presented here. Still the figure of merit for PV

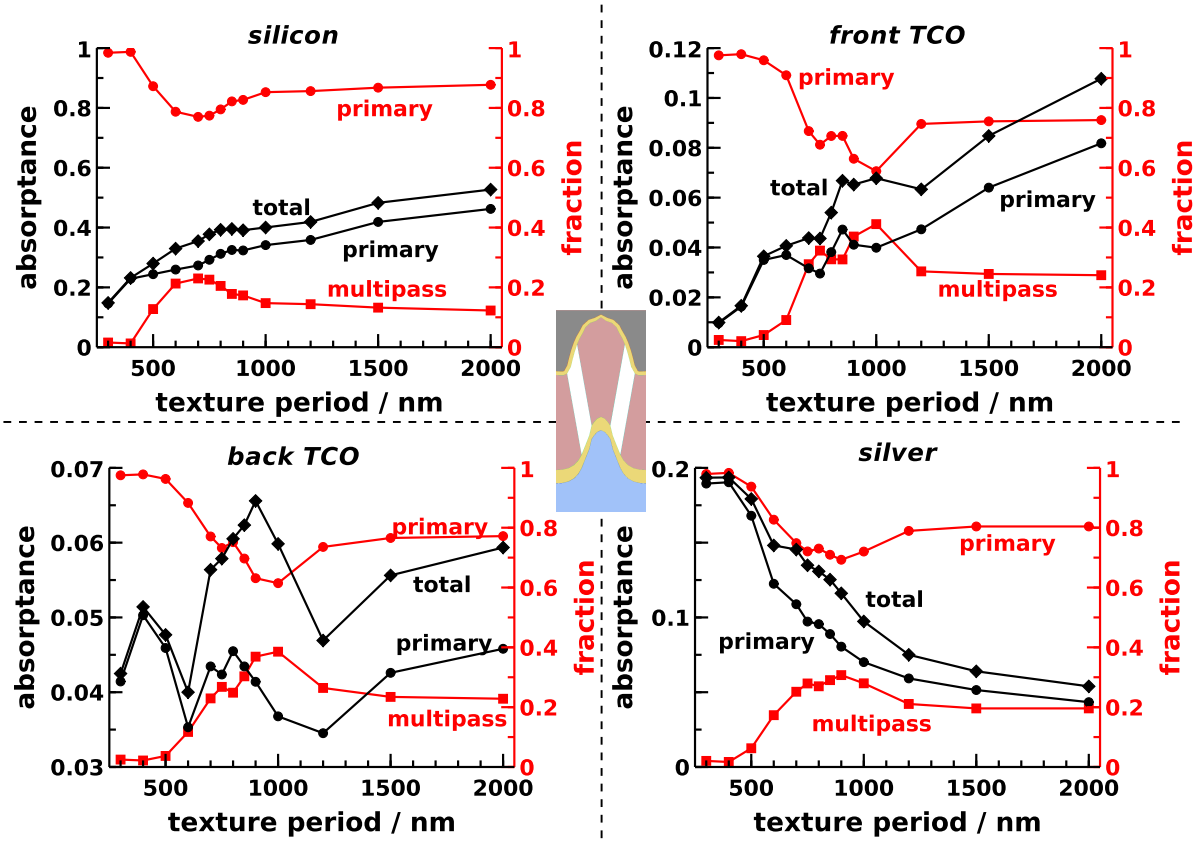

Figure 4.8.: *Average absorptance in the wavelength range between 600 nm and 1100 nm for the solar cell geometry depicted in the center of the diagrams, scaled in all dimensions to various domain periods. Absorptance at the first pass (labeled primary) and due to multiple passes through the solar cell are presented separately to visualize the gain by internal reflection at the superstrate/air interface.*

application is the absorptance of the silicon layer. For that reason the average absorptance

$$\langle A \rangle_{\lambda_{\min},\lambda_{\max}} = \frac{1}{\lambda_{\max} - \lambda_{\min}} \int_{\lambda_{\min}}^{\lambda_{\max}} A(\lambda) d\lambda \tag{4.4}$$

was plotted inf Fig. 4.8 for all scalings without considering the different material volumes. Light path improvement in the various cases will be discussed in the following subsection. The wavelength interval used for trapezoidal integration was $\lambda_{\min} = 600\,\text{nm}$ to $\lambda_{\max} = 1100\,\text{nm}$. For domain periods up to 1000 nm a 10 nm wavelength spacing was used and a 20 nm spacing for larger periods. To discriminate light trapping by reflection in the superstrate from light initially trapped in the textured silicon absorber the normalized fractions from the primary pass and from subsequent passes were included in Fig. 4.8 and are labeled *primary* and *multipass* in the diagrams (red curves). Additionally, the non–normalized primary absorptance and the

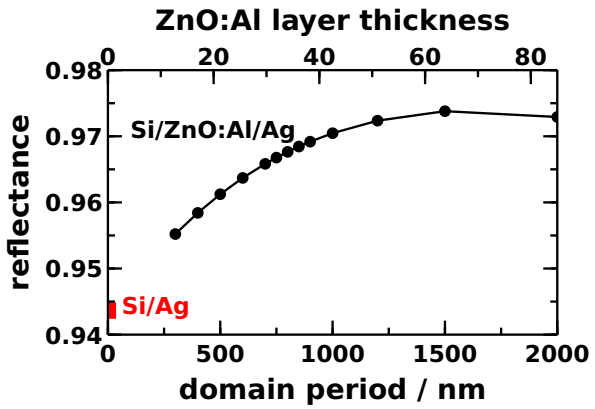

Figure 4.9.: *Reflectance from planar silicon/ZnO:Al/silver stacks at normal incidence for ZnO:Al layer thicknesses corresponding to the domain scalings used in the simulations within this section.*

total computed absorptance (labeled *total*) were included (black curves). All curves were plotted over the texture period which is proportional to the scale factor applied to the nominal geometry defined for a 2000 nm periodic substrate. The corresponding wavelength resolved absorptance spectra of the silicon layer can be found in appendix B.1 for all simulated layouts.

In the diagram for silicon absorptance in Fig. 4.8, upper left, steep slopes are visible below wavelengths of 500 nm and 850 nm. These can be taken as a sign of improved light trapping at these periods. A small local maxiumum is formed in the total absorptance at 850 nm and no significant improvement in absorptance happens until 1000 nm domain period where the nominal silicon thickness is more than 1.6–fold the value at 850 nm. The absorptance gain due to light trapping in the superstrate is largest at periods where only a few propagating orders exist in glass. The gain by multiple passes is very low at periods below 500 nm where all light is reflected specularly over almost the complete wavelength range. It is highest in the range from 700 nm to 800 nm domain perdiod where only a few orders propagate at oblique angles below the escape cone at the superstrate / air interface. The maximum gain by multiple passes is about 20% of the total absorptance in that range of domain periods. For higher periods the gain slowly drops to about 10% of the total absorptance. None of the scaled down geometries reached the silicon absorptance values of the largest tested domain size with the highest silicon volume.

Losses in the front and especially in the back TCO are small at all scalings, ranging from 1% to about 11% of the incoming power flux. In case of the back TCO, absorptance does not scale with material volume. Absorptance is highest at low domain periods. This is probably due to enhanced absorption from localized plasmons at the interface to the neighbouring silver layer, as in case of the silver reflector layer very large absorptance values were found at low domain

periods: Absorptance monotonically drops from about 20% of the incoming power flux to about 5% at the largest domain period. The high absorptance at low domain periods cannot be explained from decreasing reflector quality alone. Fig. 4.9 depicts the reflectance properties of a flat silicon / ZnO:Al / silver stack under normal incidence. The ZnO:Al layer thickness was adjusted corresponding to the domain period in the scaling analysis. Reflector quality of the ZnO:Al / silver stack decreases with decreasing ZnO:Al layer thickness, but only by a few percent. It is probable that the large absorptance values in silver found at low domain periods result from an excitation of localized surface plasmons at the silver interface. Potentially the absorption is further increased due to the decrease in layer thickness of the ZnO:Al spacing layer as discussed by Haug [Hau+08]. Paetzold [Pae+11a] calculated a very similar curve for absorptance in the silver reflector when varying the domain period of a square lattice. His absorptance depasses 20% at 300 nm domain period and decreases to about 10% at 1000 nm domain period.

Light path improvement at the band edge

Light trapping efficiency at different domain periods is measured by computing light path improvement factors. The light path improvement is the path length in nominal absorber thicknesses, calculated by equating the absorptance of the silicon layer to Lambert–Beer absorptance of the light coupled into an infinite silicon half space,

$$A(\lambda) = I(\lambda)(1 - \exp(-\alpha\,\mathrm{LPIF}(\lambda)\,d_{\mathrm{nominal}}))\,. \tag{4.5}$$

Here A is the measured absorptance, I the light coupled through the front layers into an infinite silicon absorber, α the absorption coefficient of silicon and d_{nominal} the nominal silicon layer thickness. Solving for the LPIF yields

$$\mathrm{LPIF}(\lambda) = \frac{-\ln(1 - \frac{A(\lambda)}{I(\lambda)})}{\alpha(\lambda)\,d_{\mathrm{nominal}}}\,. \tag{4.6}$$

Incoupling simulations (cf. section 4.2.6) could not done for this simulation series based on the etched absorber model, but from the results in Fig. 4.7 it has been seen that the transmittance into silicon is almost constant at wavelengths between 600 nm and 1000 nm, over a wide range of domain periods. Therefore a constant incoupling I into silicon was assumed for this analysis. As a conservative choice all light initially transmitted from air into glass was assumed to be transmitted into silicon, to eliminate the effects of a planar anti-reflection system which was not applied to the devices simulated here. The nominal thickness of the etched

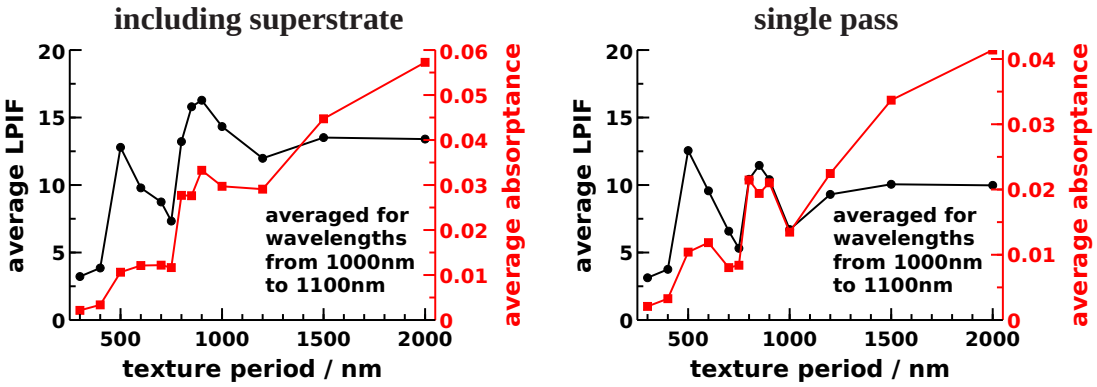

Figure 4.10.: *Conservative approximations of light path improvement factors in silicon using an assumption of perfect incoupling of light into the absorber layer. Average LPIF and absorptance values were computed for wavelengths between 1000 nm and 1100 nm for all domain periods.* ***Left:*** *LPIF and absorptance including superstrate light trapping effects.* ***Right:*** *LPIF and absorptance of the first pass through the solar cell.*

silicon absorber on the substrate with 2000 nm period is $d_{\text{nominal}} = 1.93\,\mu$m. All computed wavelength resolved LPIF spectra can be found in the diagrams in appendix B.1.

High LPIF values as predicted by theory [Yab82; YF11] are expected only at the band edge where the absorption coefficient is sufficiently small. At wavelengths above 1000 nm isolated LPIF values of over 30 were reached for some domain pitches, due to resonances lying in that wavelength range. These resonances make it difficult to compare the different domain scalings. Therefore, average LPIF values were computed for the wavelength range from 1000 nm to 1100 nm. The average high wavelength results were plotted over the domain period in Fig. 4.10 together with the average absorptance in the same wavelength region. The left diagram shows the LPIF values computed for the total light trapping system, including superstrate light trapping. The LPIF values in the right diagram were computed considering only absorption from the first pass through the solar cell. For the considered solar cell texture and structure light trapping close to the band edge is best at domain periods of 500 nm and 900 nm. Including the superstrate light trapping, a maximum wavelength average LPIF value of over 16 was found at 900 nm domain period and over 12 at 500 nm domain period. When excluding the superstrate light trapping, the strongly superstrate depending LPIF maximum at 900 nm shifted to 850 nm and dropped to about 11, while the value for the 500 nm periodic texture remained almost unchanged, as only 0-order reflection exists which lies within the escape cone of the superstrate / air interface. The observed optimal domain periods are consistent with the findings of other groups cited above. The LPIF values computed for most layout variants are smaller than Yablonovitch's geometrical limit [Yab82] of $4n^2 \approx 50$, where n is the real part of

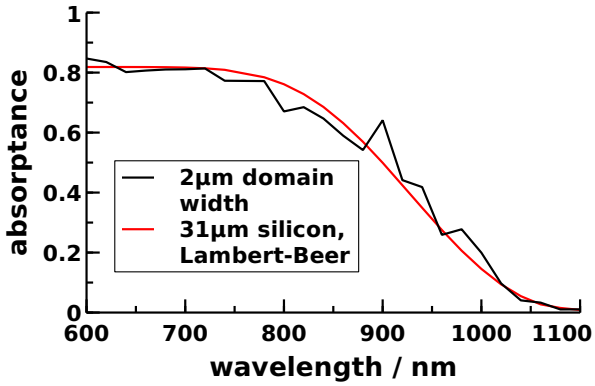

Figure 4.11.: *Absorptance in silicon for the 2 µm periodic layout and absorptance of a silicon layer of 31 µm thickness. The wavelength integrals of both curves are identical.*

the refractive index, and far below Yu's fundamental limit [YF11] of $4\pi n^2 \approx 158$ for uniform layers. The light path enhancement of over 16 for 900 nm domain period is at the maximum light trapping level measured by Berginski in his experimental analysis of microcrystalline cells with etched AZO front TCOs [Ber+06].

Despite of the higher LPIF values at low texture periods the largest value of average absorptance in the high wavelength regime was still reached in the cells with 2000 nm period where light trapping with an LPIF of about 13 is combined with a high silicon volume. A large silicon absorptance at small material volume, desirable for solar cell production, has not been found.

Light path improvement over the whole spectral range

For the layout with 2 µm texture period a silicon layer thickness corresponding to the absorptance over the spectral range from 600 nm to 1100 nm was computed. The result is displayed in Fig. 4.11. The factor I in the Lambert–Beer law eq. 4.5, with LPIF(λ) = 1, was computed as the wavelength average absorptance in silicon of the simulated textured cell in the wavelength range between 600 nm and 700 nm. In this range silicon absorptance is almost constant. The obtained I for the power coupled into the silicon layer was kept constant over the whole wavelength range, which was assumed to be a good estimation from the results of section 4.2.6. The nominally 1.93 µm textured thin film silicon solar cell absorptance corresponds to a 31 µm thick silicon layer in an integral norm over the tested wavelength range. This evaluates to a silicon light path enhancement of about 16, already partially removing the effects of parasitic absorption in other layers of the solar cell. The relatively good correspondence of the previously computed band edge light trapping and large wavelength range evaluation in

this case cannot generally be expected for periodic system and may be an effect of the large period, compared to the tested wavelength ranges.

4.2.8. Influence of the back reflector on light trapping

In this section three different back reflector designs are compared for the 2 μm periodic layout with 2.4 μm silicon deposited before etching. As a reference the solar cell layout without back reflector, already shown in the experimental comparison in section 4.2.5, was also included. The implemented back reflectors layouts are a conformal back reflector, a flat back reflector with a large back TCO volume and a detached flat back reflector without back TCO. The detached reflector design was recently studied by Moulin experimentally, employing etched ZnO:Al surface textures for light trapping [Mou+11; Mou+12]. The conformal back reflector design was already used for the simulations in the previous section. To further assess the losses induced by the silicon etching both etched and unetched versions of each layout were simulated. The results of this study are summarized in Fig. 4.12 and in the tables 4.1 and 4.2. Table 4.1 holds LPIF values close to the band edge and table 4.2 silicon layer thicknesses with integral absorptions equal to the thin film layouts. The computation of these values was done as in section 4.2.7.

The silicon volume reduction by about 20% due to etching results in a decrease of silicon absorptance by 3% to 5% of the incoming power in all cases. The tabulated LPIF values close to the band edge are not very different between the etched and unetched layouts, if a back TCO layer is present. LPIF values are lowest for the cases with a back TCO, when compared to the reflectorless stack and the air spaced flat silver reflector. Light path improvement factors up to 25 were calculated for the configurations without back TCO layer. In the back TCO free cases, light trapping inside the dome structure is clearly superior to the light trapping achieved in the etched silicon layer.

Regarding the back reflector design no large influence of the back reflector on the absorptance inside the silicon and front TCO layers was found in case of the conformal and the flat ZnO:Al / Ag back reflector design. Absorption in the silicon layer is almost identical to the reflectorless case. However, the different reflector layouts lead to a different distribution of the incoming energy flux into reflectance as well as transmittance, or absorptance in the back TCO and silver layers. Total absorptance is very high in case of the flat ZnO:Al / Ag back reflector and Haase [HS07] stated that a flat back reflector design is generally beneficial for light trapping compared to a conformal back reflector design. In this context it remains to be cleared whether the high absorptance inside the back ZnO:Al layer of the flat layout could be turned into silicon absorptance if replaced by a low–absorbing back TCO material. The

absorptance of silver is only on the order of a few percent in case of the flat back reflector layout. Here, reduced surface area may play a role in addition to the suppression of plasmonic excitation.

A recent experimental evaluation of detached reflector designs for μc–Si thin film solar cells with rough interface textures by Moulin [Mou+11; Mou+12] resulted in an absorption enhancement of the silicon layer with respect to the customary conformal ZnO:Al / Ag back reflector. In Moulin's studies of buffer materials between the silicon absorber and the back reflector, low index materials were generally preferential. In the detached back reflector design included here the back TCO of the flat back reflector layout discussed above was substituted by air. This back reflector layout shows a considerable increase of absorptance in silicon with respect to the other layouts. High LPIF values in silicon are attained close to the band edge and the silicon layer thickness corresponding to the wavelength integrated absorptance, cf. Table 4.2, is greater than 50 μm in this case. However, it is not clear whether this effect is mainly due to decreased parasitic absorptance or due to the change in refractive index. Also the trends seen by Moulin might be due to a better optical spacing to the silver reflector, thus reducing parasitic absorption.

back reflector type	etched	unetched
none (air)	13	19
conformal ZnO:Al / Ag	13	14
flat ZnO:Al / Ag	11	10
flat air / Ag	19	25

Table 4.1.: *Average LPIF values in the wavelength range between 1000 nm and 1100 nm for the tested back reflector layouts. Computation as described in section 4.2.7.*

back reflector type	etched	unetched
none (air)	31 μm	38 μm
conformal ZnO:Al / Ag	31 μm	34 μm
flat ZnO:Al / Ag	29 μm	32 μm
flat air / Ag	37 μm	51 μm

Table 4.2.: *Silicon layer thicknesses with identical wavelength integrated absorption as the thin film layouts. Computation as described in section 4.2.7.*

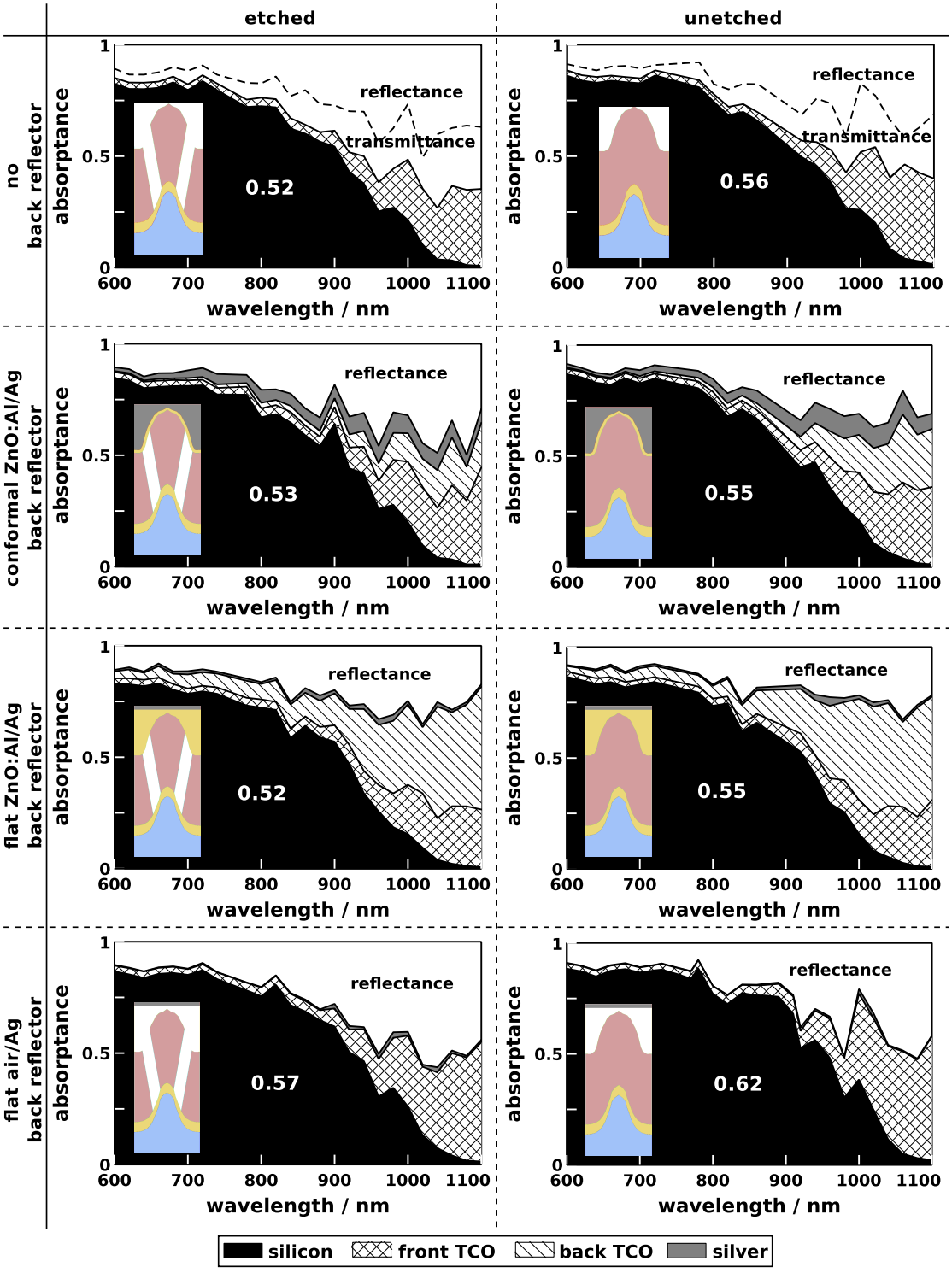

Figure 4.12.: *Comparison of cell absorptance fractions for unetched (left) and etched (right) solar cells on a 2 µm periodic substrate with a nominal height of 2.4 µm silicon deposited before etching. Different back reflector designs are compared in the vertical direction. Layout cross–sections are included in the diagrams. White numbers indicate the average absorptance of silicon in the displayed wavelength range.*

4.3. Discussion and outlook

This chapter on light trapping by periodic textures demonstrated that good light trapping performance can be achieved with designs suitable for a controlled polycrystalline silicon growth.

The reconstruction of the experimental nanodome texture's average unit cell from TEM images performed for the geometric model construction in section 4.2.2 can be seen as a competitional method to AFM scans in cases where this method of directly obtaining 3D height distributions fails. Of course the TEM method relies on the availability of very large TEM images propagating through the texture under an oblique angle to the grid vectors. In cases of textures with very steep sidewalls this angle might be critical on the success of the method. Also the preparation process of TEM samples is tedious as it requires glueing, mechanical abrasion and ion milling steps, although these processes are well established. No complex preprocessing is required for AFM scans.

Nanodomes seem to be a geometry very suitable for light trapping, as already demonstrated for amorphous silicon solar cells in the substrate layout by Zhu [Zhu+08; Zhu+09; Zhu+10]. The benefit of the polycrystalline silicon cells targeted by the textures simulated in this chapter is the possibility of reaching an absorber thickness of $4\,\mu$m to $5\,\mu$m without significant electrical losses. This allows a wide range of possible designs. Experimentally, the deposition and etching processes also worked well on samples with nominally $4.1\,\mu$m high silicon deposition. The domain scaling simulations in section 4.2.7 demonstrated the importance of reaching high LPIF values at large material volumes. Optical measurements were done on on etched $2\,\mu$m periodic samples with nominally $4.1\,\mu$m silicon height before etching and no back reflector, as depicted in Fig. 4.3, and showed a moderate increase in device absorptance in comparison to the samples with nominally $2.4\,\mu$m silicon height. Simulations of these textures have not been done yet. Textures with an increased material height and optimized back reflector design would also be interesting for texture periods around 900 nm where light path improvement factors are highest. However, light trapping might be subject to considerable angle sensitivity at such low texture periods, as already discussed by Yu [YRF10a; YF11].

The unit cell shapes used in the analysis within this chapter were mirror symmetric. Further improvement of the light trapping performance might be possible by using asymmetric unit cell shapes. Yu [YF11; YRF10a; YRF10b] and Weiss [Wei+10] showed the benefit of using asymmetric unit cells smaller or equal to the wavelength of light for modal coupling into odd modes under normal indicence. Yu also showed that this benefit existed no longer when texture size depasses the wavelength. As in most of the tested designs the lateral size of the textures is large compared to the wavelength there should therefore be no disadvantage resulting from

the symmetry considering modal coupling. Still there could be an advantage in the use of asymmetric unit cells also in case of texture periods larger than 1 μm from superstrate light trapping. In case of symmetric textures and normal incidence efficient reflection from zero order into non–zero order modes after the first pass through the solar cell is probable to result in efficient reflection into the zero order mode after the next pass. Most of this light is then reflected out of the cell. Asymmetric unit cells were already considered in literature, e.g. by Thorp [TCW96], for a more efficient geometrical superstrate light trapping.

Planar anti–reflection coatings may also be considered for the presented layouts at the air / superstrate interface to further enhance cell absorptance. The superstrate light trapping scheme which yields and additional benefit of about 10% of the incoming power flux in case of the 2000 nm periodic layout would not be strongly affected by this as the escape cone between glass and air is not altered by insertion of a planar layer.

Finally the angular sensitivity of the presented light trapping concept remains to be probed to ensure that light trapping is good also at oblique incident angles.

4.4. Conclusion

The precedent chapter assesses the possibilities of a periodic light trapping system which is suitable for implementation into polycrystalline silicon solar cells. A geometrical model of a complex, experimentally realized material distribution was obtained from TEM and SEM images. The model was experimentally verified by comparison to optical absorptance measurements. An incoupling analysis highlighted good transmittance into the silicon absorber of the solar cell in comparison to a flat material layout. The incoupling into silicon was found to be strongly dependent on the surface angle distribution but less on the height distribution and the texture period.

Using an incoherent iterative coupling of the superstrate and the solar cell several scaled versions of the nanodome light trapping geometry, completed with a conformal back reflector, were simulated. To assess the importance of superstrate light trapping the contributions of superstrate light trapping were considered separately from the contributions of primary light trapping by the textured solar cell. The results showed that in case of normal incidence on the textured cells superstrate light trapping can account for about 20% of the total absorptance for texture pitches around 900 nm and levels to about 10% for larger texture pitches. Primary light trapping of the scaled textures was found to have maxima at 500 nm and around 900 nm texture pitch. These maxima match with the optimal texture periods reported by other groups [Wei+10; Zen+08; CK+09; She+11b; AP09; Isa+; Pae+11b; Pae+11a]. Including the

superstrate light trapping into the analysis yielded light path improvement factors up to 16 for averaged values in the wavelength range between 1000 nm and 1100 nm and 900 nm texture period. This light trapping efficiency, computed for the case of an actual solar cell design, is well below the limits calculated by Yablonovitch [Yab82] and Yu [YF11] for ideal systems.

A variation of the back reflector for the experimental layout with 2 μm texture pitch showed that, compared to a conformal back reflector design, a flat back reflector design with a high volume of absorptive back TCO does not result in a loss of absorptance inside silicon. The absorptance inside silicon could further be brought to a much higher level by using a detached flat silver back reflector. These results suggested that a flat back reflector with a low refractive index, low-absorbing spacer medium should preferentially be implemented in the solar cell.

In summary, an implementation of the presented periodic light trapping structure into the conventional back- and front-contacted polycrystalline thin-film silicon solar cell technology would not lead to a considerable higher absorptance than already achieved in state-of-the-art nanocystalline thin film solar cells, as e.g. by Yamamoto [Yam+00] who is referenced for the nanocrystalline cell record by Green [Gre+12]. A major improvement in silicon absorption enhancement may require a new cell structure with significantly reduced parasitic losses and would be faciliated by achieving 4 μm or more of high quality absorber height in polycrystalline thin film growth.

5. Excursus: Application of small period silicon nanodome textures as photonic crystals

Scalability of the of the periodic dome texture generation method presented in the previous chapter was already mentioned in section 4.2.1. Scaling it down to periods of only a few hundred nanometers shifts the lowest photonic bands of the structure to the near infrared where silicon has very low absorption losses. As the operating range of modern fiber optics based telecommunication technology lies in the near infrared regime between 1300 nm and 1600 nm optical devices controlling light in that range are of a high technological relevance. One of the major problems in the building of microscopic optical devices allowing for optical chip design is light confinement to narrow light paths [OY01]. An already proven way of achieving such encapsulation is by photonic crystal structures. This optical technology was developed by Yablonovitch [Yab93] and John [Joh91]. Since then, many 1D, 2D and 3D photonic devices have been controlling the flow of light localized in defect structures within photonic crystals [Bus+07; Joa+08]. Best encapsulation and control of light is achieved by 3D photonic crystal structures, but their fabrication is technologically very difficult. A more promising way of controlling light is using 2D photonic crystal structures in a thin slab waveguide fabricated from material with a high refractive index. For example, silicon can provide the required encapsulation in the third dimension [Cho+00]. Large area formation of micrometer sized pores in silicon by using Laser interference lithography or illumination mask based lithography and etching processes has been demonstrated by Grüning [Gru+96]. Laser interference lithography (LIL) can provide periodic patterning on large areas without production of a lithography mask but is unable to produce the defect patterns required to build optical circuits. Simultaneous writing of photonic crystal and defect structures is possible by mask based optical lithography as used for chip design [Bir+01], but expensive high precision devices are necessary for pattering of sub–micrometer structures. As an alternative the use of fast ion beam deposition was suggested by Vogelaar [Vog+01] to directly write defect structures on samples previously

patterned with large area photonic crystal structures using LIL. This work flow is convenient for writing large area test designs and to–scale master layouts. For production, however, writing of a complete layout in only very few rapid production steps is preferential. A suitable low–cost processing method with a low time consumption is the embossing of textures and overcoating by a high refractive index material. The use of this process to form waveguide structures has already been suggested in the 1980s by Lukosz [LT83]. Weiss [WMK10] recently reported a characterization of an inorganic nano–imprint lithography method for production of line gratings with steep texture flanks and only a few hundred nanometers texture pitch. He also demonstrated its almost defect–free applicability to several tenths of square centimeters.

In a joint paper of Becker [Bec+12] and the author of this thesis the optical properties of very small textures of nanodome shape with 2D square periodicity and a unit cell pitch of only 300 nm was investigated. Lowest bands are supposed to lie in the near infrared and visible range for this texture pitch. The experimental texturing combining solgel imprint with electron beam deposition of silicon, SPC and subsequent etching of amorphous parts might be suitable to form grid textures of the overcoated silicon layer which could act as 2D photonic crystals. To the present experimental evidence of a photonic band structure was collected by reflection measurement. The obtained band structure was compared to a calculated band structure. Results were published in reference [Bec+12]. This section presents the simulation results included in the paper and an extended discussion of the experimental measurement technique.

5.1. Technical details

Adaption of the geometric model

The geometrical model reconstructed in section 4.2.2 for the light trapping textures was used as a basis for the 300 nm pitch structures. Silicon was assumed to be directly deposited on the solgel layer and not overcoated any further. A comparison of scattering simulations on the scaled–down model with angle resolved reflectance measurements in $\Gamma \rightarrow X$ direction suggested that the small experimental textures were morphologically not completely identical to the textures reconstructed from larger pitches. The interface morphology was therefore optimized for a single spectral feature as follows. A spectral match between experiment and simulation was sought for the lowest frequency resonance peak position in the reflectivity measurements in $\Gamma \rightarrow X$ direction. Incident angles from 20° to 70° and p– as well as s–

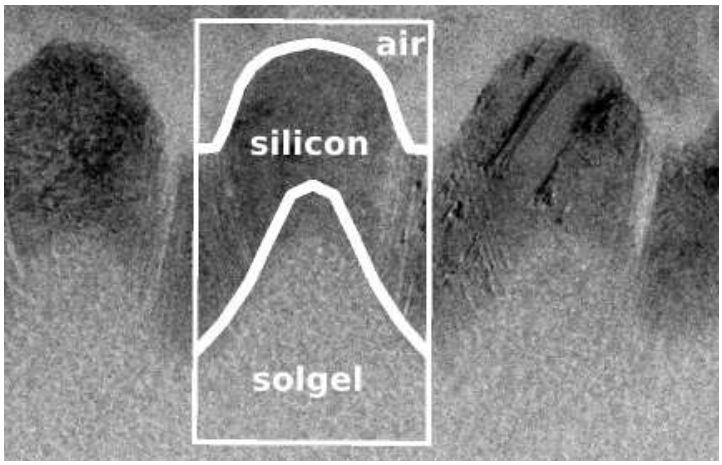

Figure 5.1.: *Cross–sectional TEM image of the nanodome texture with 0.3 µm pitch. The TEM cut is assumed to be close to the center of the unit cell. White lines depict the boundaries and material interfaces at the center of the computational model.*

polarized light were taken account. A scaling function,

$$\tilde{z} = c(z_{\max} - z_{\min})\left(\frac{z}{(z_{\max} - z_{\min})}\right)^{k} + z_{\min}\,, \tag{5.1}$$

where $z_{\min/\max}$ are the minimum and maximum height values of the respectrive interface, was applied independently to both interfaces. A good match of the lowest frequency resonance peak was found for $k = \frac{2}{3}$ with $c = 0.7$ for the silicon / air interface and $c = 1.2$ for the solgel / silicon interface. The etching angle was subsequently determined from the top cone diameter in SEM images depicting the etched silicon / air interface.

Cross–sectional TEM images were available for comparison at a later time. The TEM image with the maximum diameter of the silicon / air interface was chosen for comparison as this should be the cross–sectional view closest to the unit cell's center. The comparison to the center cross–section of the simulated geometry is depicted in Fig. 5.1. White lines traced on top of the image show the cross–section of the model unit cell. The silicon / air interface was found to compare quite well to the measurement. The most prominent differences between TEM image and the model can be found at the tip of the solgel / silicon interface. Cross–sections of the etched silicon structures (see section 4.2.2 for a description of the etching) are included as insets in Fig. 5.3. The conical cuts representing the etching were probably not placed under the right angle. The removed material volume also seems to be underestimated in comparison to the TEM images.

Description of the simulations

Both scattering and eigenvalue problems were solved on computational domains with periodic boundary conditions in the horizontal directions and transparent PML boundaries in the vertical direction. The computational domain consisted of three material layers as depicted in Fig. 5.1. Refractive index values of crystalline silicon were assumed for the silicon layer. All material properties except for the silicon data set used in the simulations are given in appendix A. The silicon data set used in this chapter differs from the crystalline silicon data set used for the simulations in the previous chapter. The two data sets and resulting band structures are compared in detail in appendix B.3. No fundamental differences were observed when substituting the material data with the crystalline silicon data depicted in Fig. A.2.

The experimental setup used for reflectance measurement is depicted schematically in Fig. 5.2 (a). In scattering simulations a plane wave was used as incident field at the side of the air half space. As in the experiments simulations with incident angles between 20° and 70° with a 5° spacing along the high symmetry directions $\Gamma \rightarrow X$ and $\Gamma \rightarrow M$ were performed. Solutions for both s– and p–polarized light were computed at every incident angle.

To obtain the full band diagrams depicted in Fig. 5.3 the eigenvalue problem was solved for horizontal components of the wavevector along the directions $\Gamma \rightarrow X$ and $\Gamma \rightarrow M$. As a single PML discretization can not be assumed to be good for the entire frequency range scattering simulations with adaptive PML refinement were used to obtain a good PML discretization for disjoint search intervals in frequency space. An additional sub–devision into frequency intervals was performed to include dispersion and absorption of silicon in the simulations of the unetched structures for which experimental comparison was sought. The interval boundaries across which material properties were altered are included in the band diagrams in Figures 5.2 and 5.3 as horizontal orange lines. For any fixed interval of the resulting division an initial guess for the eigenvalue solver was placed in the center of the interval. A series of solver restarts with different eigenvalue guesses was performed until full coverage of the search interval was reached.

Removal of unphysical solutions

A solution of the eigenvalue problem with transparent PML boundary conditions can lead to computation of unphysical solutions [Rec05; Ket12b; Ket12a]. These have been found to cluster along the light lines and other straight lines through the origin lying in the guided mode regime below the light lines. Field energy density of such solutions is often high at the PML boundary and low in the actual guiding layer. An energy thresholding criterion was used

to discriminate the unphysical solutions from the physical solutions. This procedure worked quite well in the present case but may also have resulted in the discrimination of some physical eigenvalues.

Band tracing and reasons for incomplete band coverage

Many bands crossing or touching in the dispersion diagrams which are traced in the 2D space $[k_{\|}, \Re(\omega)]$ of the horizontal wave vector component and the real part of the eigenvalue are actually well separated when considering the imaginary part of the eigenvalue. Piece–wise band tracing was achieved using an extrapolating propagation algorithm in the 3D space $[k_{\|}, \Re(\omega), \Im(\omega)]$. Empirical criterons where used for tolerance of the deviation to the extrapolation and tracing stops. Some band kinks and shifts are visible across the boundaries of the material intervals in Fig. 5.3, upper left, which resulted in the sudden ending and restarting of bands. Additionally a number of eigenvalues, which was found close to the straight lines holding the unphysical solutions, was suppressed along with these eigenvalues during energy thresholding. Finally incomplete coverage might have been induced by the iterative restarting algorithm. It is not guaranteed that the extacly same numeric values are found for a single eigenvalue in two runs of the Arnoldi eigenvalue solver due to random initialization. Shifts of eigenvalues together with the implemented piecewise interval coverage method might have resulted in suppression of eigenvalues, as any eigenvalues found outside of the search interval were consequently neglected.

5.2. Discussion of the bandstructure obtained by angular resolved reflectance measurements

An experimental test of the optical quality of the nanodome arrays was done by measuring the reflectance of light under oblique incidence to obtain insight into the photonic band structure above the light line. As outlined in the corresponding paper [Bec+12] measurements were not performed with a focused light beam but with a spot size of several square millimeters, thus illuminating millions of nanodomes. The experimental configuration should therefore be close to the model assumption of illumination by a plane wave.

The angular resolved reflectance method for probing 2D photonic crystals was developed by Astratov [Ast+99] and further refined in the following years by obtaining accurate resonance positions by fitting Fano line shapes [Gal+05] and improvement of visibility of the photonic crystal bands [Krá+08]. A Fano line shape is produced in the reflected intensity due

to interference between a discrete state and a continuous background. For fitting purposes an Airy function may be used to model the background interference pattern [Gal+05]. Dependent on the relative phase of the discrete state and the background different line shapes can be produced as shown by Babić [BD10]. Using his notation the reflectance of a single discrete resonance and the continuous state is written

$$R(\omega) = \left| r_D(\omega) \exp(-i\Delta\xi) + \frac{r_R \Gamma_0}{i(\omega - \omega_0) + \Gamma_0} \right|^2 \tag{5.2}$$

for a discrete resonance of line width Γ_0 centered at ω_0. r_D and r_R represent the amplitudes of the direct (background) and the resonant contribution. Babić introduced the phase difference $\Delta\xi$ between the two contributions which controls the asymmetry of the resonance line. In his simulations he was able to produce line shapes resembling a single peak, a single dip or directly adjacent peak and dip. A spectral feature representing a single resonance may also change its shape at different incident angles if phase shifts of the direct and the resonant contribution do not match. A fitting of Fano–functions to resonances in the spectrum would therefore be desireable for accurate determination of their spectral position. However, this was found to be very difficult in case of the scattering spectra of the nanodome structure. A typical example highlighting the nature of the scattering spectra is depicted in Fig. 5.2 (a) on the right. The scattering spectrum obtained by 3D simulation is plotted along with two different models for the direct background. The red line shows the response of a 3–layer model using the effective thickness of the silicon layer. It does not agree with the scattering spectrum in the low–ω range where no more discrete resonances were found in the direct bandstructure computations shown below. Therefore a multilayer model was used consisting of 49 individual layers with an effective material representing the material fractions of the cross–section in the center of each slice. The model fits well in the low–ω range for all scattered spectra. The reflectance of the background model is very low compared to the reflectance of the dome–structures over the entire spectral range. Broad peaks as the one between 0.3 and 0.35 visible in the scattered spectrum should therefore not be separate discrete resonances on a background interference maximum but the result of the superposition of multiple discrete resonances and cannot be fitted solitarily.

A simultaneous fitting of multiple resonances with a multilayer background model was attempted but found not to be successful in many cases with strongly overlapping resonance lines. Therefore it was decided to apply the same by–eye marking procedure of spectral features as was used in case of the experimental data. To get a sense of induced errors narrow minima and maxima in the scattering spectra were marked and plotted separately along with

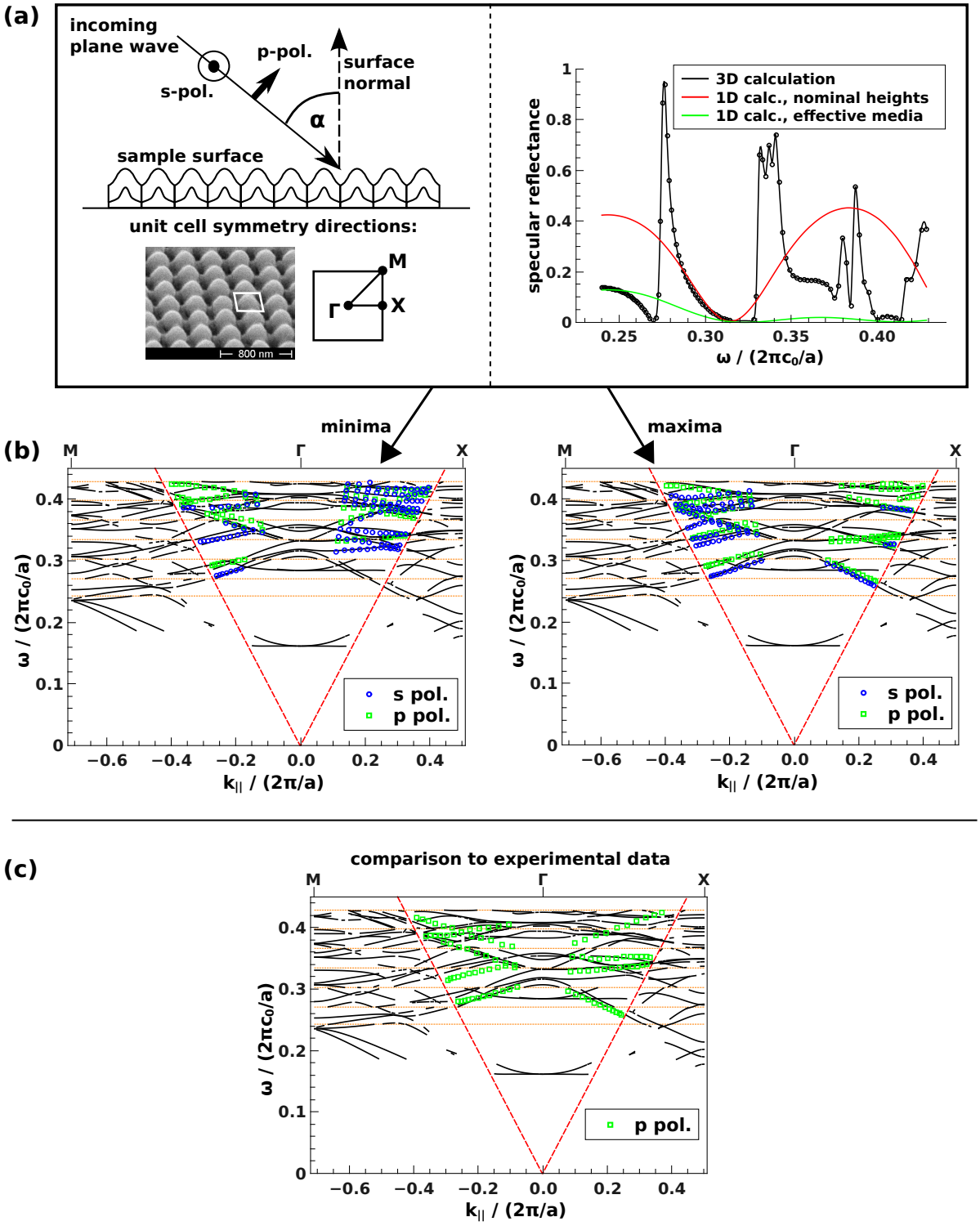

Figure 5.2.: ***(a)*** *Schematic of the reflectance simulation and experiments (left) and simulated reflectance of the model structure under illumination by a p–polarized plane wave incident under* $50°$ *to the surface normal in* $\Gamma \rightarrow X$*–direction.* ***(b)*** *Band spectra from direct computation (black lines) and tracing of narrow maxima and minima in the reflectance spectra. Light lines are included in red and refractive index intervals by horizontal orange lines.* ***(c)*** *Identical comparison as in (b) of the computed bandstructure to experimental data.*

the directly calculated bandstructure in Fig. 5.2 (b). For an incident angle α and a resonance position ω_0 the normalized location $[\tilde{k}_{\|}, \tilde{\omega}]$ in the dispersion diagram is given by

$$\begin{aligned} \tilde{k}_{\|} &= \frac{\omega_0}{c_0} \sin(\alpha) / \left(\frac{2\pi}{a} \right) \\ \tilde{\omega} &= \omega_0 / \left(\frac{2\pi}{a} c_0 \right) \end{aligned} \tag{5.3}$$

where c_0 is the vacuum speed of light and a is the pitch of the periodic grid.

The band structure above the light lines, as obtained from the scattering simulations plotted as colored markers in the band diagrams, agrees very well with the direct calculations shown in the form of lines. The tracing of maxima and minima in the spectra yields complimentary information in some spectral parts. Some of the resonances were favorably excited by s–polarized and others by p–polarized light. In summary a good coverage of the bandstructure above the light lines could be achieved by marking both narrow maxima and minima for both independent polarizations of the incident beam. Features might be multiply marked when applying this method, but this should decrease visibility of the band structure only in regions of high band density. Diagrams of all reflectance spectra with the marked positions can be found in Fig. B.1 in the appendix.

The experimental evaluation was performed on p–polarized light only. The obtained bands are plotted in Fig. 5.2 together with the computed bandstructure. Uncertainties of the simulation lie not only in the complex geometry, which is not precisely known, but also in the experimental material properties, which are known to deviate considerably from tabulated values of crystalline silicon, cf. section 4.2.5. A discussion of the silicon data set used for simulation here can be found in appendix B.3, which also discusses the flat band going through $k_{\|} = 0$, $\omega = 0.38$, that reacts very sensitive to a perturbation and therefore might be a non-physical band.

The agreement between simulated and experimentally determined band structure is good in the frequency range below $\tilde{\omega} \approx 0.37$, which corresponds to wavelengths above about 800 nm, but not for higher frequencies. In that frequency range the porous and amorphous parts of the silicon layer might alter the resonance structure, however the silicon volume was assumed to be uniform and close to crystalline in the simulations. Generally only well separated bands could be distinguished in the experimental data. This might indicate a broadening of the partially very narrow lines due to deviations of the unit cell from the average shape over the illuminated region.

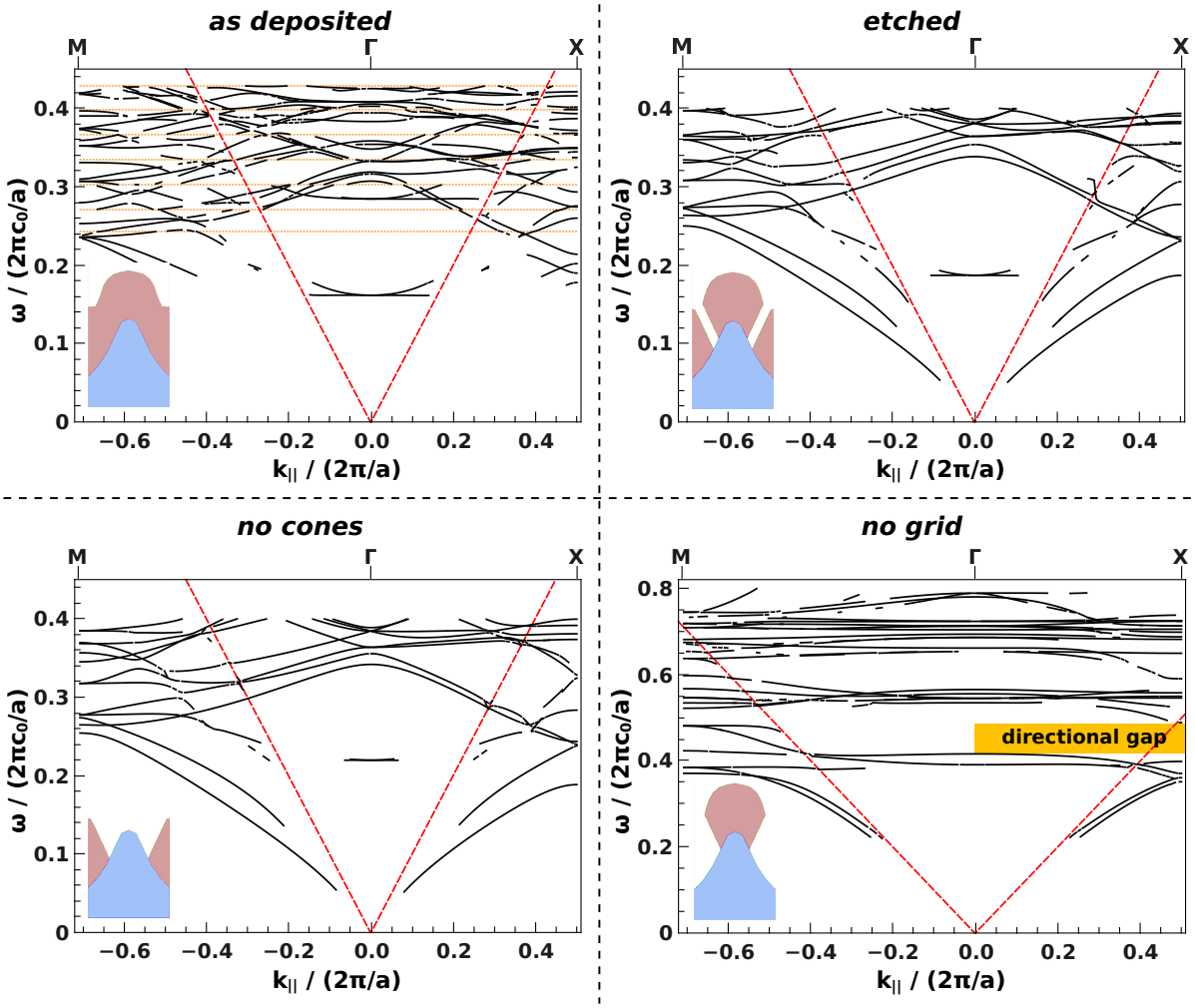

Figure 5.3.: *Simulated bandstructures of geometrical variations of the experimental structure. Insets into the different diagrams depict cross–sections through the different computational models.*

5.3. Discussion of the simulated bandstructures

The possible use of the periodic textures fabricated by imprint and silicon deposition could lie in the inexpensive replication of 2D photonic circuit designs where 2D photonic crystal structures confine light to waveguides as already mentioned above. To achieve complete confinement in 2D a complete bandgap must be realized for the working frequency of the optical device. Bandstructures of the current experimental realization and possible structural derivations were computed and are summarized in Fig. 5.3. All simulations but the one of the unetched structure were performed assuming a constant refractive index of 3.5 for silicon and no absorption. This choice of material properties is close to the properties of silicon at ener-

gies below the indirect band gap which is the actual target range of photonic crystal design. The upper left diagram in the Figure was simulated based on the silicon data set discussed in appendix B.3 and is thus not directly comparable to the diagrams featuring the etched absorber structure. The most relevant configuration for photonic circuit design would be the interconnected silicon grid residue created by lift–off of the isolated cones which was labeled *no cones* in the diagram. However, in case of the simulated structures only a partial bandgap in the $\Gamma \rightarrow X$–direction was found in absence of the silicon grid (lower right diagram) and for higher frequencies around $\tilde{\omega} = 0.45$.

The textures in their current state are not suitable for light confinement on 2D photonic devices. No bandgap engineering had been done prior to fabrication of these structures. The described experiments and simulations were only meant for verification of the structure generation and the optical measurement setup. It has been shown that overlapping complete band gaps of both polarizations of light can preferentially be reached in hexagonal lattices where the directional dependency of the bandstructure is lower and configurations suitable for the two polarizations can be realized simultaneously [Joa+08]. This will be considered for future designs.

5.4. Conclusion

A different field of application for the experimental texturing and deposition technique described in chapter 4 and originally developed for solar cells might lie in the inexpensive reproduction of planar photonic devices based on silicon. A demand of these devices is the in–plane guidance of light by a 2D photonic crystal structure. As a first test a commonly used combination of reflectance measurements and simulation for photonic band analysis was evaluated for nanodome arrays with 300 nm texture period. Using this technique the guided mode regime is not experimentally accessible but can be predicted from the simulations if a good comparability between experiment and simulation is reached above the light lines. Direct measurement of the guided modes would require a much more sophisticated experimental setup.

Considering the geometric complexity of the material distribution good accordance between experiment and computed bandstructure could be obtained for wavelengths above 800 nm. As no complete bandgap was found the studied nanodome textures are not useable as 2D bandgap materials in their present shape. The low–cost fabrication technique and wide applicability certainly motivates further work aiming at 2D photonic band gap materials.

6. Conclusion

Better light trapping concepts are a prerequisite for the success of silicon thin film photovoltaics. The focus of research in this area, which has long been on rough surfaces fabricated by growth or etching, is currently shifting towards more deterministic patterning techniques. These techniques, like nano–imprint lithography, allow for an easy replication of very complex geometries. Writing of optimized periodic or random patterns is in reach. Still, the characteristics of the material system impose constraints on possible patterns. Especially in case of polycrystalline silicon, growth conditions need to be strongly considered for light trapping texture design. Optical simulation has become an indespensable tool to analyze successful design concepts and to test variations of these.

In recent years a few groups reported the use of rigorous Maxwell solvers for optical simulation of thin film silicon solar cells with rough interfaces. Simulations of solar cells with rough interface patterns have also been performed for this thesis. As in other publications, the simulations relied on a Monte Carlo sampling of small rough surface patches. Despite of being able to rigorously solve the optical problem, model errors can still be made when using this technique, due to limitations in the space resolution of the textured solar cell.

An analysis of the model errors was done in this thesis, based on synthesized rough surfaces with a roughness similar to a commercial FTO surface. Good convergence to an absorptance standard deviation of 0.01 could already be reached at a low number of maximally 20 Monte Carlo samples, both for 1D and 2D rough surfaces. In a study of the domain size induced error for 1D rough surfaces, periodic boundary conditions were found superior to isolated boundary conditions, especially at small computational domain widths. In the simulation of 2D rough surfaces, for which only very limited computational domain sizes can be reached, a good correspondance of silicon absorptance curves was attained already between the simulation series of $1\,\mu$m and $1.5\,\mu$m domain width. Surface morphologies with a larger typical feature size than the FTO morphology used here might require larger computational domains. An application on experimental surface data and a comparison to measured quantum efficiencies of solar cells remains open.

Additionally to the general analysis of rough surface scattering simulation in silicon solar cells, an empirical partially coherent statistical ray tracing algorithm was tested against rigorous simulation. This work was done in cooperation with Janez Krč at University of Ljubljana. The chosen sample geometry of a finite silicon layer between two half spaces of air is very pessimistic in view of the approximate algorithm. The convergence of the approximate against the rigorous solution with increasing layer thickness was not good, which was attributed mostly to the lack of a back reflector in the layout. Literature comparisons to experimental EQE data suggest that the semi–coherent ray tracing method performs well in presence of a back reflector. The simulation results included here suggest that care should be taken in application of the empirical algorithm if layers of low refractive index follow layers of high refractive index in the solar cell layout, as for example in case of intermediate reflectors. An extension of this analysis to layouts including a back reflector and optionally an intermediate reflector are planned for future work.

A study in close connection to experimental work could be done in the field of periodic light management textures. A periodic unit cell material distribution was reconstructed for a silicon layer deposited on a solgel substrate with a 2 μm twofold periodic pattern. This reconstruction could be done with a very high precision by using cross–sectional TEM images. A comparison of optical absorptance measurements with the simulated absorptance of the computational model yielded a good quantitative agreement. The simulated absorptance of the silicon volume was very high in reference to a flat layer design with equal material volumes. More than 90% of incident light on the corrugated solgel interface were transmitted into the silicon volume at wavelengths above 450 nm. This is a 10% difference to the case of flat material layers, highlighting the good anti–reflection properties of the solgel texture. The simulated and measured absorptance in silicon was about 60% at 900 nm wavelength for the bare silicon layer deposited on the textured substrate, which is considerably higher than literature values for nanocrystalline solar cells with rough surface patterns.

To predict the absorption characteristics of a full solar cell, the computational model was completed with a conformal back reflector. For a further assessment of possible design enhancements, the model was scaled to different domain periods. Light path improvement factors of over 16 were found a texture period 900 nm, averaged for wavelengths above 1000 nm. However, the difference to the light path improvement for higher texture periods, where a stable plateau with a path improvement of about 13 is maintained, is not considerable. The highest silicon absorptance was found for the test layout with the highest silicon volume, at

2 μm texture pitch. This outcome emphasizes the requirement to fabricate devices with an absorber thickness of a few micrometers to reduce the absorptance efficiency gap to silicon wafer cells.

A further enhancement of absorptance with respect to the conformal back reflector layout could be reached by employing a detached flat back reflector. Air was used as spacer material in case of this simulation. The resulting cells had a single–pass comparable absorptance of more than 50 μm of silicon and a light path enhancement of up to 25 close to the band edge. Other low refractive index spacer materials with a small absorption coefficient should lead to a similar absorption enhancement in the flat back reflector design. A part of the gain obtained in this configuration can be attributed to reduced parasitic absorption, but the flat silver reflector seems to be generally preferential in case of the studied dome absorber structures. This is backed by the identical simulation with a spacer volume of absorptive ZnO:Al. Despite of a very high absorptance in the spacer material, this layout showed only a very small absorption loss in silicon with respect to the conformal back reflector.

In many publications on rigorous simulation of light trapping systems for thin film cells, the contribution of superstrate light trapping is consequently neglected. For some of the periodic layouts presented here, more than 20% of the absorptance in the silicon layer could be attributed to gains by superstrate light trapping. The superstrate light trapping therefore needs to be included, at least into simulations of thin film silicon solar cells with periodic light trapping concepts. Simulation methods which are able to compute solutions for many individual sources in batches, like the finite element method used with a direct solver, are clearly advantageous for the implementation of a superstrate coupling.

Planar photonic crystal structures are a different field of research for which the solgel patterning and silicon deposition methods, developed for solar cells, might be applicable. The optical quality of a patterned and silicon coated substrate of 350 nm period was assessed by a comparison of specular reflectivity measurements and simulations. Using this methodology the photonic band structure of the periodic device is accessible. Direct band calculations showed a good agreement to the measured data. Realizing a design with a band gap in the desired wavelength range is planned as the next step in the continuation of this project. If a photonic device with sufficiently high quality can be fabricated, the solgel imprint method, combined with silicon deposition, crystallization and etching, is an ideal toolchain for the replication of high index planar photonic devices on a silicon basis.

A. Material parameters

A.1. Glass

Non–absorptive glass with a refractive index of 1.52 was used for all simulations. The used refractive index may be somewhat higher than the value of 1.47 commonly found for borosilicate glasses. But this difference should not have had a substantial influence on the simulations.

A.2. ZnO:Al

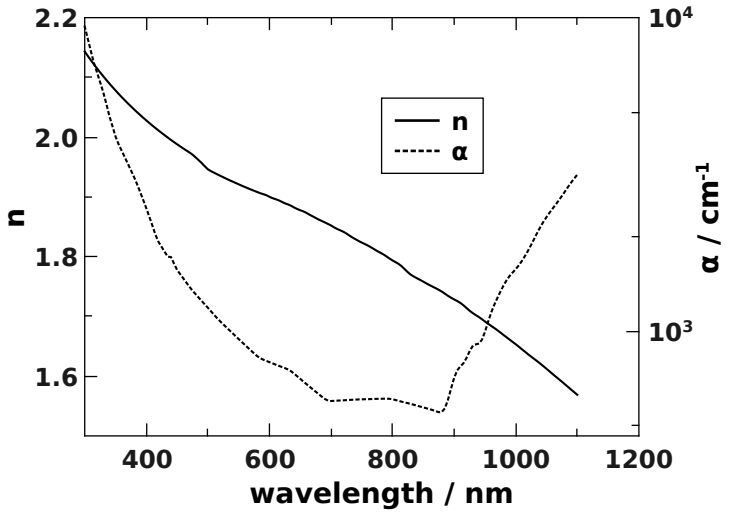

Figure A.1.: *Real part of the refractive index and absorption coefficient of ZnO:Al.*

The absorption coefficient of this material is somewhat higher than for typical rf–sputtered ZnO:Al but has been continuously used for all simulations of this thesis to maintain the comparability of results. This dataset is included in the electrical simulation software AFORS–HET [SKS06].

A.3. Silicon

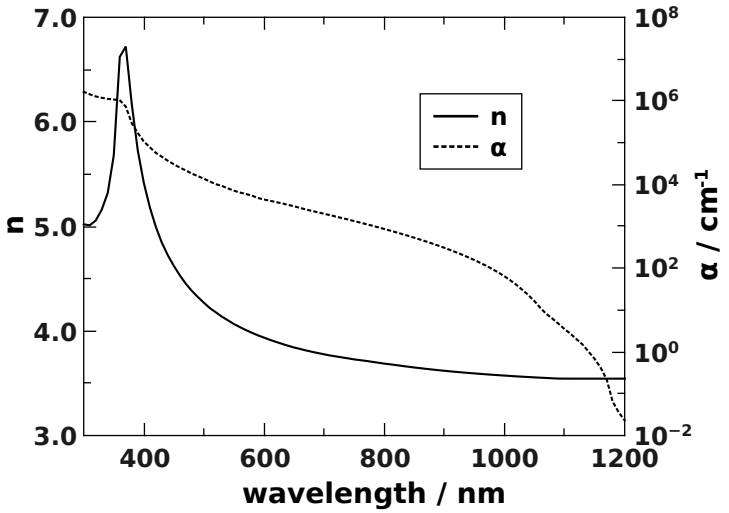

Figure A.2.: *Real part of the refractive index and absorption coefficient of silicon.*

The crystalline silicon dataset depicted in Fig. A.2 used for the simulations in this thesis is almost identical to the one tabulated on `http://photonics.byu.edu/tabulatedopticalconstants.phtml` which is referenced there to be originally published by Palik [PG98]. In the used dataset the absorption coefficient was tabulated until the band edge of crystalline silicon. Unlike the Palik dataset, the sampling point density remains very high in the wavelength range above 800 nm, which is important to avoid interpolation errors, cf. section B.3. This dataset is included in the electrical simulation software AFORS–HET [SKS06].

A.4. Silver

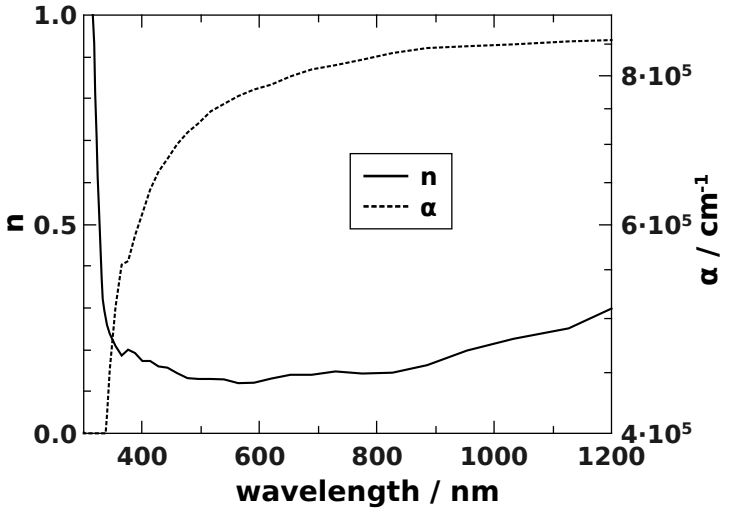

Figure A.3.: *Real part of the refractive index and absorption coefficient of silver.*

The silver dataset depicted in Fig. A.3 used for the simulations in this thesis was taken from `http://http://photonics.byu.edu/tabulatedopticalconstants.phtml` and is referenced there to be originally published by Palik [PG98].

A.5. ZrO_2

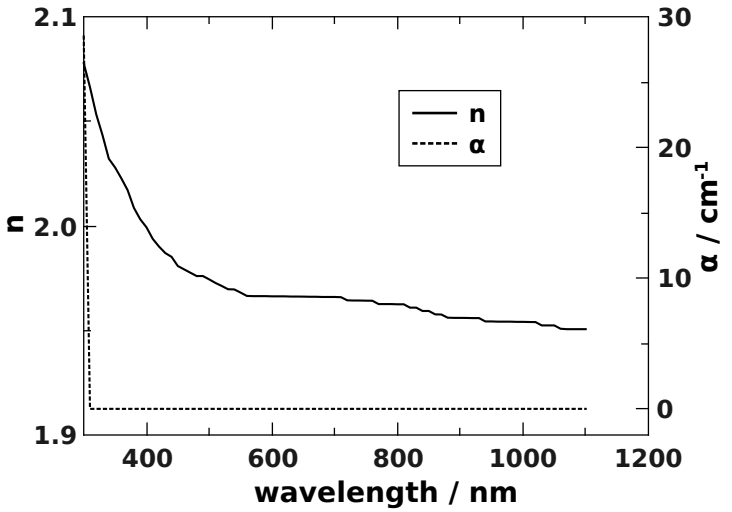

Figure A.4.: *Real part of the refractive index and absorption coefficient of ZrO_2.*

[Rit76; Ste+76]

B. Extended results and diagrams

B.1. Silicon absorptance and wavelength resolved light path improvement in scaled etched nanodome devices

Wavelength integrated absorptance and light path improvement factors were shown in section 4.2.7 to compare the device performance and light trapping performance at different scalings. The following plots show the wavelength resolved total absorptance of silicon together with the light path improvement factor of the complete light trapping system, i.e. including superstrate light trapping. The superstrate light trapping part, which is absorptance resulting from multiple reflection between the solar cell and the superstrate / air interface, was also included in the diagrams. As a guide to the eye for superstrate light trapping the limit wavelength positions at which the various diffraction orders in the glass superstrate get internally reflected were included as vertical lines. The first orders were labeled according to the labeling scheme in Fig. 4.1.

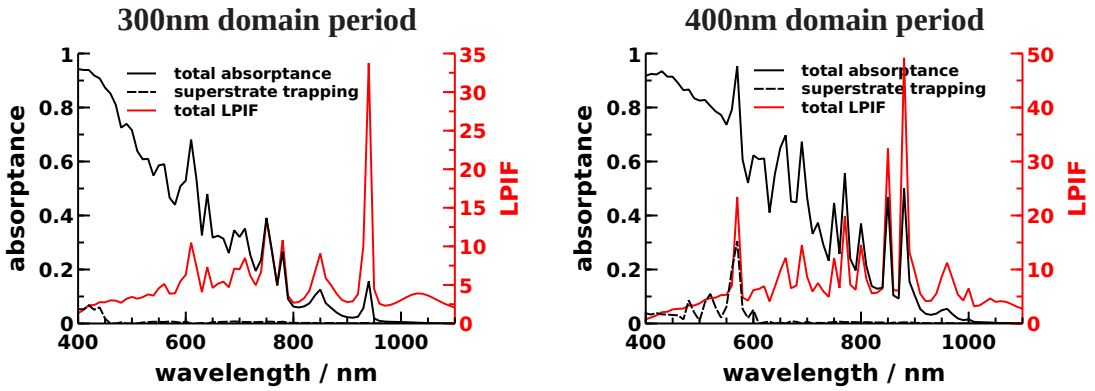

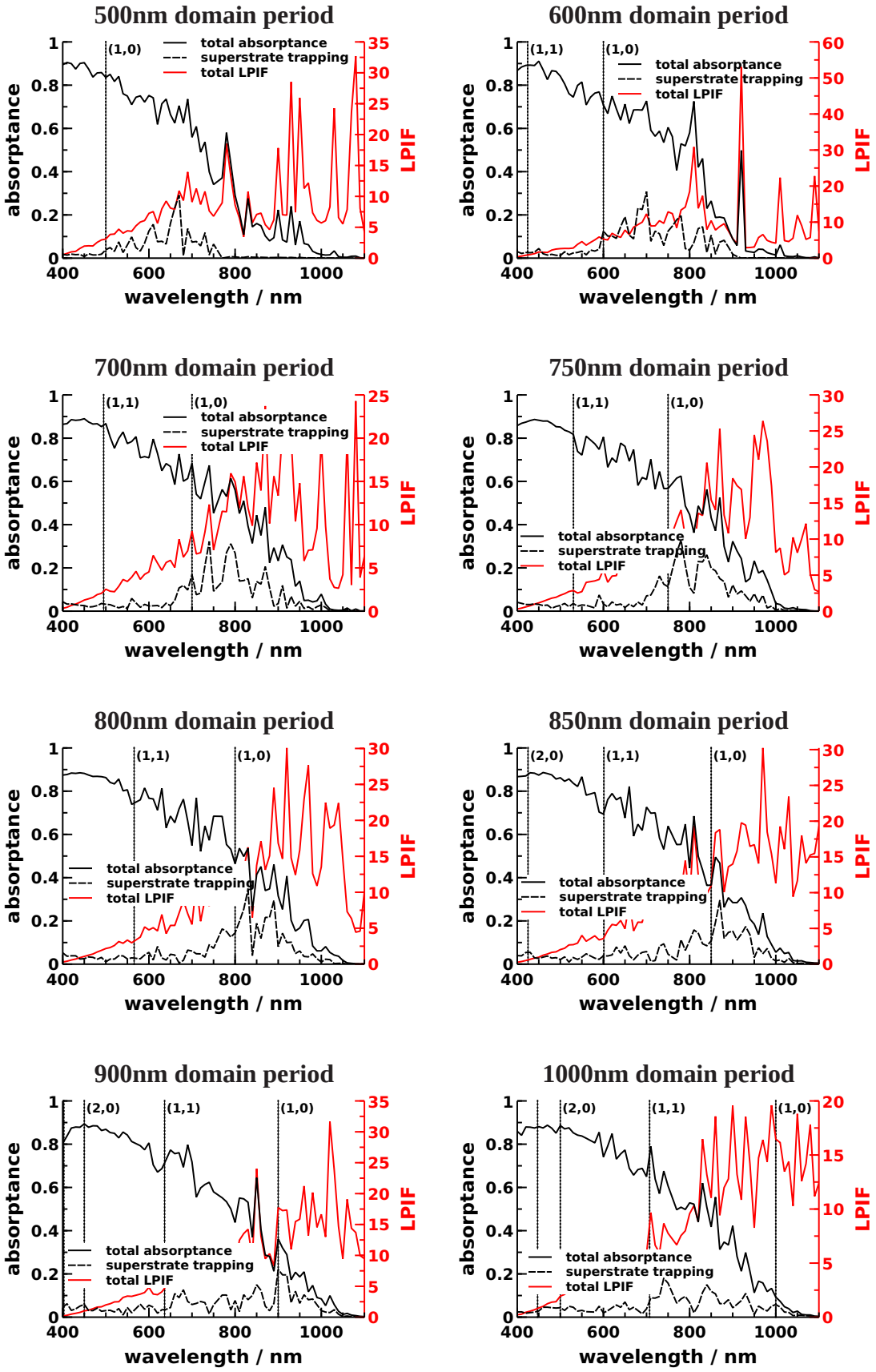
500nm domain period
(1,0)
total absorptance
superstrate trapping
total LPIF
absorptance
LPIF
wavelength / nm
600nm domain period
(1,1)
(1,0)
700nm domain period
(1,1)
(1,0)
750nm domain period
(1,1)
(1,0)
800nm domain period
(1,1)
(1,0)
850nm domain period
(2,0)
(1,1)
(1,0)
900nm domain period
(2,0)
(1,1)
(1,0)
1000nm domain period
(2,0)
(1,1)
(1,0)

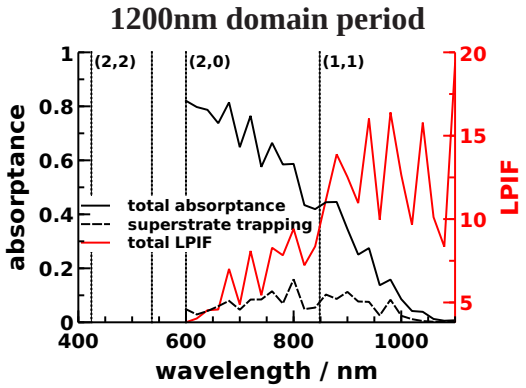
1200nm domain period
(2,2)
(2,0)
(1,1)
absorptance
LPIF
total absorptance
superstrate trapping
total LPIF
wavelength / nm

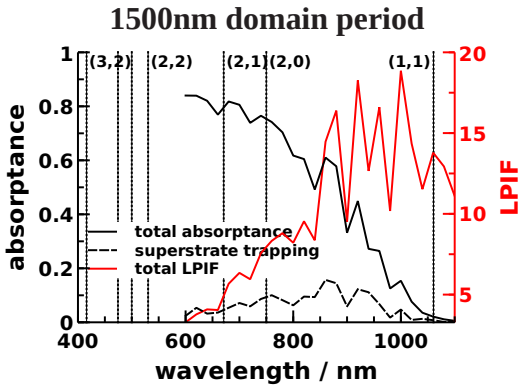
1500nm domain period
(3,2)
(2,2)
(2,1)
(2,0)
(1,1)
absorptance
LPIF
total absorptance
superstrate trapping
total LPIF
wavelength / nm

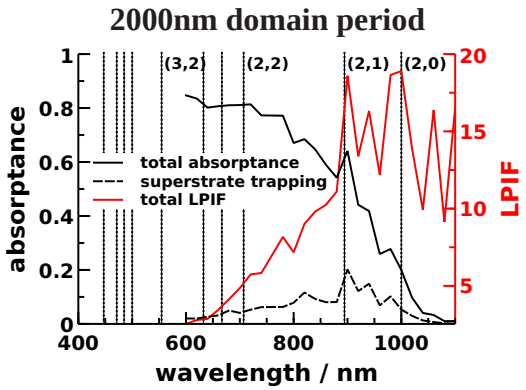
2000nm domain period
(3,2)
(2,2)
(2,1)
(2,0)
absorptance
LPIF
total absorptance
superstrate trapping
total LPIF
wavelength / nm

B.2. Bandstructure reconstruction from reflection spectra

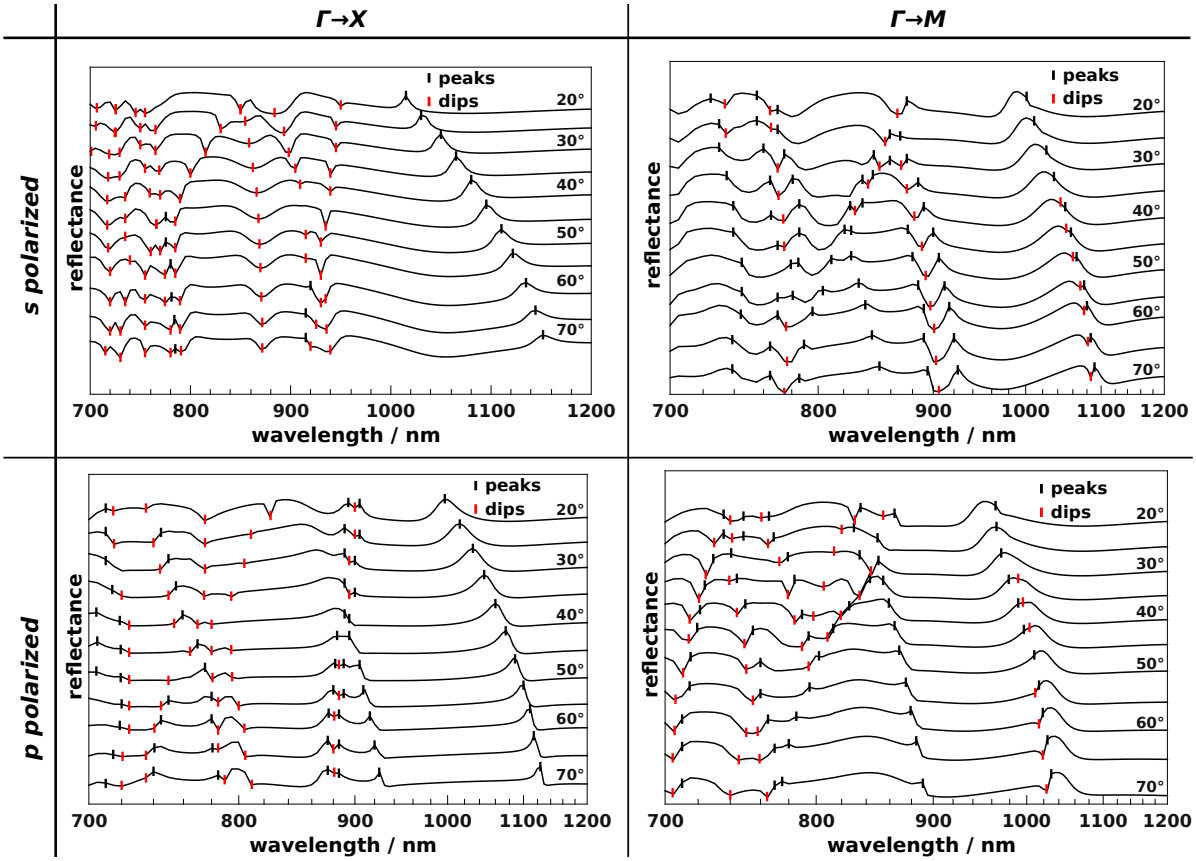

Figure B.1.: *Reflectance spectra showing specular reflectance for scattering simulations at incident angles between* 20° *and* 70° *in steps of* 5°. *The simulations were done for planes of incidence along the high symmetry directions* $\Gamma \rightarrow M$ *and* $\Gamma \rightarrow X$ *at the boundaries of the reduced Brillouin zone.*

Fig. B.1 depicts the scattering spectra used to determine the data points plotted in Fig. 5.2 above the light line according to equation 5.3. The wavelength positions used for calculation were marked with vertical black and red lines in the diagrams.

B.3. Discussion of the silicon material data used for calculation in chapter 5

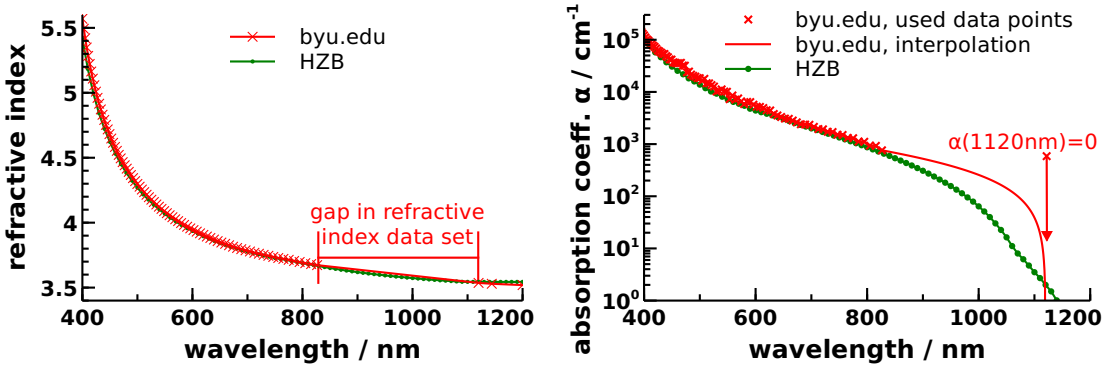

Figure B.2.: ***Left:*** *Refractive index data comparison between the data set shown in Fig. A.2, labeled "HZB", and the Palik data set [PG98], labeled "byu.edu" (cf. section A.3 for the web address to this data set).* ***Right:*** *Linear interpolation on linear scale of the absorption coefficient between the evaluation points of the refractive index data set shown to the left. The interpolation was sampled with a 1 nm spacing and shows strong differences to the densely sampled HZB data set for wavelengths above 826 nm.*

The band structure and scattering calculations presented in chapter 5 of this thesis were based on a different silicon data set than the computations of light trapping structures for solar cells in the other chapters. This data set, labeled "byu.edu" according to the web source it was taken from[1], features a very low point density for the refractive index data in the high wavelength range, marked in Fig. B.2, left, by "gap in refractive index data set". The absorption coefficient of this data set was interpolated between the positions of the refractive index data set, leading to the interpolation depicted in Fig. B.2, right. The linear interpolation on a linear scale lead to considerably higher values of the absorption coefficient in the range between 826 nm and the band gap, in comparison to the densely tablulated crystalline silicon data labeled "HZB" in Fig. B.2.

In the experimental comparison in Fig. 4.6, we recognized that a high sub band gap is present for the experimental absorber, which cannot be realized for crystalline silicon material. Crystalline silicon can therefore not be regarded as the ideal material data for obtaining experimental comparability in the high wavelength range and the "byu.edu" data set as shown in Fig. B.2, despite of being defective over the large evaluation point gap, may reflect experimental material properties better than a crystalline material data set.

[1] http://photonics.byu.edu/tabulatedopticalconstants.phtml

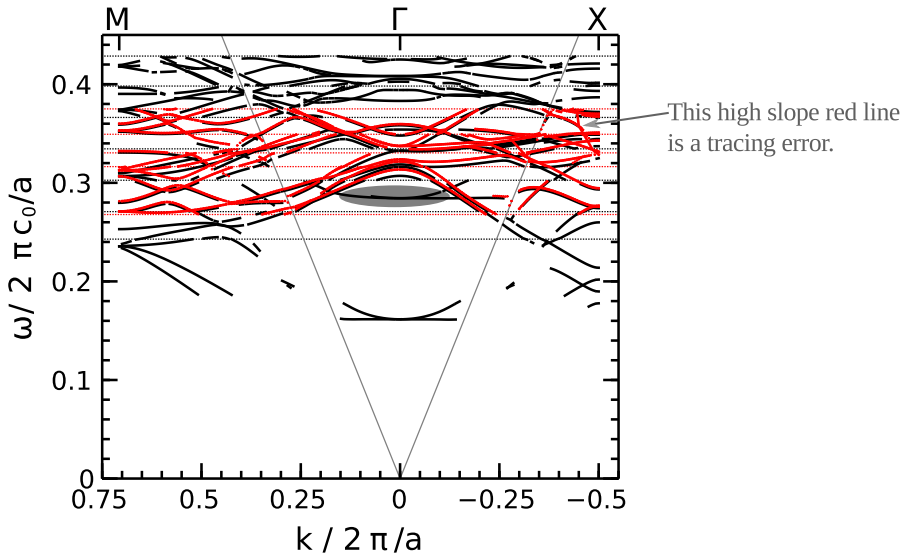

Figure B.3.: *Comparison of the band diagrams, as obtained for the two different silicon data sets shown in Fig. B.2 above. This plot refers to the diagrams in Figures 5.2 and 5.3. Axis labels: a – unit cell period; c_0 – vacuum speed of light.*
Strong black lines: *Data set labeled "byu.edu" in Fig. B.2.*
Strong red lines: *Data set labeled "HZB" in Fig. B.2. This data set is also shown in Fig. A.2. The spectral evaluation for this data set was only done in the region of high difference of absorption coefficients in Fig. B.2.*
Horizontal red / black lines: *Fine horizontal red and black lines denote the automatically chosen regions of constant refractive index and absorption coefficient for the two different simulation series.*
Details on the region marked by a grey ellipse within the diagram are given in the text.

To show that the differences in the computation of the band structure are small between the two data sets, the region of large differences in the absorption coefficient was recomputed based on the "HZB" data set from Fig. B.2. The results of this comparison are depicted in Fig. B.3. Aside from the observation that the two band structures are very similar, we notice a slight shift in band position, which is highest around the center frequency of the comparison frequency interval (matching with the gap in Fig. B.2) and gets lower towards the upper and lower boundaries of this interval. This behaviour reflects the difference between the two data sets "byu.edu" and "HZB" in the interpolation region and can therefore be attributed to the change in material properties. However, it can not be concluded from this comparison, whether the change is due to to the small relative difference in refractive index or due to the larger relative difference in the absorption coefficient.

A very interesting observation in the comparison of the two band structures is that no eigenvalues were recorded using the "HZB" data set in the region marked with an ellipse in Fig. B.3,

even before the threshold based removal of spurious modes described in the technical details section of chapter 5. It further is notable that also in case of the experimental spectra depicted in Fig. 5.2 (c), no traces of a band were observed in that spectral region. The strong sensitivity to changes in the material parameters, compared to the other observed bands, indicates that marked band might be an unphysical band which previously remained undetected.

List of publications

Papers

- Lockau, D., Zschiedrich, L., Burger, S., Schmidt, F., Ruske, F., Rech, B., “Rigorous optical simulation of light management in crystalline silicon thin film solar cells with rough interface textures”, In: *Proceedings of SPIE*, Vol. 7933, 2011, p. 79330M.

- Sontheimer, T., Rudigier-Voigt, E., Bockmeyer, M., Lockau, D., Klimm, C., Becker, C., Rech, B., “Light harvesting architectures for electron beam evaporated solid phase crystallized Si thin film solar cells: Statistical and periodic approaches”, In: *Journal of Non-Crystalline Solids* (2011), DOI: 10.1016/j.jnoncrysol.2011.10.025.

- Becker, C., Lockau, D., Sontheimer, T., Schubert-Bischoff, P., Rudigier-Voigt, E., Bockmeyer, M., Schmidt, F., Rech, B., “Large-area 2D periodic crystalline silicon nanodome arrays on nanoimprinted glass exhibiting photonic band structure effects”, In: *Nanotechnology* 23 (2012), p. 135302.

Conferences

- Lockau, D.; Zschiedrich, L.; Schmidt, F.; Burger, S.; Rech, B.: “Efficient simulation of plasmonic structures for solar cells”. *OWTNM’09* (optical waveguide theory and numerical modelling 2009), Jena, Germany (2009)

- Lockau, D.; Burger, S.; Zschiedrich, L.; Schmidt, F.; Rech, B.: “Rigorous optical simulation of rough interface light trapping structures in thin lm silicon solar cells”. *12th Euregional Workshop on Light Management in Thin Film Silicon Solar Cells*, Delft, The Netherlands (2010)

- Lockau, D.; Burger, S.; Zschiedrich, L.; Schmidt, F.; Rech, B.: “Efficient simulation of plasmonic structures for thin film silicon solar cells”. *DPG Spring Meeting 2010*, Regensburg, Germany (2010)

- Lockau, D.; Burger, S.; Zschiedrich, L.; Schmidt, F.; Rech, B.: “Rigorous optical simulation of rough interface light trapping structures in thin film silicon solar cells”. *DPG Spring Meeting 2010*, Regensburg, Germany (2010)
- Lockau, D.; Burger, S.; Zschiedrich, L. W.; Schmidt, F.; Ruske, F.; Rech; B.: “Rigorous optical simulation of light management in thin film polycrystalline silicon solar cells with textured interfaces”. *SPIE Photonics West*, San Francisco, USA (2011)

Bibliography

[Abr97] Petter Abrahamsen. *A Review of Gaussian Random Fields and Correlation Functions*. 2nd ed. Norsk Regnesentral, 1997. URL: http://publications.nr.no/917_Rapport.pdf.

[AF11] M. Agrawal and M. Frei. "Rigorous optical modeling and optimization of thin-film photovoltaic cells with textured transparent conductive oxides." In: *Progress in Photovoltaics: Research and Applications* (2011). DOI: 10.1002/pip.1158.

[Agr+10] M. Agrawal et al. "Comprehensive experimental and numerical optimization of surface morphology of transparent conductive oxide films for tandem thin film photovoltaic cells." In: *Photovoltaic Specialists Conference (PVSC), 2010 35th IEEE*. IEEE. 2010, pp. 000301–000304.

[Agr08] M. Agrawal. "Photonic design for efficient solid state energy conversion." PhD thesis. Stanford University, 2008.

[AP09] M. Agrawal and P. Peumans. "The physical limits of light trapping in thin-films and photonic structures that operate at the limit." In: *Photovoltaic Specialists Conference (PVSC), 2009 34th IEEE*. IEEE. 2009, pp. 002204–002207.

[Ast+99] VN Astratov et al. "Photonic band-structure effects in the reflectivity of periodically patterned waveguides." In: *Physical Review B* 60.24 (1999), pp. 16255–16258.

[Bat+11a] C. Battaglia et al. "Nanoimprint lithography for high-efficiency thin-film silicon solar cells." In: *Nano letters* 11.2 (2011), pp. 661–665.

[Bat+11b] C. Battaglia et al. "Nanomoulding of transparent zinc oxide electrodes for efficient light trapping in solar cells." In: *Nature Photonics* 5.9 (2011), pp. 535–538.

[Bat84] D.R. Bates. "Rayleigh scattering by air." In: *Planetary and Space Science* 32.6 (1984), pp. 785–790.

[BD10] Lj. Babić and M. J. A. de Dood. “Interpretation of Fano lineshape reversal in the reflectivity spectra of photonic crystal slabs.” In: *Opt. Express* 18.25 (2010), pp. 26569–26582. DOI: 10.1364/OE.18.026569.

[Bec+12] C. Becker et al. “Large-area 2D periodic crystalline silicon nanodome arrays on nanoimprinted glass exhibiting photonic band structure effects.” In: *Nanotechnology* 23 (2012), p. 135302.

[Ben+99] C. Beneking et al. “Recent developments of silicon thin film solar cells on glass substrates.” In: *Thin Solid Films* 351.1 (1999), pp. 241–246.

[Ber+06] Michael Berginski et al. “Design of ZnO:Al films with optimized surface texture for silicon thin-film solar cells.” In: *Proc. SPIE 6197*. 2006, 61970Y.

[Ber+07a] M. Berginski et al. “The effect of front ZnO: Al surface texture and optical transparency on efficient light trapping in silicon thin-film solar cells.” In: *Journal of applied physics* 101 (2007), p. 074903.

[Ber+07b] P. Bermel et al. “Improving thin-film crystalline silicon solar cell efficiencies with photonic crystals.” In: *Optics express* 15.25 (2007), p. 16986.

[BF79] P. M. van den Berg and J.T. Fokkema. “The Rayleigh hypothesis in the theory of reflection by a grating.” In: *J. Opt.Soc. Am.* 69.1 (1979), pp. 27–31.

[Bie+08] A. Bielawny et al. “3D photonic crystal intermediate reflector for micromorph thin-film tandem solar cell.” In: *physica status solidi (a)* 205.12 (2008), pp. 2796–2810.

[Bie+09] A. Bielawny et al. “Intermediate reflectors for enhanced top cell performance in photovoltaic thin-film tandem cells.” In: *Optics Express* 17.10 (2009), pp. 8439–8446.

[Bir+01] A. Birner et al. “Silicon-based photonic crystals.” In: *Advanced Materials* 13.6 (2001), pp. 377–388.

[Bit+08] K. Bittkau et al. “Nanoscale investigation of light-trapping in a-Si: H solar cell structures with randomly textured interfaces.” In: *physica status solidi (a)* 205.12 (2008), pp. 2766–2776.

[Bjø88] P.E. Bjørstad. “Multiplicative and additive Schwarz methods: convergence in the two-domain case.” In: *Proceedings of the 2nd International Conference on Domain Decomposition Methods*. 1988.

[BMD11] Adam Brown, Simon Müller, and Zuzana Dobrotková. *Renewable energy markets and prospects by technology*. IEA. Nov. 2011. URL: www.iea.org.

[Bra+00] Henning Braunisch et al. "Tapered Wave with Dominant Polarization State for All Angles of Incidence." In: *IEEE Transactions on Antennas and Propagation* 48.7 (2000), pp. 1086–1096.

[Bra92] Dietrich Braess. *Finite Elemente*. Springer-Verlag, 1992.

[Bre+97] R. Brendel et al. "Sol–gel coatings for light trapping in crystalline thin film silicon solar cells." In: *Journal of non-crystalline solids* 218 (1997), pp. 391–394.

[Bus+07] K. Busch et al. "Periodic nanostructures for photonics." In: *Physics reports* 444.3-6 (2007), pp. 101–202.

[BW59] Max Born and Emil Wolf. *Principles of Optics*. Pergamon Press, 1959.

[CG87] P. Campbell and M.A. Green. "Light trapping properties of pyramidally textured surfaces." In: *Journal of Applied Physics* 62.1 (1987), pp. 243–249.

[Cho+00] E. Chow et al. "Three-dimensional control of light in a two-dimensional photonic crystal slab." In: *Nature* 407.6807 (2000), pp. 983–986.

[CK+09] A. Campa, J. Krc, et al. "Analysis and optimisation of microcrystalline silicon solar cells with periodic sinusoidal textured interfaces by two-dimensional optical simulations." In: *Journal of Applied Physics* 105.8 (2009), pp. 083107–083107.

[CT10] S. Calnan and AN Tiwari. "High mobility transparent conducting oxides for thin film solar cells." In: *Thin Solid Films* 518.7 (2010), pp. 1839–1849.

[Dau+06] V. Terrazzoni Daudrix et al. "Characterisation of rough reflecting substrates incorporated into thin-film silicon solar cells." English. In: *PROGRESS IN PHOTOVOLTAICS* 14.6 (2006), 485–498. ISSN: 1062-7995. DOI: {10.1002/pip.681}.

[DB07] N. Dechamps and C. Bourlier. "Electromagnetic scattering from a rough layer: Propagation-inside-layer expansion method combined to an updated BMIA/CAG approach." In: *Antennas and Propagation, IEEE Transactions on* 55.10 (2007), pp. 2790–2802.

[DG09] J. Daillant and A. Gibaud. *X-ray and neutron reflectivity: principles and applications*. Vol. 770. Springer Verlag, 2009.

[Dom+10] D. Dominé et al. “Modeling of light scattering from micro- and nanotextured surfaces.” In: *Journal of applied physics* 107 (2010), p. 044504.

[DRY83] HW Deckman, CB Roxlo, and E. Yablonovitch. “Maximum statistical increase of optical absorption in textured semiconductor films.” In: *Optics letters* 8.9 (1983), pp. 491–493.

[FRL08] S. Fahr, C. Rockstuhl, and F. Lederer. “Engineering the randomness for enhanced absorption in solar cells.” In: *Applied Physics Letters* 92 (2008), p. 171114.

[Gal+05] M. Galli et al. “Measurement of photonic mode dispersion and linewidths in silicon-on-insulator photonic crystal slabs.” In: *IEEE Journal on Selected Areas in Communications* 23.7 (2005), pp. 1402–1410.

[Gal+09] S. Gall et al. “Polycrystalline silicon thin-film solar cells on glass.” In: *Solar Energy Materials and Solar Cells* 93.6-7 (2009), pp. 1004–1008.

[Gey92] C.J. Geyer. “Practical markov chain monte carlo.” In: *Statistical Science* 7.4 (1992), pp. 473–483.

[Gre+04] MA Green et al. “Crystalline silicon on glass (CSG) thin-film solar cell modules.” In: *Solar Energy* 77.6 (2004), pp. 857–863.

[Gre+12] M.A. Green et al. “Solar cell efficiency tables (version 39).” In: *Progress in Photovoltaics: Research and Applications* 20.1 (2012), pp. 12–20.

[Gru+96] U. Gruning et al. “Macroporous silicon with a complete two-dimensional photonic band gap centered at 5 μm.” In: *Applied physics letters* 68.6 (1996), pp. 747–749.

[Guo04] L.J. Guo. “Recent progress in nanoimprint technology and its applications.” In: *Journal of Physics D: Applied Physics* 37 (2004), R123.

[GY10] E. Garnett and P. Yang. “Light trapping in silicon nanowire solar cells.” In: *Nano letters* 10.3 (2010), pp. 1082–1087.

[Hai+07] A. Haines et al. “Policies for accelerating access to clean energy, improving health, advancing development, and mitigating climate change.” In: *The Lancet* 370.9594 (2007), pp. 1264–1281.

[Hau+08] F.J. Haug et al. “Plasmonic absorption in textured silver back reflectors of thin film solar cells.” In: *Journal of Applied Physics* 104.6 (2008), pp. 064509–064509.

[Hau+11] F.J. Haug et al. “Resonances and absorption enhancement in thin film silicon solar cells with periodic interface texture.” In: *Journal of Applied Physics* 109.8 (2011), p. 084516.

[Hei+08] M.C.R. Heijna et al. “Nanoimprint lithography of light trapping patterns in sol-gel coatings for thin film silicon solar cells.” In: *Proc. SPIE*. Vol. 7002. 2008.

[HS07] Christian Haase and Helmut Stiebig. “Thin-lm silicon solar cells with efcient periodic light trapping texture.” In: *Applied Physics Letters* 91 (2007), p. 061116.

[HSB95] Frank D. Hastings, John B. Schneider, and Schira L. Broschat. “A Monte-Carlo FDTD Technique for Rough Surface Scattering.” In: *IEEE Transactions on Antennas and Propagation* 42.11 (1995), p. 1183.

[HZW10] X.S. Hua, Y.J. Zhang, and H.W. Wang. “The effect of texture unit shape on silicon surface on the absorption properties.” In: *Solar Energy Materials and Solar Cells* 94.2 (2010), pp. 258–262.

[Ieaa] *Clean energy progress report*. IEA. June 2011. URL: www.iea.org.

[Ieab] *ENERGY POVERTY, How to make modern energy access universal?* IEA. 2010. URL: www.iea.org.

[Isa+] O. Isabella et al. “3-D optical modeling of thin-film silicon solar cells on diffraction gratings.” In: *Progress in Photovoltaics: Research and Applications* (). DOI: 10.1002/pip.1257.

[ISA08] D. Inns, L. Shi, and A.G. Aberle. “Silica nanospheres as back surface reflectors for crystalline silicon thin-film solar cells.” In: *Progress in Photovoltaics: Research and Applications* 16.3 (2008), pp. 187–194.

[Jac99] John David Jackson. *Classical Electrodynamics*. 3rd ed. Wiley, 1999.

[Jan+10] C. Jandl et al. “Simulation of tandem thin-film silicon solar cells.” In: *Proceedings of SPIE*. Vol. 7725. 2010, p. 772516.

[Jan+11] C. Jandl et al. “Simulation of Thin-Film Silicon Solar Cells with Integrated AFM Scans for Oblique Incident Waves.” In: *26th European Photovoltaic Solar Energy Conference and Exhibition*. 2011, pp. 2663–2666. DOI: 10.4229/26thEUPVSEC2011-3AV.2.23.

[Joa+08] JD Joannopoulos et al. *Photonic Crystals: Molding the Flow of Light*. Princeton Univ. Press, 2008.

[Joh91] S. John. “Localization of light.” In: *Physics Today* 44.5 (1991), pp. 32–40.

[JZ09] Klaus Jäger and Miro Zeman. “A scattering model for surface-textured thin films.” In: *APPLIED PHYSICS LETTERS* 95 (2009), p. 171108.

[Jäg+11] K. Jäger et al. “A full scattering model for integrated opto-electrical modelling of solar cells.” In: *Proceedings of the 26th EU PVSEC*. 2011, pp. 2311–2315. DOI: 10.4229/26thEUPVSEC2011-3BO.1.1.

[KAL05] B.M. Kayes, H.A. Atwater, and N.S. Lewis. “Comparison of the device physics principles of planar and radial pn junction nanorod solar cells.” In: *Journal of applied physics* 97 (2005), p. 114302.

[Kel+10] M.D. Kelzenberg et al. “Enhanced absorption and carrier collection in Si wire arrays for photovoltaic applications.” In: *Nature materials* 9.3 (2010), pp. 239–244.

[Kel+11] M.D. Kelzenberg et al. “High-performance Si microwire photovoltaics.” In: *Energy Environ. Sci.* 4 (2011), pp. 866–871.

[Ket12a] Benjamin Kettner. “Detection of Spurious Modes in Resonance Mode Computations – Pole Condition Method.” PhD thesis. Freie Universität Berlin, 2012.

[Ket12b] Benjamin Kettner. “The pole condition as transparent boundary condition for resonance problems: detection of spurious solutions.” paper in review for *SIAM Journal on Scientific Computing*. 2012. URL: http://epubs.siam.org/sisc/.

[Klu+04] Oliver Kluth et al. “Surface morphologies of rough transparent conductive oxide films applied in silicon thin-film solar cells.” In: *19th European Photovoltaik Solar Energy Conference*. 2004.

[Kol04] A. Kolodziej. “Staebler-Wronski effect in amorphous silicon and its alloys.” In: *Opto–electronics review* 12.1 (2004), pp. 21–32.

[Krá+08] Z. Král et al. “Characterization of 2D macroporous silicon photonic crystals: Improving the photonic band identification in angular-dependent reflection spectroscopy in the mid-IR.” In: *Materials Science and Engineering: B* 147.2-3 (2008), pp. 179–182.

[Krč+03] J. Krč et al. “Effect of surface roughness of ZnO: Al films on light scattering in hydrogenated amorphous silicon solar cells.” In: *Thin Solid Films* 426.1 (2003), pp. 296–304.

[Krč+04] J. Krč et al. “Optical modelling of thin-film silicon solar cells deposited on textured substrates.” In: *Thin solid films* 451 (2004), pp. 298–302.

[KST02] J. Krč, F. Smole, and M. Topič. “One-dimensional semi-coherent optical model for thin film solar cells with rough interfaces.” In: *INFORMACIJE MIDEM* 1 (2002), pp. 6–13.

[KST03] J. Krč, F. Smole, and Marko Topič. “Analysis of light scattering in amorphous Si: H solar cells by a one-dimensional semi-coherent optical model.” In: *Progress in photovoltaics* 11.1 (2003), pp. 15–26.

[Lac+11] J. Lacombe et al. “Three dimensional optical modeling of amorphous silicon thin film solar cells using the finite-difference time-domain method including real randomly surface topographies.” In: *Journal of Applied Physics* 110 (2011), p. 023102.

[Lan+11] T. Lanz et al. “Extended light scattering model incorporating coherence for thin-film silicon solar cells.” In: *Journal of Applied Physics* 110.3 (2011), pp. 033111–033111.

[Lew07] N.S. Lewis. “Powering the planet.” In: *MRS bulletin* 32.10 (2007), pp. 808–820.

[LGH04] P. Lechner, R. Geyer, and H.Schade. “Optical TCO properties and quantum efficiencies in thin-film silicon photovoltaics.” In: *19th European Photovoltaik Solar Energy Conference*. 2004.

[Li+03] M. Li et al. “Large area direct nanoimprinting of SiO–TiO gel gratings for optical applications.” In: *Journal of Vacuum Science & Technology B: Microelectronics and Nanometer Structures* 21 (2003), p. 660.

[Li+09] J. Li et al. “Design guidelines of periodic Si nanowire arrays for solar cell application.” In: *Applied Physics Letters* 95 (2009), p. 243113.

[Loc+11] D. Lockau et al. “Rigorous optical simulation of light management in crystalline silicon thin film solar cells with rough interface textures.” In: *Proceedings of SPIE*. Vol. 7933. 2011, p. 79330M.

[LPS94] F Leblanc, J Perrin, and J Schmitt. “Numerical modeling of the optical-properties of hydrogenated amorphous-silicon-based p-i-n solar-cells deposited on rough transparent conducting oxide substrates.” English. In: *Journal of Applied Physics* 75.2 (1994), 1074–1087. ISSN: 0021-8979. DOI: 10.1063/1.356489.

[LRS11] Gwénaëlle Legros, Kamal Rijal, and Bahareh Seyedi. *Decentralized Energy Access and the Millennium Development Goals*. The United Nations Development Programme, 2011. URL: http://www.undp.org/content/dam/undp/library/Environment%20and%20Energy/Sustainable%20Energy/UNDP-Decentralized-Energy-Access-and-MDGs-book.pdf.

[LT83] W. Lukosz and K. Tiefenthaler. "Embossing technique for fabricating integrated optical components in hard inorganic waveguiding materials." In: *Optics letters* 8.10 (1983), pp. 537–539.

[Löd+10] M. Lödl et al. "Abschätzung des Photovoltaik-Potentials auf Dachflächen in Deutschland." In: *11 . SYMPOSIUM ENERGIEINNOVATION*. 2010. URL: http://www.hsa.ei.tum.de/englisch/publications/2010/2010_Loedl_Kerber_Wi_Graz.pdf.

[Mei+94] J. Meier et al. "Intrinsic microcrystalline silicon (μc-Si: H)-a promising new thin film solar cell material." In: *First World Conference on Photovoltaic Energy Conversion, 1994*. Vol. 1. IEEE. 1994, pp. 409–412.

[MK09] Ellen Morris and Gathu Kirubi. *Bringing Small-Scale Finance to the Poor for Modern Energy Services: What is the role of government?* The United Nations Development Programme. 2009. URL: http://www.undp.org/content/dam/undp/library/Environment%20and%20Energy/Sustainable%20Energy/Small_Scale_Finance.pdf.

[MLS09] A. A. Maradudin, T. A. Leskova, and I. Simonsen. "Scattering of electromagnetic waves from two–dimensional randomly rough perfectly conducting surfaces." In: *Annual Review of Progress in Applied Computational Electromagnetics* 25 (2009), p. 505.

[Mon03] Peter Monk. *Finite Element Methods for Maxwell's Equations*. Oxford University Press, 2003.

[Mou+11] E. Moulin et al. "Study of thin-film silicon solar cell back reflectors and potential of detached reflectors." In: *Energy Procedia* 10 (2011), pp. 106–110. DOI: 10.1016/j.egypro.2011.10.161.

[Mou+12] E. Moulin et al. "Study of detached back reflector designs for thin-film silicon solar cells." In: *physica status solidi (RRL)-Rapid Research Letters* (2012). DOI: 10.1002/pssr.201105463.

[MW65] Leonard Mandel and Emil Wolf. “Coherence Properties of Optical Fields.” In: *Reviews of Modern Physics* 37.2 (1965), pp. 231–287.

[MW95] Leonard Mandel and Emil Wolf. *Optical coherence and quantum optics*. Cambridge University Press, 1995.

[NH06] L. Novotny and B. Hecht. *Principles of nano–optics*. Cambridge University Press, 2006.

[Nol90] Wolfgang Nolting. *Grundkurs: Theoretische Physik, Elektrodynamik (Band 3)*. 3rd ed. Verlag Zimmermann-Neufang, 1990.

[Nun+10] S. Nunomura et al. “Mie scattering enhanced near-infrared light response of thin-film silicon solar cells.” In: *Applied Physics Letters* 97.6 (2010), pp. 063507–063507.

[Néd80] J.C. Nédélec. “Mixed finite elements in $\mathbb{R}^3$.” In: *Numerische Mathematik* 35.3 (1980), pp. 315–341.

[OCS01] Open CASCADE S.A.S. *Open CASCADE Technology, 3D modeling & numerical simulation*. 2001. URL: `http://www.opencascade.org`.

[OY01] GA Ozin and SM Yang. “The race for the photonic chip: colloidal crystal assembly in silicon wafers.” In: *Advanced Functional Materials* 11.2 (2001), pp. 95–104.

[Pae+11a] U.W. Paetzold et al. “Design of nanostructured plasmonic back contacts for thin-film silicon solar cells.” In: *Optics Express* 19.106 (2011), A1219–A1230.

[Pae+11b] UW Paetzold et al. “Plasmonic reflection grating back contacts for microcrystalline silicon solar cells.” In: *Applied Physics Letters* 99.18 (2011), pp. 181105–181105.

[PDW07] D.M. Pawlowski, L. Deng, and M.D.F. Wong. “Fast and accurate opc for standard-cell layouts.” In: *Proceedings of the 2007 Asia and South Pacific Design Automation Conference*. IEEE Computer Society. 2007, pp. 7–12.

[PG98] E.D. Palik and G. Ghosh. *Handbook of optical constants of solids*. Academic press, 1998.

[Pom+07] J. Pomplun et al. “Adaptive finite element method for simulation of optical nano structures.” In: *phys. stat. sol. (b)* 244 (2007), pp. 3419 –3434.

[Pom10] J. Pomplun. “Reduced Basis Method for Electromagnetic Scattering Problems.” PhD thesis. Freie Universität Berlin, 2010.

[PY04] LIU Peng and JIN Yaqiu. “Numerical simulation of bistatic scattering from a target at low altitude above rough sea surface under an EM wave incidence at low grazing angle by using the finite element method.” In: *Science in China Ser. E Engineering & Materials Science* 47.3 (2004), pp. 293–304.

[Pyt] *PythonOCC: 3D CAD/CAE/PLM development framework for the Python programming language*. 2010. URL: http://www.pythonocc.org.

[Rec+03] B. Rech et al. “Microcrystalline silicon for large area thin film solar cells.” In: *Thin Solid Films* 427.1 (2003), pp. 157–165.

[Rec05] Maria Rechberger. “Numerical Methods for the Simulation of Acoustic Resonances.” MA thesis. Johannes Kepler Universität Linz, 2005.

[Ren] *Renewables 2011 global status report*. REN21. 2011. URL: http://www.ren21.net/REN21Activities/Publications/GlobalStatusReport/tabid/5434/Default.aspx.

[Rit76] E. Ritter. “Optical film materials and their applications.” In: *Applied Optics* 15.10 (1976), pp. 2318–2327. DOI: 10.1364/AO.15.002318.

[Roc+07] C. Rockstuhl et al. “Light localization at randomly textured surfaces for solar-cell applications.” In: *Applied Physics Letters* 91 (2007), p. 171104.

[Roc+10] C. Rockstuhl et al. “Comparison and optimization of randomly textured surfaces in thin-film solar cells.” In: *Opt. Express* 18.S3 (2010), A335–A341. DOI: 10.1364/OE.18.00A335. URL: http://www.opticsexpress.org/abstract.cfm?URI=oe-18-103-A335.

[Roc+11] C. Rockstuhl et al. “Light absorption in textured thin film silicon solar cells: A simple scalar scattering approach versus rigorous simulation.” In: *Applied Physics Letters* 98.5 (2011), pp. 051102–051102.

[RV+09] Eveline Rudigier-Voigt et al. “Sol-gel based structuring of the front-electrode in Si-based thin film PV device.” In: *24th European Photovoltaic Solar Energy Conference*. 2009.

[Sai+08] H. Sai et al. “Enhancement of light trapping in thin-film hydrogenated microcrystalline Si solar cells using back reflectors with self-ordered dimple pattern.” In: *Applied Physics Letters* 93 (2008), p. 143501.

[SCB07] R.E.I. Schropp, R. Carius, and G. Beaucarne. “Amorphous silicon, microcrystalline silicon, and thin–film polycrystalline silicon solar cells.” In: *MRS bulletin* 32.03 (2007), pp. 219–224.

[Sch+07] A. Schädle et al. “Domain decomposition method for Maxwell’s equations: scattering off periodic structures.” In: *Journal of Computational Physics* 226.1 (2007), pp. 477–493.

[Sch09] M. Schulte. “Streuverhalten von texturierten TCO-Substraten in Silizium-Dünnschichtsolarzellen.” PhD thesis. RWTH Aachen, 2009.

[Sch97] J. Schöberl. “NETGEN An advancing front 2D/3D-mesh generator based on abstract rules.” In: *Computing and visualization in science* 1.1 (1997), pp. 41–52.

[SG04] O. Schenk and K. Gärtner. “Solving unsymmetric sparse systems of linear equations with PARDISO.” In: *Future Generation Computer Systems* 20.3 (2004), pp. 475–487.

[She+11a] X. Sheng et al. “Design and Non-lithographic Fabrication of Light Trapping Structures for Thin Film Silicon Solar Cells.” In: *Advanced Materials* 23 (2011), pp. 843–847.

[She+11b] X. Sheng et al. “Optimization-based design of surface textures for thin-film Si solar cells.” In: *Optics Express* 19.104 (2011), A841–A850.

[She96] Jonathan Richard Shewchuk. “Triangle: Engineering a 2D Quality Mesh Generator and Delaunay Triangulator.” In: *Applied Computational Geometry: Towards Geometric Engineering*. Ed. by Ming C. Lin and Dinesh Manocha. Vol. 1148. Lecture Notes in Computer Science. From the First ACM Workshop on Applied Computational Geometry. Springer-Verlag, May 1996, pp. 203–222.

[Si09] Hang Si. *A quality tetrahedral mesh generator and three-dimensional delaunay triangulator*. Weierstrass Institute for Applied Analysis and Stochastic, Berlin, Germany, 2009. URL: `http://tetgen.org`.

[Sim04] I. Simonsen. “A random walk through surface scattering phenomena: Theory and phenomenology.” In: *Arxiv preprint cond-mat/0408017* (2004).

[Siv+09] V. Sivakov et al. “Silicon nanowire-based solar cells on glass: synthesis, optical properties, and cell parameters.” In: *Nano letters* 9.4 (2009), pp. 1549–1554.

[SK09] H. Sai and M. Kondo. “Effect of self-orderly textured back reflectors on light trapping in thin-film microcrystalline silicon solar cells.” In: *Journal of Applied Physics* 105.9 (2009), pp. 094511–094511.

[SKS06] R. Stangl, M. Kriegel, and M. Schmidt. “AFORS-HET, Version 2.2, a numerical computer program for simulation of heterojunction solar cells and measurements.” In: *Photovoltaic Energy Conversion, Conference Record of the 2006 IEEE 4th World Conference on*. Vol. 2. IEEE. 2006, pp. 1350–1353.

[SML09] I. Simonsen, A.A. Maradudin, and T.A. Leskova. “The scattering of electromagnetic waves from two-dimensional randomly rough perfectly conducting surfaces: the full angular intensity distribution.” In: *Arxiv preprint arXiv:0910.0563* (2009).

[Son+09] T. Sontheimer et al. “Crystallization kinetics in electron-beam evaporated amorphous silicon on ZnO:Al-coated glass for thin film solar cells.” In: *Applied Physics Letters* 95.10 (2009), pp. 101902–101902.

[Son+10] T. Sontheimer et al. “Crystal nucleation in electron-beam evaporated amorphous silicon on ZnO: Al-and SiN-coated glass for thin film solar cells.” In: *physica status solidi (c)* 7.3-4 (2010), pp. 525–528.

[Son+11a] T. Sontheimer et al. “Large-area fabrication of equidistant free-standing Si crystals on nanoimprinted glass.” In: *physica status solidi (RRL)-Rapid Research Letters* 5 (2011), pp. 376–378. DOI: 10.1002/pssr.201105437.

[Son+11b] T. Sontheimer et al. “Light harvesting architectures for electron beam evaporated solid phase crystallized Si thin film solar cells: Statistical and periodic approaches.” In: *Journal of Non-Crystalline Solids* (2011). DOI: 10.1016/j.jnoncrysol.2011.10.025.

[Son11] Tobais Sontheimer. “Design of electron beam evaporated Si thin films for solid phase crystallized solar cells on glass.” PhD thesis. Technische Universität Berlin, 2011.

[Spr+05] J Springer et al. “Light trapping and optical losses in microcrystalline silicon pin solar cells deposited on surface-textured glass/ZnO substrates.” English. In: *SOLAR ENERGY MATERIALS AND SOLAR CELLS* 85.1 (2005), 1–11. ISSN: 0927-0248. DOI: {10.1016/j.solmat.2004.02.020}.

[SPV04] J. Springer, A. Poruba, and M. Vanecek. “Improved three-dimensional optical model for thin-film silicon solar cells.” In: *Journal of applied physics* 96.9 (2004), pp. 5329–5337.

[Ste+76] F. Stetter et al. “New materials for optical thin films.” In: *Applied Optics* 15.10 (1976), pp. 2315–2317. DOI: 10.1364/AO.15.002315.

[SZ98] R.E.I. Schropp and M. Zeman. *Amorphous and microcrystalline silicon solar cells: modeling, materials, and device technology*. Vol. 5. Springer, 1998.

[Söd+10] T. Söderström et al. "Flexible micromorph tandem a-Si/μc-Si solar cells." In: *Journal of Applied Physics* 107.1 (2010), pp. 014507–014507.

[Söd09] T. Söderström. "Single and multi-junction thin film silicon solar cells for flexible photovoltaics." PhD thesis. Université de Neuchâtel, 2009.

[TCW96] D. Thorp, P. Campbell, and S.R. Wenham. "Conformal films for light-trapping in thin silicon solar cells." In: *Progress in Photovoltaics: Research and Applications* 4.3 (1996), pp. 205–224.

[Tie+84] T. Tiedje et al. "Limiting efficiency of silicon solar cells." In: *Electron Devices, IEEE Transactions on* 31.5 (1984), pp. 711–716.

[Tse+11] P.C. Tseng et al. "Antireflection and light trapping of subwavelength surface structures formed by colloidal lithography on thin film solar cells." In: *Progress in Photovoltaics: Research and Applications* (2011). DOI: 10.1002/pip.1123.

[Van+11] M. Vanecek et al. "Nanostructured three-dimensional thin film silicon solar cells with very high efficiency potential." In: *Applied Physics Letters* 98 (2011), p. 163503.

[Vog+01] L. Vogelaar et al. "Large area photonic crystal slabs for visible light with waveguiding defect structures: Fabrication with focused ion beam assisted laser interference lithography." In: *Advanced Materials* 13.20 (2001), pp. 1551–1554.

[Wan+09] Y. Wang et al. "Spherical antireflection coatings by large-area convective assembly of monolayer silica microspheres." In: *Solar Energy Materials and Solar Cells* 93.1 (2009), pp. 85–91.

[WC01] K.F. Warnick and W.C. Chew. "Numerical simulation methods for rough surface scattering." In: *Waves in Random Media* 11.1 (2001), pp. 1–30.

[Wei+10] D.N. Weiss et al. "Nanoimprinting for diffractive light trapping in solar cells." In: *Journal of Vacuum Science & Technology B: Microelectronics and Nanometer Structures* 28 (2010), p. C6M98.

[Wei11] Eric W. Weisstein. *Central Limit Theorem*. MathWorld – A Wolfram Web Resource. 2011. URL: http://mathworld.wolfram.com/CentralLimitTheorem.html.

[Whi97] DJ Whitehouse. "Surface metrology." In: *Measurement Science and Technology* 8 (1997), p. 955.

[WMK10] D.N. Weiss, S.T. Meyers, and D.A. Keszler. “All-inorganic thermal nanoimprint process.” In: *Journal of Vacuum Science & Technology B: Microelectronics and Nanometer Structures* 28 (2010), p. 823.

[Won05] Alfred Kwok-Kit Wong. *Optical Imaging in Projection Microlithography*. SPIE Press, 2005.

[Wu00] Jiunn-Jong Wu. “Simulation of rough surfaces with FFT.” In: *Tribology International* 33 (2000), pp. 47–58.

[Wür05] P. Würfel. *Physics of solar cells*. Wiley, 2005.

[Yab82] Eli Yablonovitch. “Statistical ray optics.” In: *J. Opt. Soc. Am.* 72.7 (1982), pp. 899–907.

[Yab93] E. Yablonovitch. “Photonic band-gap structures.” In: *Journal of the Optical Society of America B* 10 (1993), pp. 283–283.

[Yam+00] K. Yamamoto et al. “Thin film Si solar cell fabricated at low temperature.” In: *Journal of Non-Crystalline Solids* 266.269 (2000), pp. 1082–1087.

[YF11] Z. Yu and S. Fan. “Angular constraint on light-trapping absorption enhancement in solar cells.” In: *Applied Physics Letters* 98 (2011), p. 011106.

[YRF10a] Z. Yu, A. Raman, and S. Fan. “Fundamental limit of light trapping in grating structures.” In: *Optics Express* 18.103 (2010), A366–A380.

[YRF10b] Z. Yu, A. Raman, and S. Fan. “Fundamental limit of nanophotonic light trapping in solar cells.” In: *Proceedings of the National Academy of Sciences* 107.41 (2010), pp. 17491–17496.

[YUF06] T. Yagi, Y. Uraoka, and T. Fuyuki. “Ray-trace simulation of light trapping in silicon solar cell with texture structures.” In: *Solar energy materials and solar cells* 90.16 (2006), pp. 2647–2656.

[Zen+08] L. Zeng et al. “Demonstration of enhanced absorption in thin film Si solar cells with textured photonic crystal back reflector.” In: *Applied Physics Letters* 93 (2008), p. 221105.

[Zhu+08] J. Zhu et al. “Optical absorption enhancement in amorphous silicon nanowire and nanocone arrays.” In: *Nano letters* 9.1 (2008), pp. 279–282.

[Zhu+09] J. Zhu et al. “Nanodome solar cells with efficient light management and self-cleaning.” In: *Nano letters* 10.6 (2009), pp. 1979–1984.

[Zhu+10] J. Zhu et al. “Nanostructured photon management for high performance solar cells.” In: *Materials Science and Engineering: R: Reports* 70.3-6 (2010), pp. 330–340.

[ZK00] VV Zalipaev and AV Kostin. “Rigorous and approximate methods for modeling wave scattering from a locally perturbed perfectly conducting surface.” In: *Technical Physics* 45.1 (2000), pp. 1–7.

[ZK08] M. Zeman and J. Krc. “Optical and electrical modeling of thin-film silicon solar cells.” English. In: *JOURNAL OF MATERIALS RESEARCH* 23.4 (2008). Spring Meeting Symposium of the Materials-Research-Society, San Francisco, CA, APR 09-13, 2007, 889–898. ISSN: 0884-2914. DOI: {10.1557/JMR.2008.0125}.

[Zsc09] Lin Zschiedrich. “Transparent boundary conditions for Maxwell’s equations.” PhD thesis. Freie Universität Berlin, 2009.

Abbreviations

ACF	—	autocorrelation function
AFM	—	atomic force microscopy
ARC	—	anti–reflection coating
ARS	—	angular resolved scattering
AZO	—	aluminum doped zinc oxide (ZnO:Al)
EQE	—	external quantum efficiency
FDTD	—	finite difference time domain
FEM	—	finite element modeling
FFT	—	fast Fourier transform
FTO	—	fluor doped tin oxide (SnO_2:F)
GWp	—	Gigawatt peak
IFFT	—	inverse FFT
IEA	—	International Energy Agency
IQE	—	internal quantum efficiency
LPCVD	—	low pressure chemical vapor deposition
LPIF	—	light path improvement factor
PSD	—	power spectral density
PV	—	photovoltaic
QE	—	quantum efficiency

RCWA	—	rigorous coupled waveguide analysis
rms	—	root mean square
SEM	—	scanning electron microscope
SPC	—	solid phase crystallization
TCO	—	transparent conductive oxide
TEM	—	transmission electron microscope

Eidesstattliche Erklärung

Hiermit versichere ich an Eides statt, die vorliegende Arbeit selbständig und ausschließlich unter Verwendung der angegebenen Hilfsmittel und Quellen verfasst zu haben.

_____

Daniel Lockau

_____

Ort, Datum